



Electronic structures of magnetic iron and cobalt thin films on tungsten(001) : a spin-polarized inverse photoemission study  
by Qing Cai

A thesis submitted in partial fulfillment of the requirements for the degree of Doctor of Philosophy in Physics  
Montana State University  
© Copyright by Qing Cai (1989)

Abstract:

Electronic structure is a central question in metallic magnetism as well as in magnetic materials research. The electronic properties in a two-dimensional system such as thin films of a few atomic layers is an important issue in surface science. The epitaxial thin film preparation and morphology are of special technological interests. In this thesis, these questions are addressed. Spin-polarized inverse photoemission spectroscopy is used to study the unoccupied electron band states in magnetic thin film magnets of Fe and Co epitaxially grown on W(001) surface.

The clean W(001) surface was studied by angle-resolved inverse photoemission spectroscopy and the bulk band dispersion was determined.

Ultrathin Fe overlayers on W(001) show a square lateral crystal structure similar to the bcc-Fe(001) surface. The electronic structure develops into a structure that is close to that of bulk Fe at about four atomic layers. In the normal-incidence spin polarized inverse photoemission spectra, direct transitions to the majority and minority final states near the H'25 point are identified in good agreement with the theoretical calculations. One Fe monolayer, or multilayers less than four, showed behavior corresponding to a gradually reduced Curie temperature. When the film thickness is reduced, the spin-resolved spectral behavior show that the majority spin signal peak moves from near the Fermi energy to about 1.3 eV while the minority peak stays at about the same position near 1.3 eV. The results are used to examine the spatial correlation of the spin fluctuations in the system in comparison with a theoretical spectral calculation, and favors the disordered-local-moment picture in the contemporary theory of itinerant magnetism.

The Co overlayer shows an overlayer structure that consists of equivalent, mutually rotated domains of distorted hexagonal lateral structure. For one atomic layer of Co in that structure, which has a nominal lateral atomic density twice that of the substrate surface, in-plane remanent magnetization is not found. The results for two atomic Co layers show a prominent minority peak that is consistent with the hcp-Co band structure. The existence of a small majority spin peak at an energy slightly higher than the minority peak provokes serious questions concerning the electronic and magnetic properties of the Co thin films. Further investigations in this area of spin-polarized electronic spectroscopic technique on spin-dependent electronic structure study are suggested.

ELECTRONIC STRUCTURES OF MAGNETIC  
IRON AND COBALT THIN FILMS ON TUNGSTEN(001):  
A SPIN-POLARIZED INVERSE PHOTOEMISSION STUDY

by  
Qing Cai

A thesis submitted in partial fulfillment  
of the requirements for the degree

of  
Doctor of Philosophy  
in  
Physics

MONTANA STATE UNIVERSITY  
Bozeman, Montana

August 1989

D378  
C12

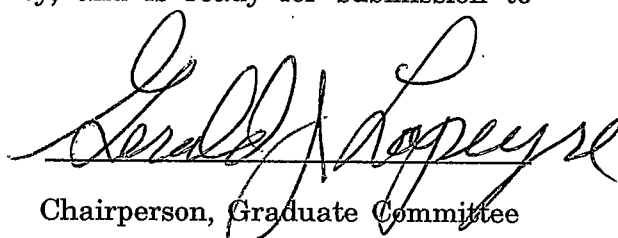
APPROVAL

of a thesis submitted by

Qing Cai

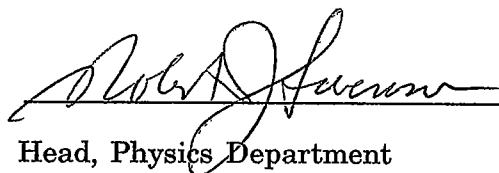
This thesis has been read by each member of the thesis committee and has been found to be satisfactory regarding content, English usage, format, citations, bibliographic style, and consistency, and is ready for submission to the College of Graduate Studies.

8/28/89  
Date

  
Chairperson, Graduate Committee

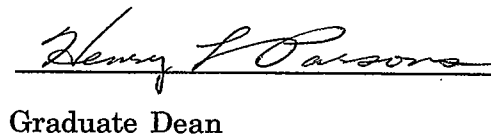
Approved for the Physics Department

8/28/89  
Date

  
Head, Physics Department

Approved for the College of Graduate Studies

8/30/89  
Date

  
Graduate Dean

## STATEMENT OF PERMISSION TO USE

In presenting this thesis in partial fulfillment of the requirements for a doctoral degree at Montana State University, I agree that the Library shall make it available to borrowers under rules of the Library. I further agree that copying of this thesis is allowable only for scholarly purposes, consistent with "fair use" as prescribed in the U.S. Copyright Law. Requests for extensive copying or reproduction of this thesis should be referred to University Microfilms International, 300 North Zeeb Road, Ann Arbor, Michigan 48106, to whom I have granted "the exclusive right to reproduce and distribute copies of the dissertation in and from microfilm and the right to reproduce and distribute by abstract in any format."

Signature *Cliff Cui*  
Date 8/28/89

DEDICATED TO MY PARENTS

## VITA

Qing Cai, born in Nanjing, Jiansu, China, is the son of Disheng Cai and Jing Zhou. He has an older sister, Zuocao.

Qing Cai was raised in Nanjing. One year after he graduated from Nanjing 45th high school, he was assigned to a small local factory, SUJIMO (machinery manufacturer for plastic products) in Autumn 1987, as molding mechanic apprentice.

In early 1978, he took the entrance examination and was admitted by Nanjing University, Nanjing, China, where he completed his undergraduate education in physics.

In September 1981, he started his graduate study at Montana State University, where a Master of Science degree was obtained in 1983.

## ACKNOWLEDGMENTS

I am indebted to some special individuals who have made it possible for me to complete this work. Dr. Gerald J. Lapeyre, my thesis advisor, suggested this work, and provided guidance and encouragement. His scientific inspiration was a valuable asset to this work, and his confidence in me throughout this work is greatly appreciated. Dr. Recep Avci participated in the work during his sabbatical year in 1987-1988, and made valuable contributions to this work. Working with him and learning from him was one of the most beneficial experiences in my graduate career. Dr. James Anderson provided important criticisms and advice in many ways. His critical reading of my scientific papers including this thesis is especially acknowledged.

I would like to thank Mr. Milt C. Jaehnig, Andrew Paule, Tom A. Jungst, Gordon Williamson, Tony Knick, and Alfred Beldring for providing their technical expertise in helping me construct and operate the experimental apparatus. Thanks to Dr. Cliff Olson of Iowa State University for his assistant in calibrating our photon detector at the University of Wisconsin's Synchrotron Radiation Center. I would also like to thank Drs. David Frankel, Richard Smith, Wayne Ford, and John Hermanson for helpful consultations in the research. My special thanks go to Ms. Alice Allen, Kathy Phillips, Linda Todd and Robyn Klein for their kind help during my stay at M.S.U.

I am grateful to the Physics Department, M.S.U. and Dr. Robert Swenson who was very kind to provide me this opportunity to study at this department and provided me with continuous support throughout my graduate years. The cheerful help and friendly favors I received from, and exchanged with, the staff and fellow students in the department are very precious to me.

## TABLE OF CONTENTS

	Page
VITA .....	v
ACKNOWLEDGMENT .....	vi
ABSTRACT .....	xii
1. INTRODUCTION .....	1
2. SPIN-POLARIZED INVERSE PHOTOEMISSION AND THE ELECTRONIC STRUCTURE OF METALLIC FERROMAGNETS .....	7
A. Inverse Photoemission .....	9
Concept .....	9
Models .....	10
Spin-Resolution of IPES .....	15
Surface-Sensitivity of IPES .....	17
Angle Dependent SPIPES .....	18
Experimental Feasibilities .....	20
B. The Electronic Structure of Metallic Ferromagnets .....	21
Band Theory of Metallic Ferromagnetism .....	21
Ground State Properties of Fe, Co, Ni .....	22
Surface Magnetism and 2D Magnetic Systems .....	23
Models of Electronic Structure at Elevated Temperature .....	27
3. SPIN-POLARIZED ELECTRON SOURCE, EXPERIMENTAL APPARATUS AND PROCEDURES .....	34
A. Spin-Polarized Electron Source .....	34
Spin-Polarized Photoelectron Emission from GaAs .....	35
Construction of Polarized Electron Source .....	39
Operation of the Polarized Electron Source .....	45
B. Bandpass Photon Detector .....	49
C. Experimental Chamber .....	52
D. Sample Preparation .....	57
E. Data Acquisition .....	62



## TABLE OF CONTENTS - continued

4. CLEAN W(001) RESULTS .....	67
5. Fe ON W(001) .....	76
A. Thin Film Characterization .....	76
B. Normal-Incident SPIPES from Ultrathin Magnetic Films of Fe ....	83
C. Off-Normal-Incidence SPIPES .....	90
D. Thickness-Dependent SPIPES from Fe Monolayers .....	95
6. Co ON W(001) .....	99
A. LEED Results .....	99
B. SPIPES Results .....	103
7. SUMMARY .....	111
REFERENCES .....	114
APPENDICES .....	119
A. Computer Program .....	120
B. Magnetic Anisotropy of Thin Films .....	126

## LIST OF TABLES

Table	Page
1 Magnetic moments, exchange splittings and Curie temperatures of selected 3-d transition metal elements . . . . .	22
2 Bulk material properties of W, Fe, Co and Ni . . . . .	77

## LIST OF FIGURES

Figure	Page
1 Phenomenology of ordinary and spin-polarized inverse photoemission . .	8
2 Bulk transitions and its relationship with IPES spectrum . . . . .	14
3 Schematic of primary contribution and background from inelastic scattering by electron-hole creation . . . . .	16
4 Relationship between k-vectors across the solid-vacuum interface . . . .	19
5 Electron spin distribution in energy bands of Fe, Co and Ni. . . . .	24
6 Comparison of the Stoner, Heisenberg and unified models . . . . .	28
7 Temperature dependent local-band model spectral behavior . . . . .	30
8 Theoretical spectra at elevated temperatures from Fe $\Gamma'_{25}$ . . . . .	32
9 Surface and bulk magnetization vs. $T/T_C$ . . . . .	33
10 GaAs energy diagram near the center of the Brillouin zone. . . . .	36
11 The GaAs band bending at the Cs+O <sub>2</sub> treated surface. . . . .	38
12 Schematic of polarized electron source chamber . . . . .	40
13 Schematic of the electrostatic lens design, source chamber . . . . .	43
14 Schematic of the electrostatic lens design, experimental chamber. . . .	44
15 Typical activation curves of GaAs electron source . . . . .	47
16 Diagram of Canneltron bandpass photon detector . . . . .	50
17 Photon detector spectral responses . . . . .	53
18 System layout . . . . .	54
19 Flowchart of retarding-field Auger spectroscopy . . . . .	56
20 Perspective view of the experimental geometry . . . . .	58
21 Sample holder and spot detector . . . . .	59

## LIST OF FIGURES - continued

22	Evaporator and QCO monitor .....	61
23	Schematic of SPIPES measurement .....	63
24	Energy diagram of SPIPES experiment .....	65
25	Tungsten bcc BZ, SBZ, and IPES detecting plane .....	68
26	LEED pattern of p(1×1) W(001) .....	69
27	W(001) ARIPIPES spectra with SrF <sub>2</sub> window detector .....	71
28	Band dispersion along $\bar{\Delta}$ .....	73
29	W band calculations .....	74
30	LEED patterns of Fe/W(001) .....	78
31	Auger amplitudes of W and Fe as a function of deposition. ....	80
32	LSF-fitted Auger amplitude ratio measurements .....	82
33	SPIPES and spectral asymmetry of Fe thin films. ....	85
34	Fe bulk bands, and bulk and surface layer-projected DOS. ....	88
35	Angle-dependent spectra from bulklike Fe thin film .....	92
36	Energy bands of bulk Fe along the G direction .....	93
37	Theoretical Fe spectra for spin-polarized inverse photoemission from the H <sub>25</sub> ' state .....	97
38	LEED patterns of W(001)p(1×1) and Co/W(001) .....	100
39	Illustration of decomposition of Co/W(001) LEED patterns and the corresponding Co overlayer structure .....	102
40	The Co SPIPES spectra .....	104
41	Domain adjusted SPIPES spectra of two monolayers of Co .....	107
42	Theoretical energy bands of hcp Co .....	108
43	Sample FORTRAN program .....	121

## ABSTRACT

Electronic structure is a central question in metallic magnetism as well as in magnetic materials research. The electronic properties in a two-dimensional system such as thin films of a few atomic layers is an important issue in surface science. The epitaxial thin film preparation and morphology are of special technological interests. In this thesis, these questions are addressed. Spin-polarized inverse photoemission spectroscopy is used to study the unoccupied electron band states in magnetic thin film magnets of Fe and Co epitaxially grown on W(001) surface.

The clean W(001) surface was studied by angle-resolved inverse photoemission spectroscopy and the bulk band dispersion was determined.

Ultrathin Fe overlayers on W(001) show a square lateral crystal structure similar to the bcc-Fe(001) surface. The electronic structure develops into a structure that is close to that of bulk Fe at about four atomic layers. In the normal-incidence spin polarized inverse photoemission spectra, direct transitions to the majority and minority final states near the  $H'_{25}$  point are identified in good agreement with the theoretical calculations. One Fe monolayer, or multilayers less than four, showed behavior corresponding to a gradually reduced Curie temperature. When the film thickness is reduced, the spin-resolved spectral behavior show that the majority spin signal peak moves from near the Fermi energy to about 1.3 eV while the minority peak stays at about the same position near 1.3 eV. The results are used to examine the spatial correlation of the spin fluctuations in the system in comparison with a theoretical spectral calculation, and favors the disordered-local-moment picture in the contemporary theory of itinerant magnetism.

The Co overlayer shows an overlayer structure that consists of equivalent, mutually rotated domains of distorted hexagonal lateral structure. For one atomic layer of Co in that structure, which has a nominal lateral atomic density twice that of the substrate surface, in-plane remanent magnetization is not found. The results for two atomic Co layers show a prominent minority peak that is consistent with the hcp-Co band structure. The existence of a small majority spin peak at an energy slightly higher than the minority peak provokes serious questions concerning the electronic and magnetic properties of the Co thin films. Further investigations in this area of spin-polarized electronic spectroscopic technique on spin-dependent electronic structure study are suggested.

## CHAPTER 1

## INTRODUCTION

Recent advances in a variety of areas of surface science, computational physics, and instrumentation have aroused new interest in the field of magnetism. The electronic structure of matter is an issue central to our understanding of not only its physical and chemical properties, but also its magnetic properties, since magnetism is a quantum mechanical phenomenon originating in the spin-dependent electronic configurations in solids. It is attributable to the developments of spin-sensitive electron spectroscopy and ultrahigh vacuum techniques that the direct experimental study of spin-dependent electron band structure in magnetic systems has become possible.

The study of the electronic structure of transition metal magnets has gone through a long period of controversial debate. The Stoner band model,<sup>1</sup> proposed over 50 years ago, has proved quite adequate to describe magnetic ground state properties at or near zero temperature quite well. In this model, spontaneous ferromagnetism occurs when it is energetically favorable for the energy band structure to be split by the exchange interaction, as for Fe, Co and Ni. The non-integral magnetic moment in units of Bohr magnetons ( $\mu_B$ ) per atom can be explained readily, since the magnetic moment is just the amount by which the itinerant electrons of majority spin( $\uparrow$ ), where the electron spin magnetic moment is parallel to the internal magnetization direction, outnumber those of minority spin( $\downarrow$ ), where the electron spin magnetic moment is opposite to the internal magnetization, because of the relative shift in electron energy

bands by the amount of the exchange-splitting ( $\Delta_{\text{exch}}$ ). At finite temperatures close to and above the Curie temperature ( $T_C$ ), however, the Stoner model fails, for example, to explain some fundamental thermodynamic properties such as the Curie-Weiss law above  $T_C$ . It is agreed that there exists a local magnetic moment even above  $T_C$ . Spin-density fluctuations are expected to play an important role. Developments beyond the Stoner model or the Heisenberg model have been made, and involve mainly a local-band-picture or a disordered-local-moment picture. This area of research remains active, and many questions require further theoretical and experimental investigations.

Quantitative information about the spin-dependent band structure has been obtained because of the advance in computational physics facilitated by the tremendous increase of computing power since the 1970s. Calculations based on the one-electron picture have been surprisingly successful in describing the electronic properties.<sup>2</sup> This approach provides a firm foundation for experimental investigations such as photoemission and inverse photoemission. Despite the controversy at finite temperatures, the investigation of zero-temperature ground state properties has been extended from three-dimensional to two-dimensional problems such as surfaces and thin films (for example, see Ref. 3) in order to investigate their surface electronic and magnetic properties. One of the key issues that has stimulated the renaissance of magnetism research is the possible existence of a magnetic "dead layer" at the surface of bulk magnets.<sup>4</sup> Further, the scope of the research has included not only materials in their equilibrium crystal structure, but also materials having a metastable crystal structure, variations of lattice spacing,<sup>5</sup> and transition metal overlayers on other substrate surfaces and sandwiches built up of several layers.<sup>6,7</sup> For these unusual systems very interesting results have been found

such as giant surface magnetic moments of monolayer systems<sup>7</sup> and geometry-induced magnetic phase transitions.<sup>5</sup> Such studies, mainly theoretical, have provided a rich store of information about electronic structure, and there has been an acute need for experimental information.

The maturing of the angle-resolved photoemission technique has left us with a powerful tool to study electron structure in solids and at surfaces. The spin-dependent version of photoemission (SP-PES), which was developed at the end of the last decade, has added another degree of freedom to our understanding of electronic structure. By these means the spin-split band structure can be investigated experimentally. Inverse photoemission spectroscopy (IPES) was developed much later, in the 1980s, the delay being due to the very small signal involved in this technique. However, IPES has been found very useful in some important areas of investigation, such as bulk electronic structure, surface states, and chemisorption states, because of the special energy region that can be probed, between Fermi level and vacuum energy, which is not accessible directly by other means. The spin-sensitive version of IPES (SPIPES), while on an equal footing with SP-PES theoretically, has the experimental advantage of having a much higher spin-dependent detection efficiency than that of the spin-detection methods in SP-PES. Therefore, the first SPIPES was demonstrated in 1982, soon after SP-PES was demonstrated.

It is particularly interesting to examine the electronic structure information obtained from spin-split overlayers deposited on a non-spin-split substrate material, in order to explore the initial development of the electronic structure of transition metal thin films. This approach is possible only if one can prepare nearly ideal atomically smooth ultrathin film overlayers. Clusters, steps and interdiffused overlayers obviously cannot serve the purpose of a two-



dimensional (2D) transition metal system. If all the above prerequisites are satisfied, then it is possible to explore magnetic thin film electronic structures. In addition, transition metal overlayers, especially their superlattices, can have the lattice structure substantially altered from that of the bulk material, therefore providing an excellent opportunity to study such novel systems.

The experimental investigation of the electronic structure of 2D magnetic systems can address some fundamental questions. For example, how does the exchange splitting of certain bands depend on the  $k$  vector, and how does it change with temperature? How is the magnetization influenced by the crystal structure (fcc, bcc, and with variation of lattice constants in the superlattice structure)? What behavior shall we expect for surface magnetism as an intrinsic surface effect due to the termination of crystal symmetry at the surface, and what shall we expect of the influence of surface reconstruction (contraction or relaxation)? What effect does chemisorption have on the surface electronic structure, especially on the magnetic ordering? What role does the substrate-overlayer interface play in the electronic structure and magnetic properties? What is the direction of remanent magnetization at the surface and for thin films of various lattice spacings? How does the Curie temperature change with the film thickness? How does the magnetic ordering depend on dimensionality, or is there such a general trend? To extend the dimensionality idea further, what can one determine about a one-dimensional magnetic system? For example, can we prepare one-dimensional magnetic chains on surface ridges? Can we expect the magnetic moment to be intermediate between thin films and zero dimensional atoms and clusters?

We can continue to pose these questions, some of which go to the root of basic concepts in physics, like the general relationship between order-disorder

phases and dimensionality; some questions are applicable to 3D bulk systems. Certain topics such as the effects of chemisorption and especially oxidation magnetization may be very important technologically. For example, surface magnetization can be of significance in the magnetic recording industry, because when finer particles and thinner films are used, surface and size effects are going to be significant. Also, thin film preparation, and the future technology of superlattices and other synthetic magnetic materials may become important. In short, there are growing interests in both the fundamental and the technological aspects of the magnetic and the electronic structure of various materials such as magnetic thin films. Some of the problems cannot be easily resolved using traditional surface analytical techniques. The SPIPES technique described in this thesis proves to be a powerful tool to search for some of the answers experimentally.

Finally, the spin-polarized inverse photoemission spectroscopy is of intrinsic significance as an advanced member of the class of electronic spectroscopic techniques. It has a unique degree of freedom, the electron spin, and is also angle resolved. The theory of this technique and related phenomena need to be investigated.

This thesis is outlined as follows. The theory of SPIPES will be given in Chapter 2, together with a survey of the background of metallic magnetism. The following chapter describes the experimental setup and the methods used. Chapters 4-6 are devoted to experimental results, starting from clean W(001) to test out inverse photoemission spectroscopy as well as to prepare an ideal substrate for the transition metal overlayers. The Fe and Co results from their ultrathin films on W(001) will follow. Finally, a summary is given in Chapter 7.

Because the experimental techniques employ vacuum and surface science terminologies extensively, a list of the abbreviations and acronyms is given here for convenience.

AES - Auger electron spectroscopy

ARIPES - angle-resolved inverse photoelectron spectroscopy

ARPES - angle-resolved photoelectron spectroscopy

ARUPS - angle-resolved ultraviolet photoemission spectroscopy

BZ - Brillouin zone

DOS - density of states

IPES - inverse photoelectron spectroscopy

LEED - low energy electron diffraction

PES - photoelectron spectroscopy

QCO - quartz crystal oscillator

RF-AES - retarding-field Auger electron spectroscopy

SBZ - surface Brillouin zone

SPIPES - spin-polarized inverse photoelectron spectroscopy

SP-PES - spin-polarized photoemission spectroscopy

UHV - ultra high vacuum

## CHAPTER 2

### SPIN-POLARIZED INVERSE PHOTOEMISSION AND THE ELECTRONIC STRUCTURE OF METALLIC FERROMAGNETS

Inverse photoemission (IPES), as its name suggests, can be considered as the time-reversed process of photoemission. As illustrated in Fig. 1 together with photoemission for comparison, the process involves incident electrons falling to lower energy levels by emitting photons in the sampled material, and consequently revealing the electronic properties of the material. Spin-polarized inverse photoemission (SPIPES) uses polarized electrons in the process, and thereby reveals spin-dependent electronic properties such as are characteristic of the ferromagnetic transition metals. Transition-metal ferromagnetism, after many decades of study, is still a challenging and controversial subject in many aspects. New interests have also been fueled by the recent state-of-the-art theoretical calculations for two dimensional systems. The new spin-polarized electronic spectroscopic techniques, including SPIPES, may provide interesting information about this phenomenon. In this chapter, a general conceptual treatment of SPIPES will be presented, followed by an introduction to the theory of electronic structure of itinerant ferromagnets, especially in connection with SPIPES.

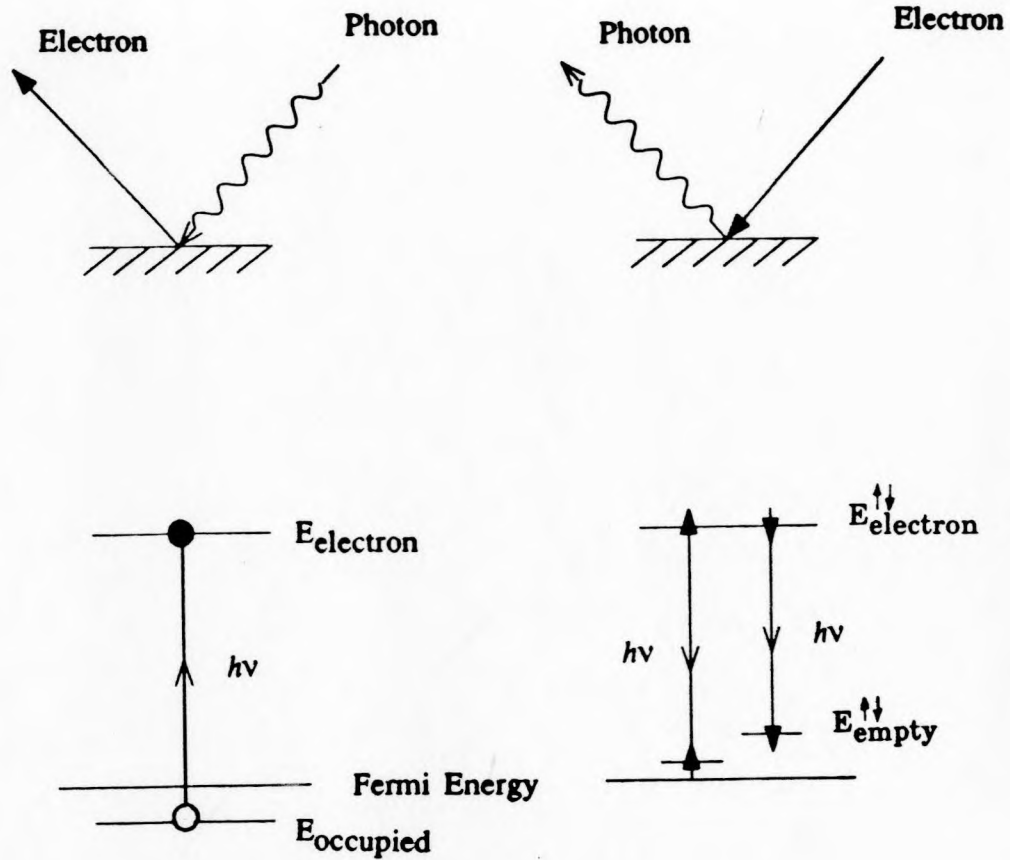


Figure 1. Phenomenology of photoemission, ordinary and spin-polarized inverse photoemission. Left: an incident photon is absorbed and excites an electron. Right: an incident electron with certain spin is de-excited, creating a photon.

### A. Inverse Photoemission

#### Concepts

The inverse photoemission process in solids can be described as an interaction between electron and photon in the presence of the crystal field. One may use the following formula to specify the relationship between the initial state of an electron,  $e^-$ , and the final state with an electron in a lower energy state and an emitted photon,  $h\nu$ ,

$$e^-(\mathbf{k}, E) \rightarrow e^-(\mathbf{k}-\mathbf{q}, E-h\nu) + h\nu(\mathbf{q}, h\nu) \quad (1)$$

in contrast to the photoemission (PES) process

$$h\nu(\mathbf{q}, h\nu) + e^-(\mathbf{k}', E') \rightarrow e^-(\mathbf{k}'+\mathbf{q}, E'+h\nu) \quad (2)$$

where all electron states,  $e^-$ , and photon states,  $h\nu$ , are specified by their momentum vectors,  $\mathbf{k}$  and  $\mathbf{q}$ , and energies,  $E$  and  $h\nu$ . As shown in Fig. 1, the electrons of certain energy  $E$  impinge on a material, and de-excite into lower energy states by emitting photons. Also known as bremsstrahlung isochromat spectroscopy (BIS), IPES is a complementary technique to ordinary photoemission in terms of the electron energy ranges investigated: While PES reveals the occupied electronic structure, ordinary IPES reveals the unoccupied structure. SPIPES reveals in addition the spin-dependent aspects of electronic structure as in the magnetic 3d transition metals, Fe, Co, and Ni. The time-reversal correspondence between PES and IPES allows one to transfer the well developed understanding of PES to IPES directly. The emitted photons are

examined either "monochromatically" i.e., at constant initial electron energy  $E$  by measurements of the photon energy distribution, or "isochromatically" at fixed photon energy  $h\nu$  by sweeping the electron energy  $E$  (in this chapter,  $E$  represents the incident electron energy, not the final state energy in the presentation of spectra). They are analogous to CFS (constant-final-state) and EDC (energy-distribution-curve) measurements in ordinary PES, respectively.

### Models

The formal single-step IPES theory is well established.<sup>8</sup> It involves quantum mechanical calculations of the probability that an electron with energy  $E$ , incident on the surface at a certain direction, emits a photon of energy  $h\nu$  and polarization  $s$ . In earlier applications of this method of calculation to specific metal surfaces,<sup>9-12</sup> spectral distribution curves were obtained that provided relative intensities, feature shapes, and polarization sensitivities. Meaningful comparisons were obtained between the theoretical models and the experiment, and physical parameters (such as the exchange splitting) were determined.

The so-called three-step model is often found more illuminating than the rigorous quantum-mechanical approach. Here the IPES phenomenon is treated as three separate processes: (1) wave function matching at the surface of an incoming plane wave of free electrons to traveling waves inside; (2) attenuated propagation of injected electron waves in the crystal; (3) radiative de-excitation from the initial state to unoccupied final states above the Fermi energy  $E_F$ , via the emission of photons. The photons emitted travel to the surface and escape into the vacuum where they are detected.

Electrons of any energy in vacuum are energetically allowed to enter the

solid, in contrast with the reverse process in PES where only electrons with perpendicular kinetic energy ( $p_{\perp}^2/2m$ ) greater than some threshold can escape. The broken symmetry along the surface normal prevents the conservation of the wavevector component perpendicular to the surface, but the wavevector component parallel to the surface is conserved modulo a reciprocal lattice vector. Inside the crystal, a linear combination of Bloch waves, which could be propagating or evanescent, are to be matched at the surface with the free-electron incident wave and the diffracted wave backscattered to the vacuum. The boundary condition determines the coupling coefficient,  $c_i$ , of an incident plane wave to a bulk state  $|i\rangle$ .

An electron in an excited state of energy  $E$  in the crystal may undergo de-excitation by emitting a photon. The yield function of the emitted photon flux  $I(E, hv)$  is in general a sum of a primary contribution  $I_p(E, hv)$  from electrons that have not suffered an inelastic collision prior to the radiative transition and a background contribution  $I_s(E, hv)$  from a compound process involving nonradiative decays followed by a radiative transition emitting a photon of energy within the detector window around  $hv=9.8\text{eV}$ :

$$I(E, hv) = I_p(E, hv) + I_s(E, hv) . \quad (3)$$

A monochromat or isochromat IPES spectrum can be described by this expression by fixing the parameter  $E$  or  $hv$ , respectively.

The primary contribution from bulk transitions is readily obtained in analogy to PES by considering direct radiative transitions

$$I_{\text{dir}}(E, hv) \sim \sum_{fi} \int_{\Omega} d^3k \, c_i |\langle f|\Delta|i\rangle|^2 \delta[E_i(\mathbf{k}) - E_f(\mathbf{k}) - hv] \cdot \delta[E_i(\mathbf{k}) - E] \quad (4)$$



where  $\Delta$ , the optical field perturbation as in PES, will be discussed explicitly later,  $c_i$  is the coupling coefficient between the free electron plane wave and the bulk state  $|i\rangle$  as mentioned earlier,  $E_f$  and  $E_i$  are the energies of final and initial states  $|f\rangle$  and  $|i\rangle$ ; Eq. (4) is to be summed over all possible states, provided both  $E_f$  and  $E_i$  are above the Fermi level  $E_F$ . The volume  $\Omega$  of integration over  $\mathbf{k}$  space depends on the experimental conditions, e.g. angle-resolved or angle-integrated.

The perturbation inducing the radiative transition may be described by the interaction term in an (unscreened) optical field,

$$\Delta = \frac{e}{2mc} (\mathbf{A} \cdot \mathbf{p} + \mathbf{p} \cdot \mathbf{A}) - e\Phi + \frac{e^2}{2mc^2} \mathbf{A} \cdot \mathbf{A} \quad (5)$$

where  $\mathbf{A}$  and  $\Phi$  are the corresponding vector and scalar potentials. The term  $\mathbf{A} \cdot \mathbf{A}$  in the equation does not contribute to one-photon processes and is neglected. It is further assumed at this point that the vector potential  $\mathbf{A}$  is fully determined by classical macroscopic dielectric theory, i.e. local-field corrections due to the inhomogeneity of the electron system are neglected. Then  $\mathbf{p} \cdot \mathbf{A} \sim \nabla \cdot \mathbf{A} = 0$ , and  $\Phi = 0$  in the Coulomb gauge. Finally,  $\mathbf{A} = \mathbf{A}_0 \cos(\mathbf{q} \cdot \mathbf{r}) \approx \mathbf{A}_0$  in the UV spectral region, because the optical wavelength  $2\pi/q$  is much larger than the atomic scale distance, the perturbation reduces to the well known electric dipole approximation

$$\Delta = \frac{e}{mc} \mathbf{A}_0 \cdot \mathbf{p} \quad (6)$$

and the matrix element takes the form  $\frac{e}{mc} |\mathbf{A}_0 \cdot \langle i | \mathbf{p} | f \rangle|$ .

The assumption of bulk states  $|i\rangle$  and  $|f\rangle$  in Eq. 4 implies that the vector  $\mathbf{k}$  is a good quantum number, which is conserved in the reduced Brillouin zone scheme, since the momentum of a UV photon is negligible.<sup>13</sup> A schematic diagram of a direct transition as compared to an indirect transition is shown in Fig. 2.

Peaks observed in the spectra have finite width because, even with perfect experimental resolution, the states involved in IPES are subject to lifetime broadening. In the single-step model the delta function in the above expression is replaced by a term involving a complex self-energy, which results in a Lorentzian line broadening.<sup>14</sup>

There is also the possibility of phonon-assisted indirect transitions. The average energy lost or gained by electron-phonon interaction is small enough compared with the experimental resolution so that the scattering may be considered elastic, but the  $\mathbf{k}$ -vector is changed. A schematic illustration of  $\mathbf{k}$ -non-conserving transitions is included in Fig. 2. Under the assumption of complete breakdown of  $\mathbf{k}$  conservation, the spectral distribution may be expressed in a form similar to that for direct transitions:

$$I_{\text{ind}}(E, h\nu) \sim \sum_{\mathbf{q}} \int d^3\mathbf{k}_i \int d^3\mathbf{k}_f |\langle f|\Delta|i\rangle|^2 \delta[E_i(\mathbf{k}_i) - E_f(\mathbf{k}_f) - h\nu] \delta[E_i(\mathbf{k}_i) - E] \quad (7)$$

where the volume of integration for both  $\mathbf{k}_i$  and  $\mathbf{k}_f$  is the entire Brillouin zone.

To give a feeling of comparison between direct and indirect transitions, let us assume the radiative transition matrix elements are constant. For an angle-integrated experiment, e.g. for a polycrystalline sample,  $I_{\text{dir}}$  leads to the so-called energy distribution of the joint density of states (EDJDOS), while  $I_{\text{ind}}$  will give a product of initial and final densities of states,  $I \propto N(E)N(E-h\nu)$ .

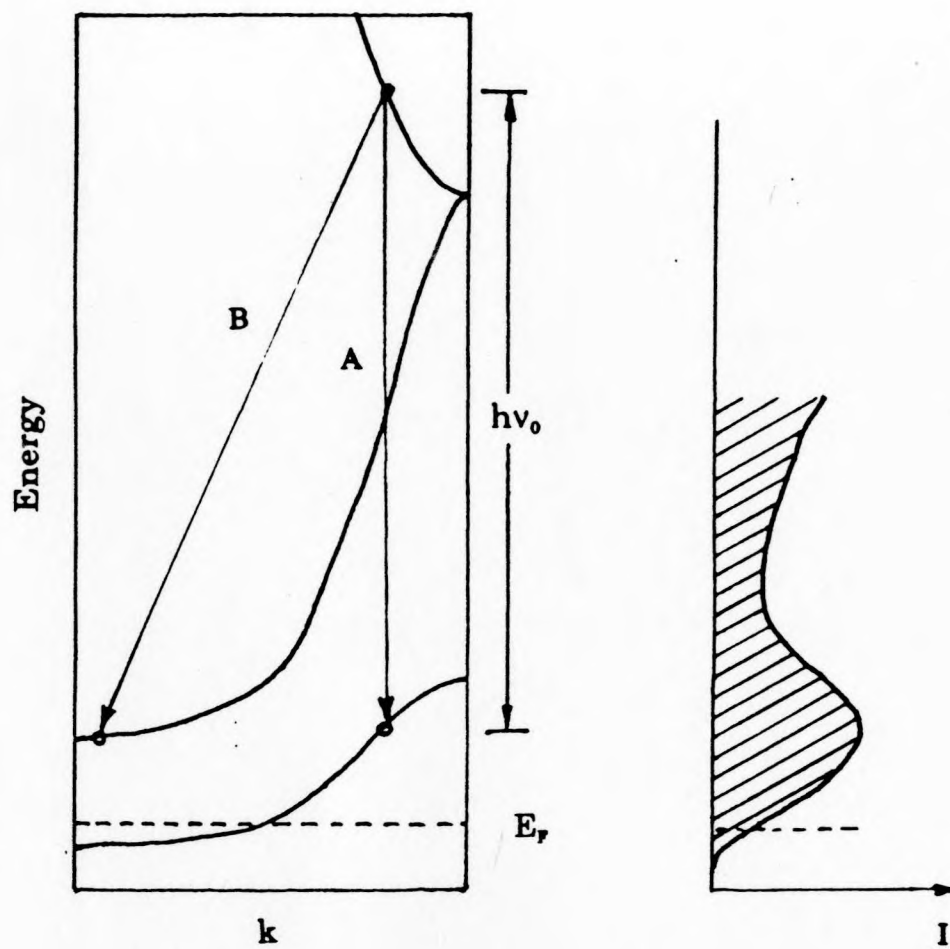


Figure 2. Bulk transitions A shows a direct ( $k$ -conserving) transition; B shows an indirect transition where  $k$  along the horizontal axis is not conserved. The curve on the right shows how the corresponding IPES spectrum may look like.

As an example, an isochromat spectrum from W(001) is given in Fig. 3. The vertical axis is the signal intensity, and the horizontal axis is the final state energy  $E - h\nu$ . The primary contribution is predominant near  $E_F$ . When the electron energy increases, the inelastic background increases nearly monotonically since the excess energy allows the electron to undergo an inelastic scattering and still make the radiative transition at  $h\nu = 9.8$  eV to a final state above  $E_F$ . A schematic diagram of this process is shown on the top of Fig. 3 for the electron-hole excitations, where the electron can lose energy by two quantum-mechanically equivalent channels.

The photon transport and escape processes can be treated as multiplicative factors over the spectral distribution. It has been found (cf. p232, Ref 15) that the transport function is close to unity and only weakly energy dependent. The escape function depends on the optical constants of the investigated material. While it is constant in isochromat mode spectra, it could in principle affect the monochromat spectra.

### Spin-Resolution of IPES

In the IPES process, as in the PES process, the spin of the electron involved in the radiative transitions is conserved, since in the electric dipole approximation, Eq. (6), the spin operator does not appear. When the electronic system of the material under investigation has spin-dependent structure, then the IPES spectrum is also spin-dependent.

The spin-dependent IPES spectra are usually represented as a pair of EDC (energy-distribution curve) curves of opposite spin-polarization, after the appropriate adjustments for experimental factors. It is sometimes useful to plot the spin-asymmetry together with the spectra, plotting both as a function

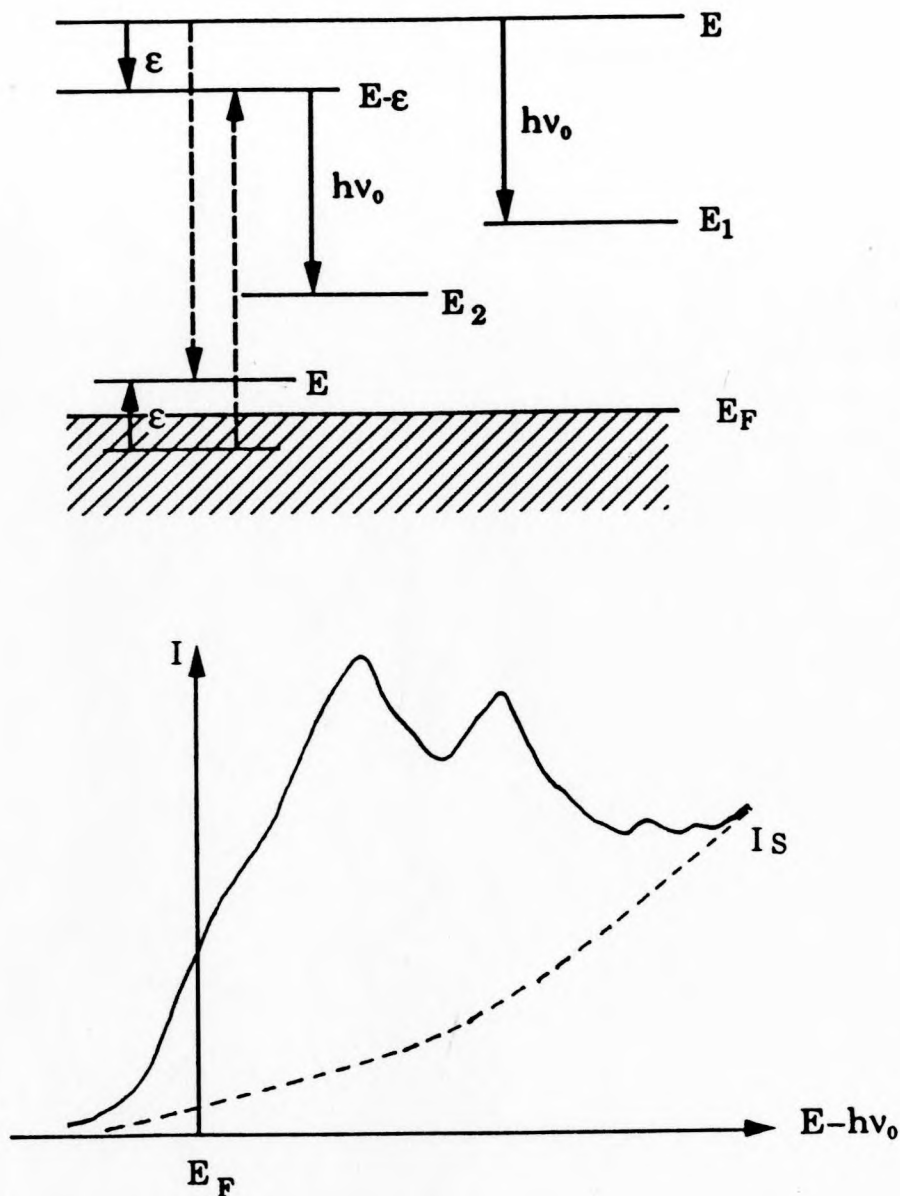


Figure 3. Energy level diagram and schematic spectrum for IPES of primary and inelastic contributions at photon energy  $h\nu_0$ . The radiative transition on the left/right is a IPES process with/without preceding an electron-hole pair excitation of energy  $\epsilon$ . The electron hole pair can be produced by two quantum-mechanically equivalent channels (broken and continuous arrowed lines) for the same energy level  $E - \epsilon$ . The dashed curve under the solid curve of the observed spectrum represents the inelastic contributions. The spectrum is always plotted in final state energy,  $E - h\nu_0$ .

of final state energy. The detailed definitions are given in Eqs. 9-12 in Chapter 3. The spin quantization axis of the measurement is determined by that of the incident electrons. When the direction of magnetic remanence of thin films is different from the spin quantization axis, it is understood that the projection of the spin polarization in the direction of the magnetic remanence is measured, as long as spin is a good quantum number in the system. Similarly, in the excited states with spin fluctuations, the averaged projection of the local spin polarization is measured. The local magnetization might fluctuate in amplitude and in angle at elevated temperature  $0 < T/T_c < 1$ , and produce characteristic changes in the SPIPES spectra, a topic which will be discussed later.

#### Surface-Sensitivity of IPES

The IPES technique is intrinsically surface sensitive because the impinging electrons are quickly attenuated at shallow depths by elastic and inelastic scattering in the solid. The penetration depth of 10 eV electrons is  $\sim 10$  Å or so, which translates into about 5 atomic layers. According to the surface magnetism calculations it is believed that the electronic and magnetic properties of the surface layer could be profoundly different from the bulk properties, while those of the second layer and deeper are closer to the bulk properties. Therefore, both bulk- and surface-derived features are examined in the SPIPES spectra. Experimentally, besides the bulk electronic structures sampled, the existence of surface states, image-potential states, and other surface features have also been investigated by IPES.

This surface sensitivity feature has allowed us to investigate the evolution of the electronic system to thicknesses up to a few atomic layers. In the present experimental conditions, the polarized electronic structure from

magnetic overlayers are superimposed over a background of non-polarized electronic features of the tungsten substrate. SPIPES measurements as a function of the magnetic film thickness provide a novel microscopic picture of the initial development of ferromagnetism and corresponding electronic properties.

### Angular Dependent SPIPES

As in angle-resolved PES, in IPES detailed information about the electronic states participating in the optical transitions can be obtained by recording the direction together with the energy of the incident electrons. This is because of the  $\mathbf{k}$ -conserving direct-transition nature of IPES, and also because of the experimental feature of a well defined angular distribution of the polarized electron beam.

At the solid-vacuum interface the parallel component  $k_{\parallel}$  of the vector  $\mathbf{k}$  is conserved, and the perpendicular component  $k_{\perp}$  of the vector  $\mathbf{k}$  is not, because of the potential jump across the interface, see Fig. 4. This partially conserving feature of the  $\mathbf{k}$  vector i.e., conservation of  $k_{\parallel}$ , allows us to trace  $k_{\parallel}$  simultaneously with  $E$ . For example, at normal-incidence,  $k_{\parallel}=0$ , while  $k=k_{\perp}$  is collinear with the surface normal, which is frequently chosen a low index crystal axis. If one has reliable knowledge of the initial (higher energy) state dispersions in reciprocal space, determined perhaps by ARPES, the value of  $\mathbf{k}$  inside the solid is determined, and thus the unoccupied final states can be identified. The present work will be focused mainly on normal-incidence spectra.

At an off-normal angle of incidence,  $\theta \neq 0$ , the parallel component of the wave vector is  $k_{\parallel} = [2m(E - E_{\text{vac}})\hbar^{-2}]^{-1/2} \sin\theta$ . The experimental dispersion of the

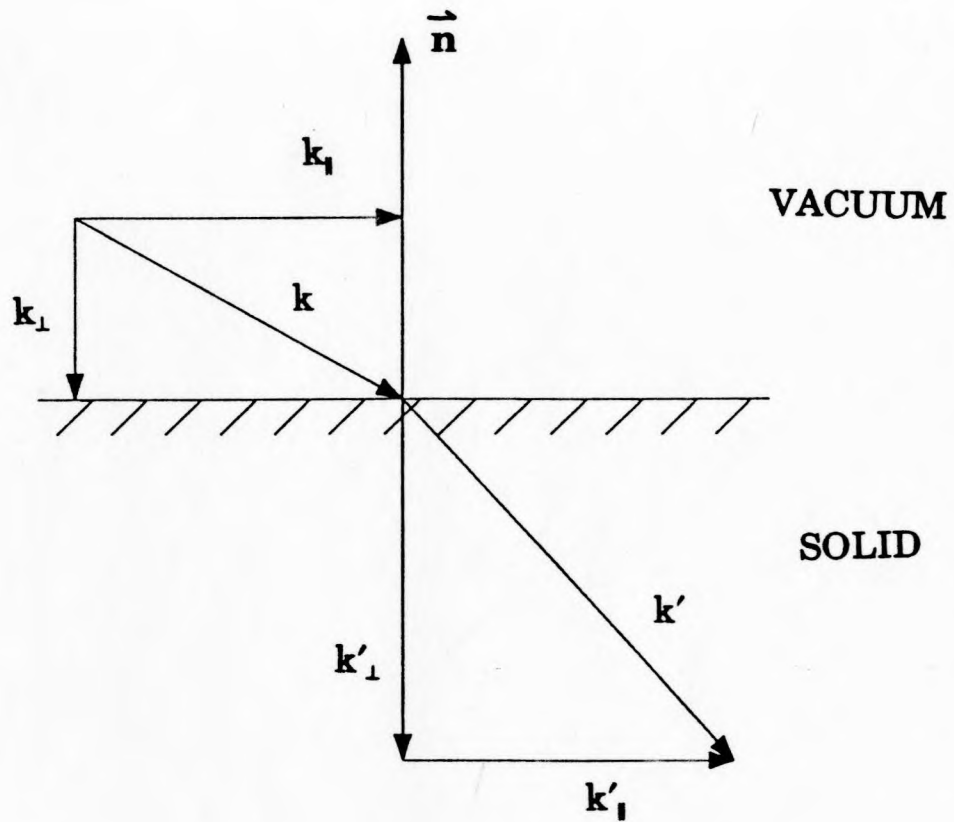


Figure 4. Relationship between  $\mathbf{k}$  vectors across the vacuum-solid interface.



states responsible for bulk or surface features can be plotted with respect to  $k_{\parallel}$ . The surface or overlayer features are intrinsically two-dimensional, and such a dispersion plot will reflect the symmetry of the surface Brillouin zone (SBZ). The bulk electronic structure is often projected to the SBZ to be compared with experimental dispersion curves; this helps identify surface features.

### Experimental Feasibilities

Finally we comment on the experimental difficulties of SPIPES, in contrast with those of IPES and PES. It is long known from studies of the photoionization process and radiative recombination processes in atomic physics that what we call PES and IPES processes differ in transition probabilities by orders of magnitude. It can be seen, by comparing the coefficients of the total cross section obtained from the golden rule that the IPES process is about five orders of magnitude weaker than PES.<sup>16</sup> This low signal may have kept the IPES technique one or two decades behind its counterpart.

In SPIPES it usually takes about ten times more data acquisition time than in ordinary IPES to resolve the spin features from the partially polarized electron beam and from the depolarized background signal. This requirement certainly increases the difficulties of a weak SPIPES experiment. In contrast, spin-polarized PES suffers from the low efficiency of the Mott-type spin detector ( $\sim 10^{-4}$  to  $10^{-3}$  at the best). In this case, SPIPES is not that far behind,<sup>17</sup> and is expected to make important contributions in spin-dependent electronic structure investigations.

## B. The Electronic Structure of Metallic Ferromagnets

### Band Theory of Metallic Ferromagnetism

The zero temperature properties of a 3-d metal magnet are fairly well described by the band theory proposed in 1936 by Stoner.<sup>1</sup> The d-electrons in transition metals are treated as itinerant electrons that interact strongly with each other, and the non-integral Bohr magneton numbers of the 3d-transition metals are easily understood. The exchange-split spin-dependent electron bands are the basis for our understanding of the 3d-transition-metal ferromagnetic electronic structures at low temperatures.

The well-known Stoner criterion predicts that if  $U \cdot N(E_F) > 1$ , the ferromagnetic state is lower in energy than the paramagnetic one, where  $U$  is the intra-atomic Coulomb interaction energy which is responsible for Hund's rules in atoms, and  $N(E_F)$  is the paramagnetic density of states (DOS) at  $E_F$ . When this criterion is satisfied, the DOS becomes spin-split spontaneously, resulting in an excess of electron spins with their magnetic moments parallel to the macroscopic internal magnetic field. Since the electron has a negative charge, the electrons with their spins antiparallel to the direction of internal magnetization are referred to as majority ( $\uparrow$ ) spin electrons, while the electrons with the opposite spin are called minority ( $\downarrow$ ) spin electrons. The DOS of the two groups of electrons is said to differ in energy by the exchange splitting; parameters of selected systems are listed in Table 1.

Table 1. Magnetic Moments in units of the Bohr magneton ( $\mu_B$ ), Exchange-Splittings and Curie Temperatures of Selected 3d Transition Metal Elements

	$T_C^{\text{bulk}}(\text{K})^{[18]}$	$\Delta_{\text{exchange}}^{\text{bulk}}(\text{eV})$	$\mu^{\text{Bulk}} [18]$	$\mu^{\text{Surface}} **$	$\mu^{\text{Adlayer}} ***$
Fe	1043	1.8	2.22	2.98	3.2(3.20 <sup>[19]</sup> )
Co	1400	0.85	1.72	1.95	2.2
Ni	631	0.5	0.606	0.68(0.98 <sup>[3]</sup> )	1.04
V	—	—	NM	0.	3.0(1.98 <sup>[19]</sup> )

\* bulk V is not ferromagnetic (NM)

\*\* calculations for (001) surfaces of a square lattice only, including a bcc-Co structure, from Ref. 19 unless otherwise specified.

\*\*\* monolayer on Ag(100) surface, from Ref. 20 unless otherwise specified.

### Ground State Properties of Fe, Co, and Ni

A magnetic "ground state", strictly speaking, refers to the state with absolutely no magnetic excitations, such as spin waves or other spin-fluctuations, at 0 K. Since the electronic structure and macroscopic magnetic ordering of a bulk system usually do not change rapidly from 0 K to a temperature of a fraction of  $T_C$ , say, at  $T_C/3$ , we are able with reasonable accuracy to compare an electronic spectrum at some experimental temperature  $T \neq 0$  K with a theoretical electronic structure in the ground state.

It is possible to calculate the Stoner electron band structure in great detail for metallic systems like transition metals, as mentioned in Chapter 1. A special characteristic of 3-d transition metals that determines many of their special physical, chemical, catalytic, and magnetic properties is their high density of 3-d band states near  $E_F$ . It is found that the Stoner criterion is

satisfied for bulk Fe, Co and Ni, and the exchange-split electron bands are energetically favored for them.

Taking Fe as an example, in the case of isolated Fe atoms, the two 4s-electrons are paired, and the six 3d-electrons, four of them unpaired, according to Hund's rules, contribute 4 Bohr magnetons ( $\mu_B$ ) for each Fe atom. In the case of the solid  $\alpha$ -Fe, the strongly overlapped 4s-states form bands in a broad energy range, while the 3d-state bands are relatively flat because of the small orbital overlap. Of the 8 valence electrons per atom there are 7.4 electrons with 3d character and 0.6 with 4s character. Further, there are 4.8  $d\uparrow$ -electrons and 2.6  $d\downarrow$ -electron, and the spin-polarization of the s-electrons is negligible. The net result is a  $2.2\mu_B$  non-integral magnetic moment per Fe atom. See Fig. 5.

Shown together in Fig. 5 are the electron distributions of Co and Ni. Their characteristic difference from Fe is that in Co and Ni the majority-spin d-bands are fully occupied, and only Fe has partially unfilled majority spin d-bands, a property which has been observed in the present experiments (Chapter 5). The property of Co, and Ni, that they have only minority unoccupied d-bands, has been used to investigate their minority electronic structures prior to the spin-polarized electron technique, and this should be considered specially in the spin-flip electron-hole creation in inelastic scattering processes. A summary of the Fe, Co and Ni magnetic moments is given in Table 1.

#### Surface Magnetism and 2D Magnetic Systems

At the surface of transition metals, the local DOS can be substantially different from that of the bulk, which suggests different magnetic behavior at the surface than in the bulk according to the Stoner criterion. It has been

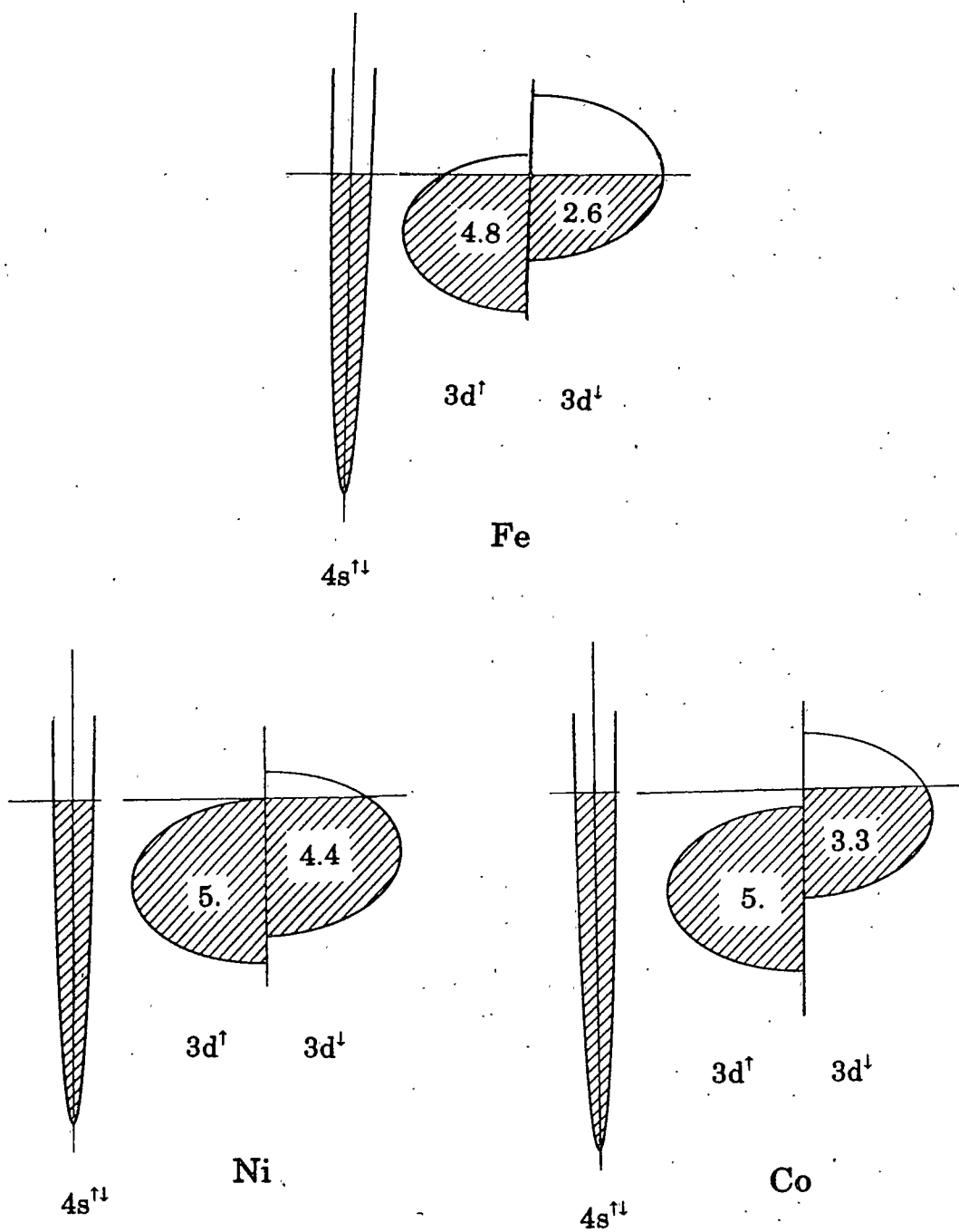


Figure 5, Electron spin distribution in energy bands of Fe, Ni, and Co.

found that Fe, Co and Ni retain their ferromagnetic ordering at the surface, and paramagnetic V, anti-ferromagnetic Cr, and possibly also Mn may acquire ferromagnetic ordering at the surface.<sup>21</sup>

Many efforts have been made in calculational physics to determine qualitatively as well as quantitatively the electronic and magnetic properties at the surface. For example, self-consistent calculations on Ni(100) clean surface and Fe(100) oxygen-chemisorbed surface have been carried out by Zhu and Huang respectively.<sup>22</sup> Because of the reduced symmetry, the calculation for the surface is more difficult and time-consuming than for the bulk. Frequently, a slab model is employed, and the exchange-split electron band structure and the local magnetic moment are revealed in a layer-dependent manner, guided by the asymptotic approach of the inner-plane properties to the bulk properties. Table 1 has included calculated surface magnetic moments for Fe, Co and Ni. As one can see, the Fe surface magnetic moment is predicted to be about  $3\mu_B$ , an enhancement from the bulk value of  $2.2\mu_B$ , yet less than the limit of atomic Fe of  $4\mu_B$ , which is not very surprising since the atomic coordinations for surface atoms (2D) are between the bulk (3D) case and the free atom (1D) case. One can also see that the bulk V and its surface are both non-magnetic, but a monolayer of V is expected to be ferromagnetic with a sizeable magnetic moment. All these remarkable results from first-principles calculations with the precise details of the electronic and magnetic properties have greatly advanced our knowledge of surface magnetism. These theoretical advances have been both a challenge and an opportunity for advanced spin-polarized electronic structure investigations.

While it is difficult to distinguish the contribution from each layer in bulk materials by electron spectroscopic techniques, the magnetic adlayers on top of

a non-magnetic substrate may be a close substitute for an isolated single layer for the surface magnetism study. Recent progress in surface science techniques has given us the means for such study, which requires firm knowledge about epitaxial growth and ultrathin film characterization, a solid foundation that the present work is based on.

There are additional advantages gained by studying magnetic adlayer systems. First, the relationship between magnetism and the geometric structure of 3-d transition metals can be investigated in the case of the adlayers that form various structures on different substrate surfaces. For example, iron forms bcc-Fe on Ag(001) but fcc-Fe on Cu(001). Also, the effect of material atomic density on magnetism can be investigated since the lattice spacing of the epitaxial adlayer can be significantly distorted as a result of the lattice mismatch with the substrate.<sup>23</sup> The itinerant electronic and magnetic properties are intimately related to the geometric structure and lattice spacing. Changes of interatomic spacing in bulk materials are hardly feasible with conventional methods because they require tremendous external pressures. Needless to say, the possibility of varying at will the lattice spacing can greatly increase our progress towards understanding the many-body interaction problem in solids. Theoretical analysis shows that there are phase transitions between the ferromagnetic and paramagnetic states as the atomic density is varied.<sup>5</sup> In particular (related to our Fe/W(001) system), dilation of the lattice spacing in bcc Fe has been predicted to enhance the magnetic moment. Experimental evidence for these effects has not yet been produced.

The importance of studying adlayer systems also relates to more fundamental questions such as the relationship between low-dimensionality and magnetic ordering. Strictly speaking, the surface magnetism of bulk materials

is not a two dimensional (2D) magnetic system because of the interaction from the second layers. There are even arguments questioning the existence of magnetic ordering in a 2D system in a strict sense.<sup>24</sup> While a free-layer system is difficult to realize, it is possible to study magnetic adlayers on a nonmagnetic substrate. Further, superlattice structures can be investigated as a series of 2D systems arranged periodically, with the additional possibilities of investigating the interlayer couplings. Even though obtaining an ideal atomically smooth adlayer is very challenging and material-dependent, this sophisticated ultrathin film preparation technique may eventually provide answers to questions on two-dimensional magnetism, while also promoting the technological progress applicable to thin film devices.

#### Models of Electronic Structures at Elevated Temperature

According to the Stoner model, the exchange splitting is temperature dependent and vanishes as a result of thermal excitations at  $T_c$  when the macroscopic magnetic moment disappears. However, the value of the exchange splitting  $\Delta_{\text{exch}}$  for typical transition-metal ferromagnets is about an order of magnitude too large for the thermal energy  $k_B T_c$  at the Curie temperature to bring the exchange-split bands together when the nonmagnetic phase is reached. See Table 1, and  $k_B = 8.617 \times 10^{-5}$  eV/K is Boltzmann's constant. This, among other deficiencies, indicates that the Stoner theory is inadequate for describing the system at elevated temperatures.

On the other hand, the Heisenberg model can lead to some correct results such as the Curie-Weiss Law above  $T_c$ , but it is not appropriate to use the Heisenberg model in an itinerant system. There have been some variations of the Stoner-type or Heisenberg-type models, including a unified model (see Refs.



25-27 and references cited therein), but no generally accepted microscopic model exists for finite temperatures.<sup>28</sup> A rough pictorial representation of the problem is given in Fig. 6. In the Stoner model the local spin density gradually decreases to zero at  $T > T_c$  when the exchange splitting is also zero. In the Heisenberg model the local spin density does not decrease but fluctuates at  $T > 0$ , and eventually becomes random at  $T > T_c$ . In the so-called unified picture, not only does the local spin density vary with  $T$ , but there exists significant spin correlation which is hard to illustrate in this figure.

The missing ingredient in the Stoner theory is the existence of spin fluctuations which arise at finite temperature and eventually destroy long range order.<sup>25-27</sup> The local magnetic moment is believed to exist even above  $T_c$ . A main controversy in the modern theory of itinerant magnetism concerns the

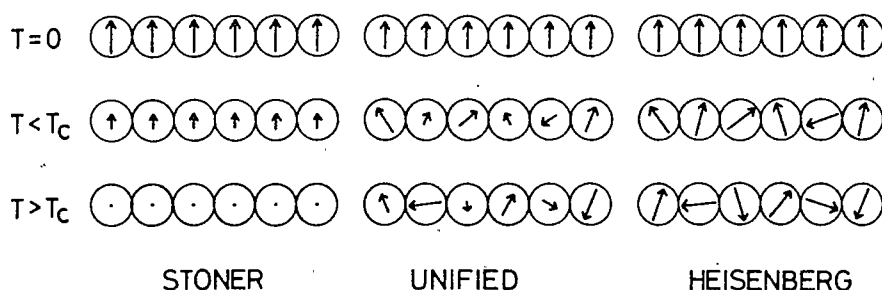


Figure 6. Comparison of the Stoner, Heisenberg and unified models. Adapted from Ref. 27.

wavelength distribution of the spin-density fluctuations, i.e., the degree of short-range magnetic order characterized by a parameter  $\Lambda$  as the spatial correlation distance of spin-density fluctuations. In the opposite limiting cases of the local-band picture or the disordered-local-moment picture,  $\Lambda$  ranges from, say,  $\sim 10\text{\AA}$  to zero, respectively.

It is out of the scope of this thesis to comprehensively discuss the theory. Instead, we will simply sketch the relevant physical pictures of it and how the theory is reflected in the model electron spectroscopies (PES and IPES). The disordered-local-moment picture (DLM) assumes no short-range magnetic order,  $\Lambda=0$ , and since at  $T>T_c$  the itinerant valence electrons "feel" totally disordered local magnetic moments, the corresponding pair of minority ( $\downarrow$ ) and majority ( $\uparrow$ ) spin peaks in the spectrum at certain k-point merge to a central peak or shoulder. On the other hand, the local-band picture, or local-band-theory (LBT), assumes a strong short-range order  $\Lambda$  up to  $\sim 10\text{\AA}$ , and since electrons, except those that are strongly delocalized, "feel" the local magnetic order although it is fluctuating, the local band exists at finite temperature, and results in a decreasing "ordinary" peak, that is, a majority (minority) spin peak at the zero-temperature majority (minority) peak energy, and an increasing "extraordinary" peak, that is a majority (minority) peak at the zero-temperature minority (majority) peak energy. The model spectrum is illustrated in Fig. 7 taken from Ref. 25.

The spectral behavior depends on the degree of localization of electron states involved, or, in terms of a tight-binding approach, the overlap integrals with neighboring atoms. Such analysis involves the wavefunctions, their symmetry and bonding or anti-bonding character of the overlap integrals (i.e. whether the state is on the bottom or the top of a d band). The result can be

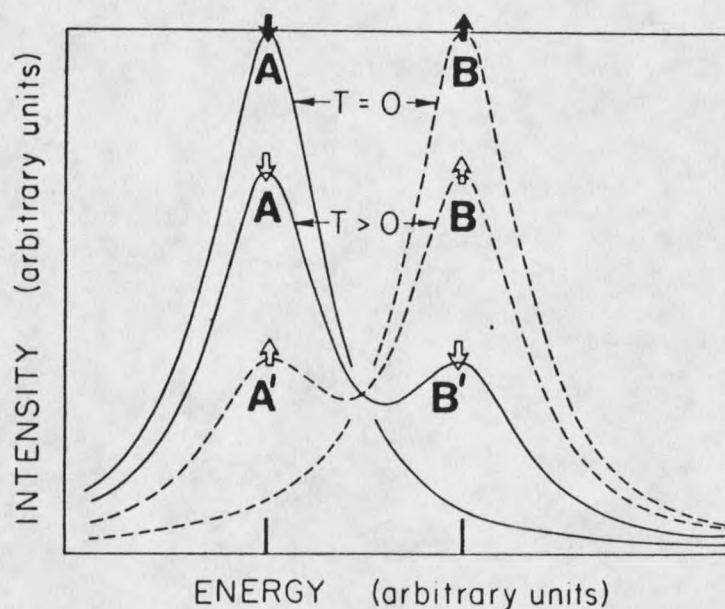


Figure 7, Local-band model spin-resolved PES/IPES spectrum for  $T=0$  K and at an elevated temperature below  $T_c$ . It is assumed that the electrons originate from regions with constant local magnetic moments the directions of which tend to fluctuate around the direction of the spontaneous magnetization at elevated temperatures. The peaks A and B are referred to as "ordinary" peaks while A' and B' as "extraordinary" peaks.

tested by techniques like SPIPES and SP-PES. A systematic study of short-range order in bcc-Fe carried out by calculating temperature-dependent theoretical spectra as a function of the correlation-length of the spin fluctuations has been done by Clauberg et al.<sup>28</sup> and an example at  $\Gamma'_{25}$  is shown

in Fig. 8 taken from Ref. 28.

In Fig. 8, the energies of  $\Gamma_{25}^{\uparrow}$  and  $\Gamma_{25}^{\downarrow}$  at  $T=0$  K are indicated by vertical dashed lines, which are separated by the amount of the exchange splitting of the d-band, while the dotted line marks the nonmagnetic  $\Gamma_{25}'$  energy. The spectra demonstrate the changes in going from the limiting DLM model ( $\Lambda=0$ ) towards the limit of the local-band model. As one can see, for  $\Lambda=5.4\text{\AA}$ , corresponding to short range order, when the magnetization is reduced to  $\bar{M}=0.4M_0$  at  $T=0.85T_c$ , where  $M_0$  is the zero-temperature magnetization, the spectrum shows a significant modification in which two extraordinary peaks develop at the original peak positions. When the magnetic moment  $\bar{M}=0$  at  $T\geq T_c$ , the spin-up and spin-down spectra coincide. With  $\Lambda=0$ , the two peaks at the  $\Gamma_{25}^{\uparrow}$  and  $\Gamma_{25}^{\downarrow}$  energies tend to merge together, showing a continuous reduction of the exchange splitting with increasing  $T$  until  $T\geq T_c$ . The peaks are attenuated and broadened generally with  $T$ , but we will only concentrate on the peak positions.

Experimentally, the spectral temperature dependence is usually obtained by varying  $T$ . However, the key parameter  $T/T_c$  could also be varied by a variation of  $T_c$ , which we believe is possible for the ultrathin film samples. More precisely, it has been found that reduced film thickness may reduce the system  $T_c$ , and as a consequence it may be possible to study behavior associated with increasing  $T/T_c$  by reducing the film thickness, cf. Chapter 5.

Another point that should be borne in mind is that the zero-temperature calculations predict some remarkable enhancement of surface magnetization, although this enhancement may not necessarily exist at finite temperature. The surface and bulk magnetizations behave differently with temperature as shown schematically in Fig. 9. The surface magnetization decreases faster than

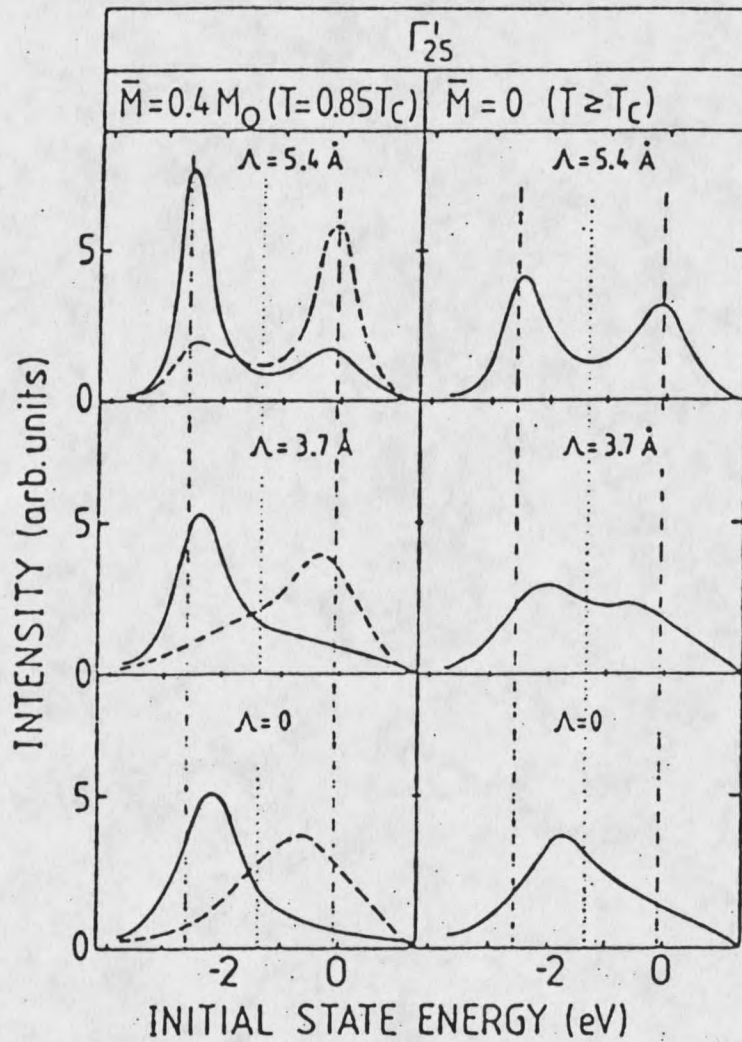


Figure 8. Theoretical spin-up (solid curves) and spin-down (dashed curves) spectra for SP-PES from the bcc-Fe  $\Gamma'_{25}$  states. The vertical dashed lines mark the energies of  $\Gamma'_{25}\uparrow$  and  $\Gamma'_{25}\downarrow$  at  $T=0$ , and the dotted line indicates the nonmagnetic  $\Gamma'_{25}$  energy. The exchange splitting is  $\Delta_2=2.5$  eV.

the bulk even though it is larger at zero-temperature, and therefore a surface magnetic enhancement at zero-temperature could turn into a deficit above a certain temperature.<sup>29</sup> Detailed analysis of this subject, including the very important area of investigating the "critical exponent",  $\beta$ , is outside the scope of this work, and interested readers are referred to other works such as Ref. 29.

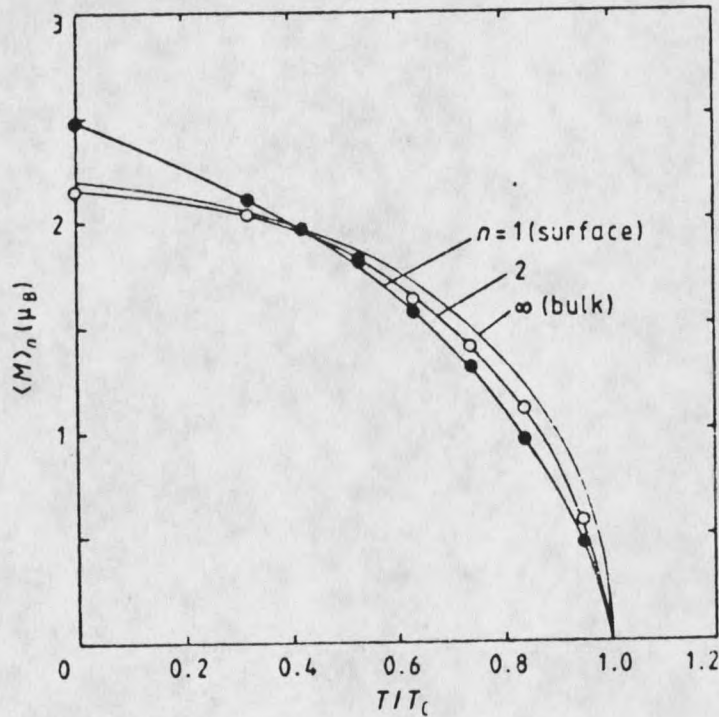


Figure 9. The calculated average magnetization on the surface ( $n=1$ ), the second layer ( $n=2$ ) and in the bulk ( $n=\infty$ ) as a function of the normalized temperature of  $T/T_c$ . Adapted from Ref. 29. The surface magnetization, which is enhanced at  $T=0$  K, decreases more rapidly than the bulk and shows a reduced magnetization above certain temperature.

## CHAPTER 3

## SPIN-POLARIZED ELECTRON SOURCE,

## EXPERIMENTAL APPARATUS AND PROCEDURES

Section A of this chapter describes the construction and operation of the spin-polarized electron source, which is the heart of SPIPES technique. Section B discusses the design and calibration of the modified UV bandpass photon detector, which served as the data collector in inverse photoemission. Section C gives an outline of the experimental system containing AES, LEED, SPIPES, and the apparatus for the magnetic thin film preparation and characterization. Section D deals with the sample preparations procedures. Section E is about the SPIPES measurement techniques.

A. Spin-Polarized Electron Source

The GaAs photo-excited electron source is the most effective way to produce spin-polarized electrons. It can produce tens of microamperes of current; it is ultrahigh vacuum compatible, has small energy spread, and its polarization is easily modulated by optical means. The technique was first demonstrated feasible by Pierce and Meier in 1976,<sup>30</sup> and became a practical device earlier this decade.<sup>31</sup> The spin-polarized electron source built at Montana State University is based on the prototype design at National Institute of Standard and Technology (previously NBS). I am indebted to Dr. Pierce and his colleagues for furnishing me the drawings. A detailed discussion of this

polarized electron source, its design, and comparison with other types can be found in Ref. 31, and the references cited therein. A brief summary of the design principle and particularly the performance characterization at this lab will be presented here.

### Spin-Polarized Photoelectron Emission from GaAs

The cathode material is a heavily doped p-type GaAs semiconductor single crystal. The valence band maximum (VBM) and the conduction band minimum (CBM) near the center of the Brillouin zone ( $\Gamma$  point) have p- and s-wavefunction symmetries, respectively. As Fig. 10 shows, the direct band gap between CBM and VBM is 1.52 eV, and the valence bands are split by spin-orbit coupling into a  $P_{3/2}$  level and a lower  $P_{1/2}$  level, separated by 0.34 eV.<sup>31</sup>

The photo-excitation process is governed by quantum mechanical selection rules. Let the direction of light be the spin quantization axis. The right-hand circularly polarized light, or helicity  $\sigma^+$ , will only excite electrons between sublevels with  $\Delta m = m_f - m_i = +1$ , and left-hand circularly polarized or  $\sigma^-$  light will only excite electrons between sublevels with  $\Delta m = m_f - m_i = -1$ , as indicated on the right of Fig. 10 by the solid lines and dashed lines, respectively. The ratios of the transition probabilities between each sublevels at  $\Gamma$  are readily calculated by substitution of corresponding atomic wavefunctions into transition matrix elements, and the results are shown in circles.<sup>30</sup>

By selecting the proper excitation wavelength, one can excite only electrons from the  $P_{3/2}$  level into the conduction band. For example,  $\sigma^+$  light causes transitions from  $m_j = -3/2$  to  $m_j = -1/2$ , and  $m_j = -1/2$  to  $m_j = 1/2$ , (solid lines in Fig. 10) with an intensity ratio of 3 : 1. The spin polarization is defined as



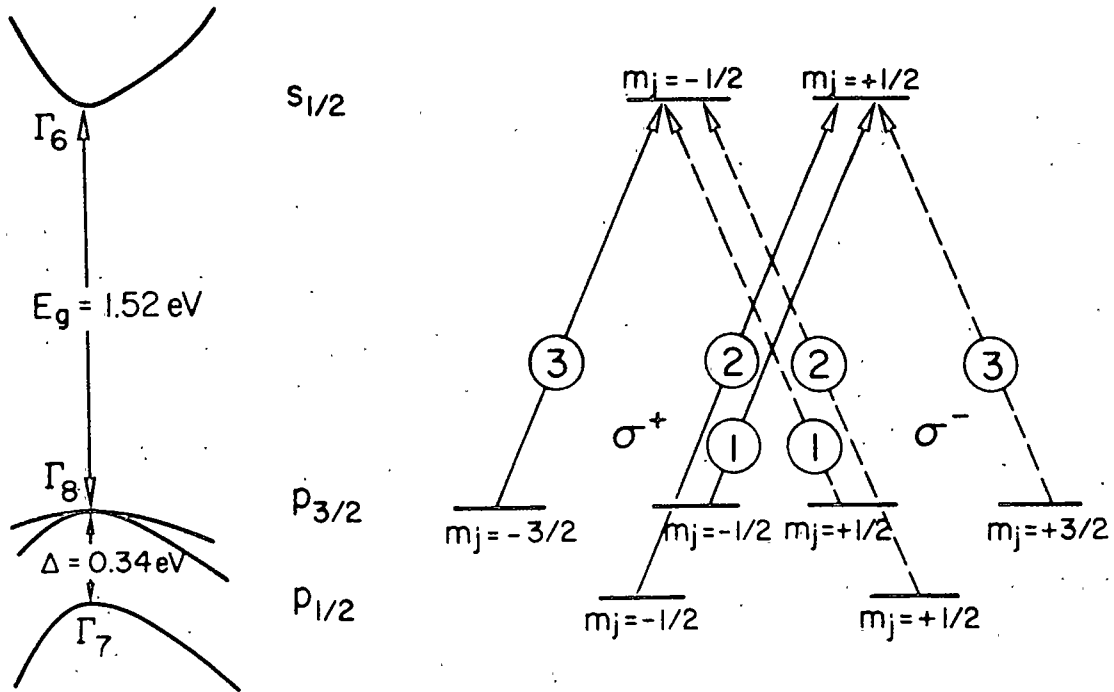


Figure 10. Left: the energy bands of GaAs near the center of the Brillouin zone, with the direct band gap of 1.52 eV and the spin-orbit splitting of the valence bands of 0.34 eV. Right: the allowed transitions between  $m_j$  sublevels for circularly polarized light,  $\sigma^+$  (solid lines) and  $\sigma^-$  (dashed lines), with the relative intensities shown by the numbers circled. Adapted from Ref. 31.

$$P = (n\uparrow - n\downarrow) / (n\uparrow + n\downarrow) \quad (8)$$

where  $n\uparrow$  and  $n\downarrow$  are the number of electrons with spins parallel and antiparallel to the light propagation direction respectively. Thus for  $\sigma^+$  light, a net spin-polarization of the excited electrons,  $P = -50\%$  is estimated theoretically. With  $\sigma^-$  light, the corresponding transitions with reversed spin sign (dashed lines in Fig. 10) take place, and  $P = +50\%$ . While a photon energy too small (below the band gap threshold) cannot cause the photo-excitation process at all, a photon energy too large may involve the  $P_{1/2}$  level ( $\Gamma_7$  band) into transitions and cause the net spin polarization to diminish.

The feature that the polarization of the electrons is easily reversible by reversing the helicity of the light without affecting the intensity and the direction of the emitted electrons, makes it very attractive for many experiments where it is essential to compare opposite spin polarization measurements under the same condition at the same time.

For the excited electrons at CBM to migrate to the surface and eventually escape out into the vacuum, p-type GaAs is used and the surface is treated with cesium and oxygen. The valence and conduction bands of p-type GaAs bend downwards in energy at the surface; the Cs-O overlayer lowers the surface work function below the bulk CBM to produce an effective negative electron affinity at the surface, see Fig. 11. Electron affinity is the energy difference from the vacuum level  $E_{vac}$  to CBM in semiconductor materials. It is clear from Fig. 11 that only electrons excited to the bulk conduction band and subsequently transported to the surface without significant energy loss can escape. The light penetrates much further into the bulk than the width of the

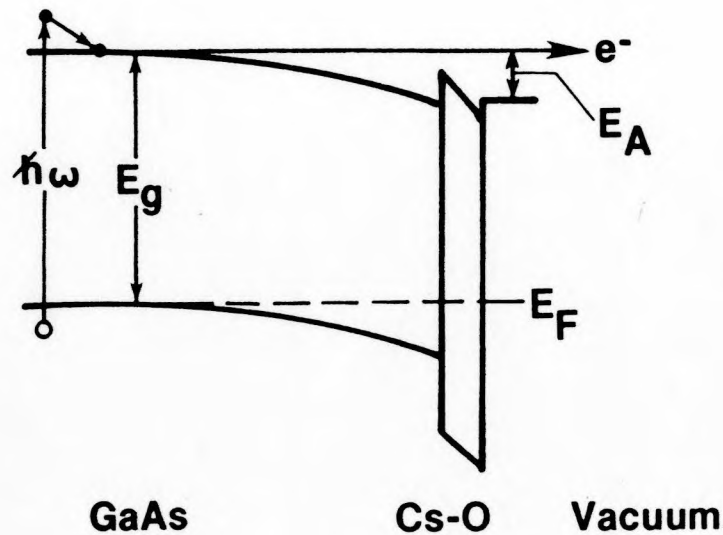


Figure 11, The valence and conduction bands of p-type GaAs bend downwards in energy at the Cs+O treated surface.  $E_g$  and  $E_A$  represent band gap energy and electron affinity, respectively.

band-bending region and excited electrons can diffuse much further than the width of the band-bending region. Therefore photo-excited electrons can readily escape, yielding a high photoefficiency.

The actual polarization of the electrons emitted from the surface turns out to be much less than the theoretical value of 50%, since depolarization processes may occur during the transport as a result of spin relaxation from defects in GaAs besides the instrumental imperfections such as the imperfect

circularity of the polarized light. Also, spin-exchange scattering with the Cs overlayer may reduce the effective polarization. Detailed discussion of the various depolarization mechanism can be found in Ref. 30.

An advantage of this type of GaAs photoelectron source is its small energy spread because of the low thermal energy and the small energy window between CBM and surface  $E_{vac}$ . No additional monochromator is needed. An electron beam of high monochromat brightness is obtained at low kinetic energy.<sup>31</sup> For applications like spin-polarized inverse photoemission where high-intensity, low-energy, and monochromatic beam are required, such a source becomes very useful.

#### Construction of Polarized Electron Source

The polarized electron source is mounted in a four-inch UHV source chamber, pumped by a 60 l/s triode ion pump and titanium sublimation pump (TSP), with base pressure in low  $10^{-10}$  Torr range. The polarized electrons are formed into a beam, then transported to an experimental chamber to perform inverse photoemission and low energy electron diffraction experiments. The source chamber and experimental chamber are mu-metal shielded since stray magnetic fields may destroy the spin polarization by precession. Ion pumps are placed at a distance away from the electron beam. A molecular cesium source is connected to the chamber by a shutoff valve. An oxygen bottle is also connected through a leak valve. An infrared (IR) optical bench is mounted horizontally outside a 2- $\frac{3}{4}$  inch viewport. See Fig. 12.

The p-GaAs crystal cathode material<sup>32</sup> is mounted between a pair of Ta holders which serve both as electrical contacts to the cathode and as current leads for resistively heating the crystal. The crystal is attached to a

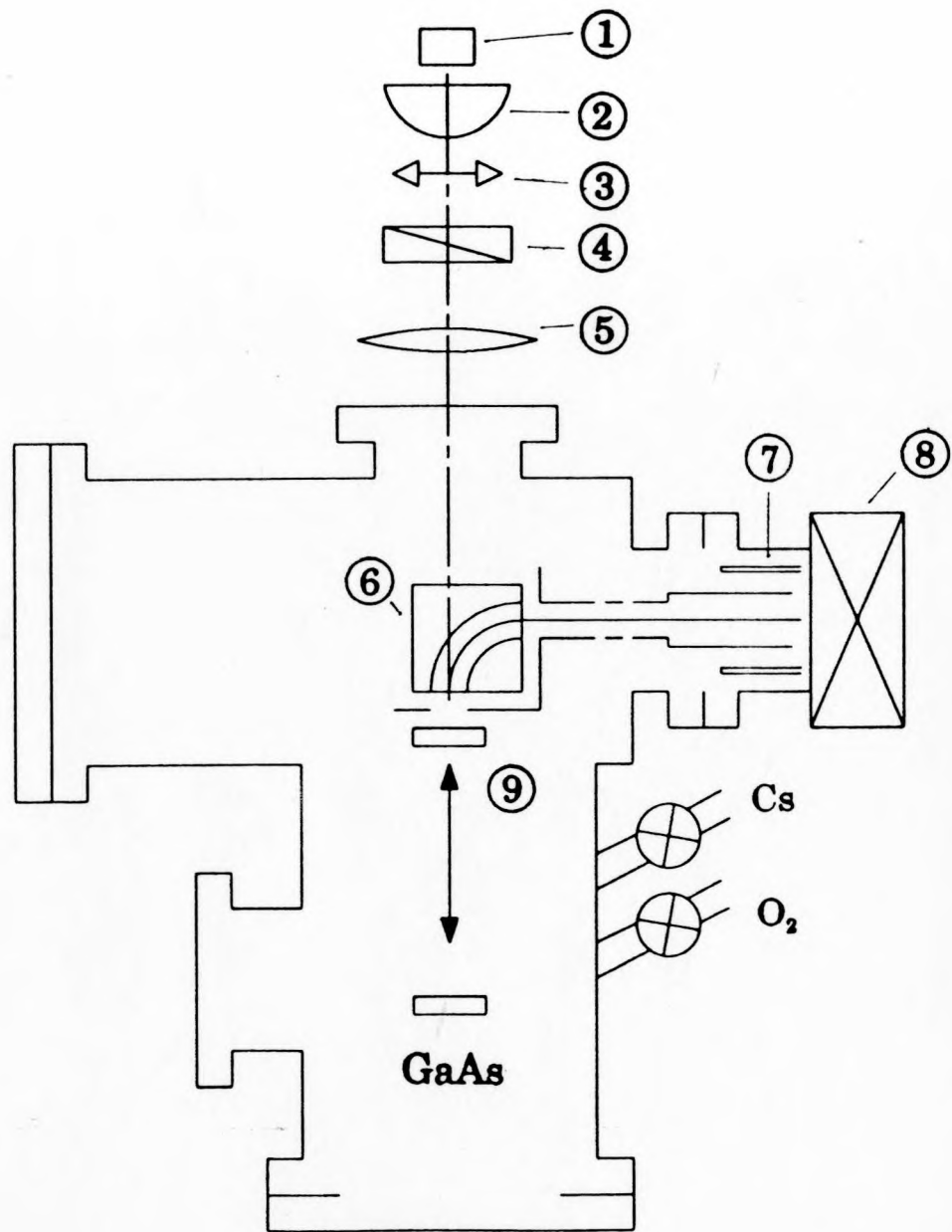


Figure 12. Schematic of polarized electron source chamber: 1: laser diode; 2: aspheric lens; 3: polarizer; 4: quarterwave plate; 5: focusing lens; 6: quarterspherical deflector; 7: sliding tube across 8: isolation valve; 9: cathode emission position and activation position.

manipulator with XYZ motion and rotation, which provides motion of the cathode between emission and activation positions. The cathode temperature is measured by a chromel-alumel thermocouple spotwelded on side of the Ta mount outside the GaAs crystal.

The electron optics in the source chamber are integrated on a 6-inch Conflat flange. The electron optics in the experimental chamber are mounted on a 2- $\frac{3}{4}$  inch double-sided flange. The two sections of the electron optics in the two chambers are connected by an Ag-plated sliding tube, also  $\mu$ -metal shielded, moving inside the isolation gate-valve. This valve, when closed separates the two sections of the chamber from each other; when open permits passage of the electrons.

As shown in Fig. 12, the infrared optical bench is on a side port of the source chamber and pointing at the cathode. A GaAlAs laser diode<sup>33</sup> emits light at about 8000 Å wavelength to excite photoelectrons from p-GaAs crystal. The light beam is formed into a parallel beam by an aspheric lens, then transformed to a circularly polarized beam by a linear polarizer and a quarterwave plate, and then focused on the crystal surface through a vacuum viewport and a hole in an electrostatic deflector. The quarterwave plate replacing the Pockels' cell in the original design simplifies the collimating and the tuning of the multi-kilovolt modulation control of Pockels' cell. The spin polarization resulting from a static circularly polarized light should also be superior to that from a time-average portion of an AC modulation, usually a sine wave. The helicity is reversed by rotating the quarterwave plate by 90°. The ellipticity of the circular polarization is tested by rotating another linear polarizer after the quarterwave plate and recording the periodic intensity variation, for example, by the photoelectron intensity. When the minimum

intensity change is achieved the light is quite close to be circularly polarized.

Figures 13 and 14 show the basic electron optical design in two sections in the source chamber and experimental chamber, respectively. The electrons are emitted into a cone, extracted at the surface normal direction by the first anode which accelerates them to 250 eV kinetic energy. The electrostatic quarter-spherical deflector bends the beam by  $90^\circ$  in the horizontal plane. Therefore, the electron beam is out of the path of the incoming light, and also the beam polarization is changed from longitudinal to transverse relative to the direction of motion. This configuration is more convenient for experiments where near-normal electron incidence and in-plane spin measurements are desired.

The quarter-spherical deflector also focuses electron beam in both directions in and perpendicular to the deflecting plane. Then the electron beam is steered in a constant-energy drifting region by two sets of x-y steering plates, accelerated to 1000 eV and focused to a parallel beam passing through the isolation valve so as to enter the experimental chamber. In the experimental chamber, Fig. 14, the electrons are decelerated, focused, and then passed through a drifting tube placed in the center of a set of Varian LEED screens. Finally the polarized electrons are retarded and focused by an additional retardation stage in front of the LEED optics and then impinge on the sample target, see Fig. 14.

The electrical potential of the lens system is designed to float at the potential of the GaAs cathode; thus, the focusing properties are retained when the beam energy is varied by varying the cathode potential. The beam voltage may vary from 500 eV to 5 eV without losing the beam substantially.

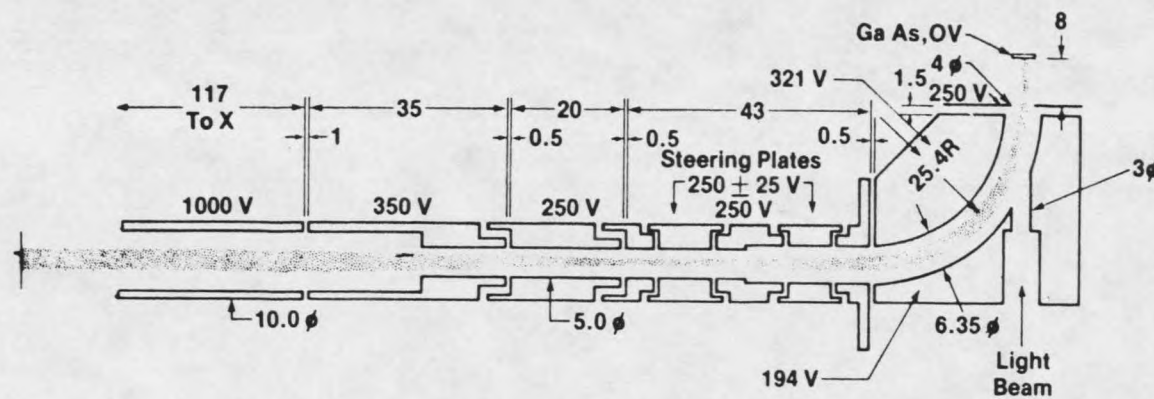


Figure 13. Schematic of the electrostatic lens design in the source chamber.



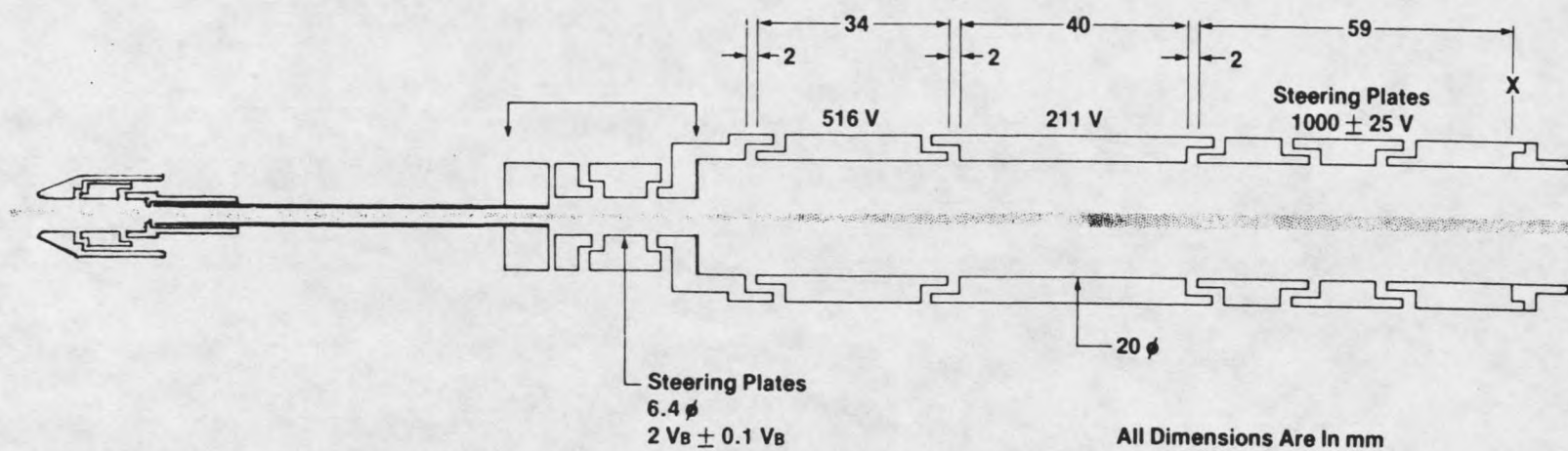


Figure 14. Schematic of the electrostatic lens design in the experimental chamber.

### Operation of the Polarized Electron Source

The operations of GaAs photoelectron source include crystal cleaning,  $\text{Cs}+\text{O}_2$  activation, efficient beam transport, and stable beam operating.

The cathode material was cut to a 6mm×10mm rectangle from a polished p-GaAs(100) crystal wafer.<sup>32</sup> The crystal was first degreased, then etched and passivated right before being inserted into the vacuum. The chemical etching recipe and procedures are described in detail in the Appendix of Ref. 31. Teflon tweezers are recommended because of its resistance to corrosion in the etching solutions.

After the source chamber has been pumped down, baked out, and outgassed thoroughly, and the chamber has reached good vacuum, the crystal may be cleaned further by annealing it to remove contaminations on the surface. The higher the annealing temperature, the cleaner the surface, and consequently, the better the activation as long as the surface was not damaged in the process. This requires a careful monitoring of the GaAs temperature. During annealing, Ga and As atoms are desorbed in equal amount. If, however, the annealing temperature is too high, permanent damage will be made by the formation of metallic Ga droplets on the surface because more As is desorbed. The exact surface melting temperature was not possible to measure since the thermocouple was not directly attached to the crystal, but it is believed to be around 660°C for GaAs(100) surface, suggested by our IR pyrometer and thermocouple measurements and published data.<sup>31</sup>

To learn the proper activation conditions, it was necessary to repeat the activation procedure at progressively higher annealing temperatures until obtaining a satisfactory photo yield before ruining the surface. We noticed that

GaAs crystals before melting actually glowed faint orange when viewed in a dark room. This visible glow could be used as the most reliable indication for the annealing temperature. A uniform resistive heating is achieved by using an AC current. The DC current causes uneven heating between the two metal-semiconductor contact points because of the diode effect. Typical current for a  $10 \times 6 \times 0.35 \text{ mm}^3$  crystal is about 1.9A.

The crystals were allowed to cool down naturally after annealing. This cooling took a few minutes before the crystal was ready to cesiate, since Cs could not stick on the surface at a temperature above  $\sim 50^\circ\text{C}$ . The crystal was placed in the retracted position above the nozzle of a Cs molecular source, consisting of a high purity Cs source ampule heated at about  $80^\circ\text{C}$  and prepumped by a 50 l/s turbo molecular pump to high vacuum prior to open the shutoff valve entering the source chamber (cf. Fig. 18 in section C).

The photoemission current was monitored during the activation process to be able to follow the course of the activation and judge its progress. White light from an incandescent lamp was used for this purpose in the earlier stages of activation, since the surface work function is then too high for excitation by the infrared source. Cesium is applied very early when the crystal is still hot to achieve the best result.

Typical activation process is shown in Fig. 15. At the beginning there is a small amount of thermionic emission when the crystal is still hot, which stops as the sample temperature cools down. When the temperature is low enough to allow Cs to stick on GaAs surface, the photoemission current picks up. A white light or the visible red light from HeNe laser is used during the initial stage of cesiating when the surface work function is still too high for the infrared laser until the cathode shows emission from the infrared. The Cs

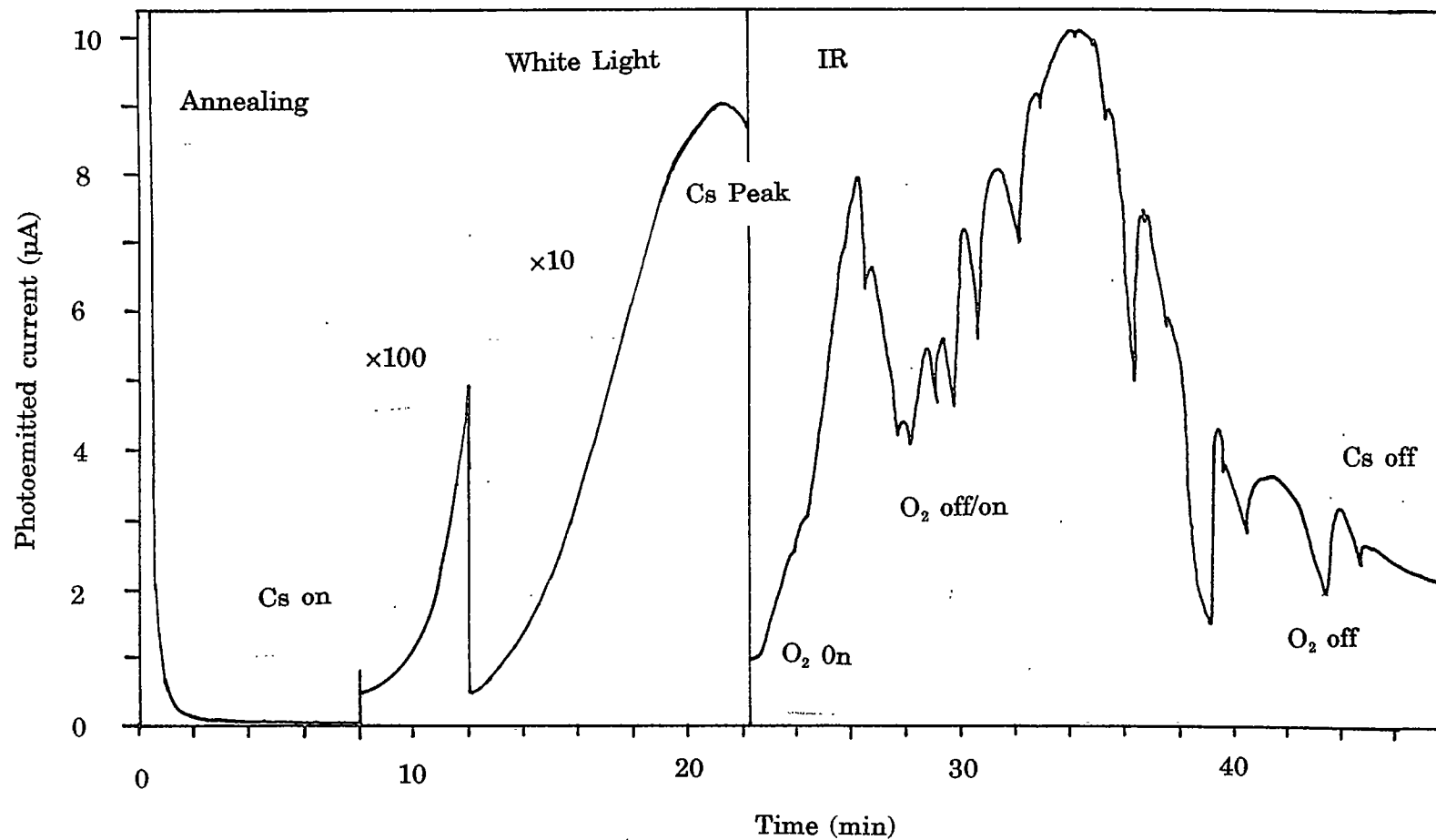


Figure 15. Typical activation curve for GaAs photoelectron source.

application is continued until a plateau in the emission current is reached, then a small amount of  $O_2$  is leaked in. The  $O_2$  pressure should be kept in the low  $10^{-9}$  Torr range, because overdosing with oxygen can kill the activated cathode and another annealing will be needed. The Cs and oxygen applications are continued alternatively until little gain can be made. The activation process is terminated with a small amount of excess Cs. Then the cathode is placed to the front of the first anode where photoelectrons can be brought into the experimental chamber.

Optimizing the beam is very important from the practical point of view. The photocurrent yield varies from point to point on the crystal surface, no doubt because of the non-uniform annealing temperature on the surface. The transport of electrons through the electrostatic lens system is done stage by stage guided by monitoring the absorbed current on each lens piece. In our system, over 60% transmission ratio, i.e., the target current divided by the emission current, has been obtained at low kinetic energy. The working current for SPIPES measurements was set to be 1.25  $\mu A$  at the target and 4.0  $\mu A$  emission current at the source. A small adjustment of IR laser intensity periodically was enough to maintain the current at a constant measurement condition. Lifetime of the cathode was about 4 hours before another cesiation, and one week before another annealing. It was always possible to repeatedly clean the surface and to reactivate the cathode, so long as the GaAs surface was not damaged by overheating during annealing.

A large amount of emission current from a cesiated surface ( $>50\mu A$ ) is observed during the initial stages of annealing. This is attributed to the thermionic emission across the small or negative electron affinity GaAs surface because the Cs and O are not yet desorbed from the surface. This emission

rapidly disappears above a critical temperature estimated to be 200-300°C. No attempt is made to carry out thermal desorption experiments on this activated surface to investigate this interesting phenomenon.

No attempt was made to measure the absolute electron spin polarization in our system, since no spin polarization detector was available. However, a polarization  $P = 27\%$  is believed a reliable figure. This estimate is based on measurements of other investigations, who used the same cathode material at room temperature and the same light excitation.<sup>34-36</sup> This value was used analyzing data through this thesis.

The electron beam energy spread is measured to be in the range of 150 to 200 meV. Caution should be employed when using high emission currents near space-charge limiting operation which might degrade the beam energy resolution.<sup>36</sup>

### B. Bandpass Photon Detector

The photon detector basically consists of a KBr-coated Channeltron<sup>37</sup> which has a near-UV photon response from ~7.5 eV up and a  $\text{CaF}_2$  (or  $\text{SrF}_2$ ) window which only allows photons below its ~10 eV cutoff energy to be detected. The detector has high quantum efficiency, short deadtime, moderate resolution, compact size, modest cost, and ease of operation. By means of a flexible coupling the detector can be positioned close to the sample target for large acceptance solid angle.

Figure 16 shows the detailed diagram of a working detector along with the electric circuit. The Channeltron was fastened to a Teflon holder and then placed in an one inch diameter demagnetized stainless steel tube. In front of

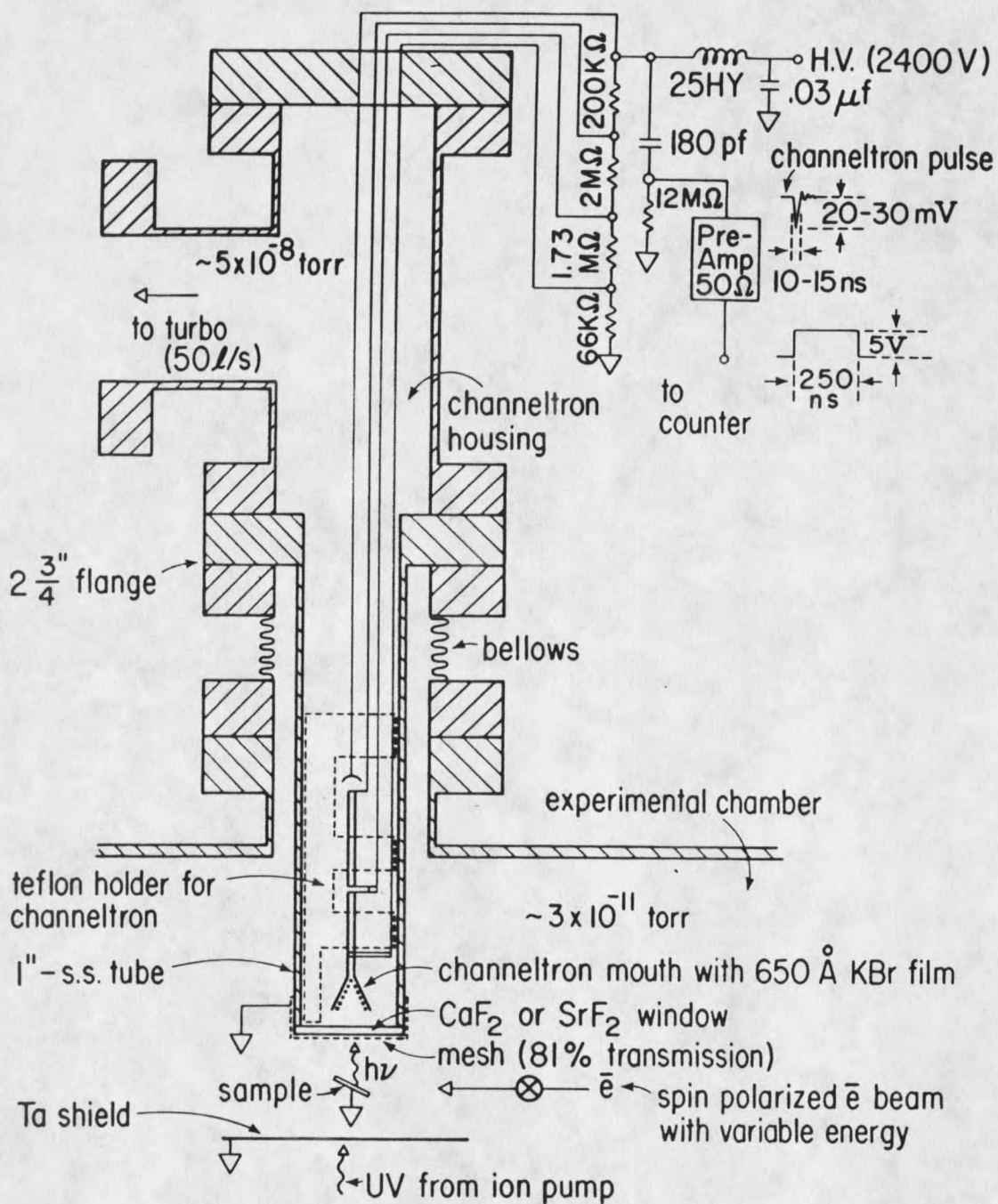


Figure 16. Diagram of Channeltron bandpass photon detector.

the tube was the 2 mm thick  $\text{CaF}_2$  disk,<sup>38</sup> masked by a copper ring. To prevent window from charging, a fine mesh of 1 mil thick tungsten wires, of 81% transmission, covered the window area. The window was sealed vacuum-tight using Torr-seal epoxy so that no charged particles could enter the tube and be detected. This eliminates the problem of large background counts.

The active detecting area of the 9 mm Channeltron cone was covered with ~650 Å film of KBr to enhance the photon detection yield. The coating was evaporated from a Ta boat in a separate vacuum system. Exposure to moisture was carefully avoided before placing the Channeltron in the vacuum. The coating seemed stable, and no deterioration was found after repeated operation.

The detector works in the pulse counting mode. With a typical operation voltage of 2400 volts, an ultraviolet photon generated a negative pulse about 20-30 mV high and 10-15 ns wide. An extra LC circuit is used to isolate ripple noise from high voltage DC power supply. The narrow pulse width could meet the demand of very high counting rate. Channeltron pulses were amplified to standard TTL signal level by a custom designed preamplifier, which also stretched the output to a 250 ns wide square pulse. A threshold adjustment in the preamplifier is used to eliminate the noise and to reduce the dark-counts to below 2 cps level.

A typical IPES signal level as high as 800 cps was obtained for the clean W sample. The detector must be shielded against stray radiation from ion pump or ion gauge. For a system pressure higher than  $1 \times 10^{-9}$  Torr the UV radiation generated in the ion pump becomes a serious problem. A better vacuum in the low  $10^{-10}$  Torr range or a turbomolecular pump is recommended to ensure low dark counts for the IPES measurement, which intrinsically has low count rates.

The absolute spectral response of the detector was measured with the use



of synchrotron radiation from the 800 MeV electron storage ring at the University of Wisconsin's Synchrotron Radiation Center. The radiation was dispersed with a modified Seya-Namioko monochromator operated with a resolution of better than 15 meV. Figure 17 shows the light intensity curve (intensity vs. photon energy), the detector response with a  $\text{CaF}_2$  window and with an additional  $\text{SrF}_2$  window, respectively, and the spectral sensitivity curves obtained by dividing the response curves by the light curve.<sup>39</sup> The detector with  $\text{CaF}_2$  window has maximum quantum yield of 18% at 9.8 eV photon energy and full width at half maximum (FWHM) of 1.6 eV, and the  $\text{SrF}_2$  with a lower cutoff has maximum quantum yield of 6% at 9.7 eV and FWHM of 1.4 eV.

The Channeltron-type detector eliminates the problem associated with preparing ionization gas chamber such as  $\text{I}_2+\text{He}$  mixture used in Geiger-Muller counter. The detector described here is easy to make and essentially maintenance-free once placed in the UHV system. If desired, more than one detector can easily be used. The resolution is demonstrated at least good enough to measure the energies of the exchange splitting d-band states of Fe and Co, but perhaps insufficient to resolve that of Ni in the SPIPES spectra. In contrast to the dead time of the widely used Geiger-Muller counter, the Channeltron-type detector has a short dead time in tens of nanosecond ( $10^{-8}$  sec) which allows a superior counting rate.

### C. Experimental Chamber

The layout of experimental system dedicated to spin-polarized spectroscopic investigations is shown in Fig. 18. On the left is the source chamber, whose

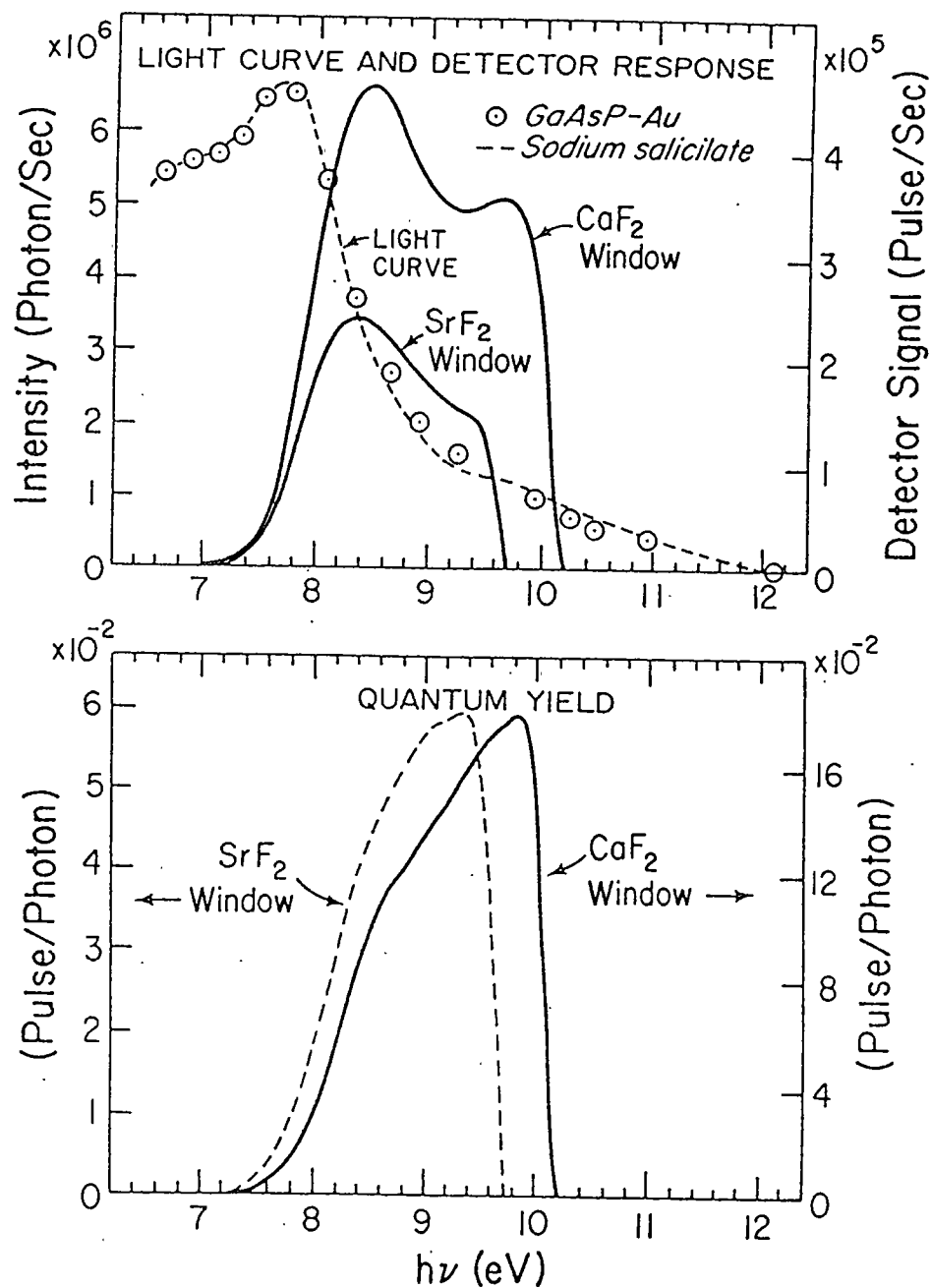


Figure 17. Spectral response measurement. Top: light spectral intensity curve and the detector responses from a Channeltron photon detector with a CaF<sub>2</sub> window or a SrF<sub>2</sub> window. Bottom: the absolute quantum yields for the two types of detector.

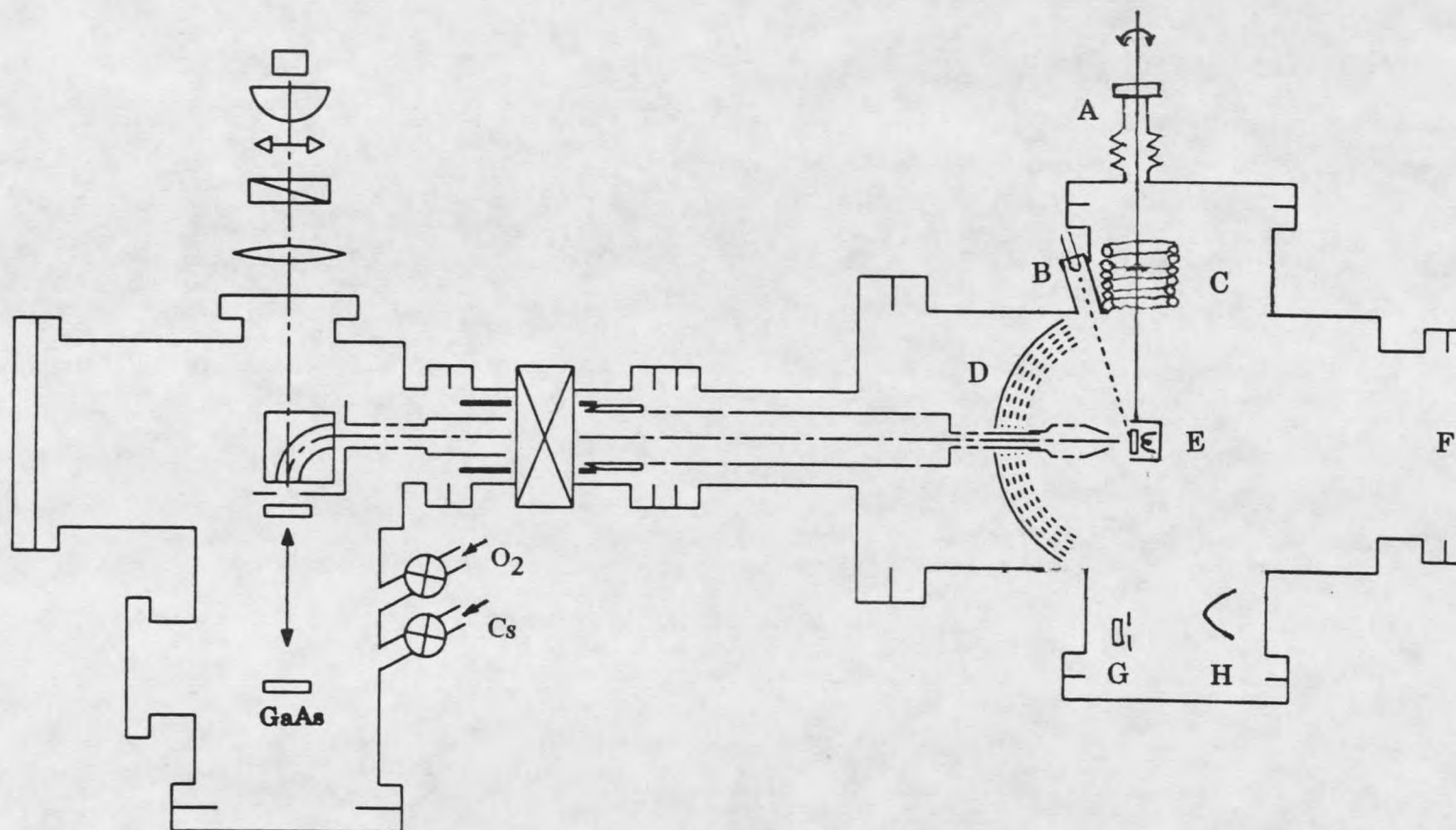


Figure 18. System layout. Left: the source chamber; right: the experimental chamber, A: XYZ motion plus Z-rotation sample manipulator, B: Auger electron gun, C: magnetization solenoid, D: LEED optics, F: sample holder; F: LEED viewport, G: QCO monitor, H: evaporator(s).

design and operation have been described in Section A. On the right is the experimental chamber containing sample materials and a number of analyzing instruments, including the photon detector, the spin-polarized electron gun, a LEED optics, Auger electron gun. The chamber is pumped by a 140 l/s ion pump and titanium sublimation pump (TSP). The base pressure measured by a nude ion gauge is maintained in the low  $10^{-11}$  Torr. A quadrupole mass spectrometer and a 50 l/s turbomolecular pump are connected outside the main chamber by a metal valve for use in vacuum diagnosis and other tasks such as pumping out Cs source, oxygen gas manifold<sup>40</sup> and during system bakeout. A leak valve lets a controlled amount of oxygen leak into the experimental chamber, mainly for the purpose of cleaning the W crystal.

The Perkin-Elmer four-grid 6-inch  $120^\circ$  LEED optics is assembled on an 8-inch Conflat flange on one end of the cylindrical chamber body. The polarized electron beam goes through the center of LEED optics. The (spin polarized) electron diffraction patterns were viewed from a 6-inch viewport directly opposite to the screen.

The LEED optics are also used as retarding-field energy analyzer for Auger analysis (RF-AES). A flowchart of RF-AES measurement using lock-in technique is provided in Fig. 19. A modified electron gun with a tungsten filament provides 5  $\mu$ A beam current at  $\sim 2.5$  keV kinetic energy for Auger excitation since the polarized electron beam can not go beyond 500 eV kinetic energy. The Auger gun is mounted on a port with  $\sim 75^\circ$  angle from the sample normal providing a grazing angle of incidence. This geometry improves the surface sensitivity for analysis of the thin film overlayers. Differentiated energy distributions of electrons emitted from the sample are analyzed by ramping the retarding grid potential while the sample is modulated by a 6-8 V

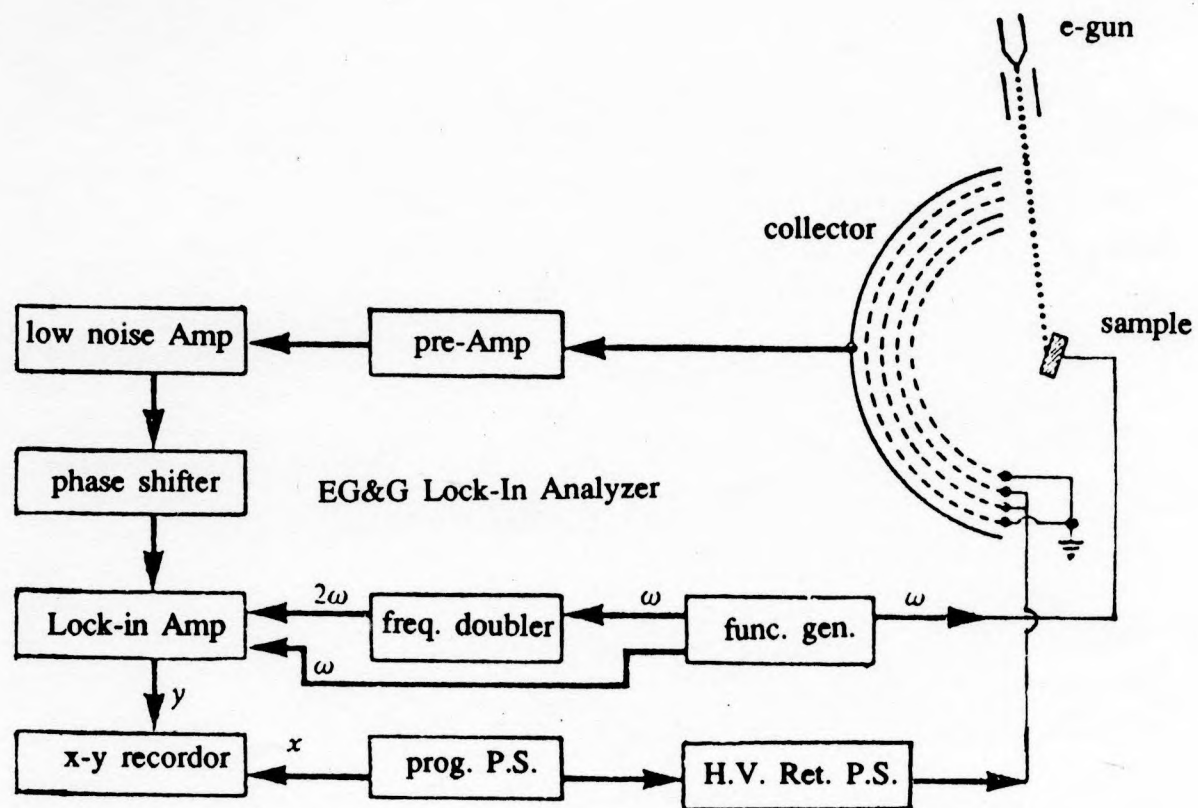


Figure 19. Flowchart of four-grid retarding-field Auger spectroscopy. The top six function blocks are contained in the EG&G Lock-in Analyzer, and the bottom two blocks of power supplies are in the Perkin-Elmer ESCA-AES control unit.

peak to peak AC signal. The RF-AES signal is detected using the double-frequency mode in the lock-in amplifier.<sup>41</sup>

A sample manipulator with x,y,z motion plus rotation about the z-axis is mounted on one side of the chamber, see Fig. 18 and the perspective view of the geometry in Fig. 20. The manipulator provides 5-5/8 inch total z stroke in the horizontal plane perpendicular to the polarized electron beam, which allows the sample to be extended to thin film deposition area and retracted into a magnetizing coil. Rotating the sample about the z axis while facing the polarized electron beam permits angle-resolved SPIPES measurements.

The sample holder design is shown in Fig. 21. The crystal is housed in a cubic housing made of tantalum metal, and is heated using e-beam heating from a tungsten filament placed in the back of the sample. Next to the sample housing is built another cubic housing with a mesh and a phosphor screen. The mesh is kept at the sample potential, mostly grounded, and the phosphor screen is at ~1000 V. The separation between the mesh and the phosphor screen is ~ 1mm. This allows to visualize the spot profile without disturbing the beam trajectory of low energy, 5-20 eV. By using this spot-detector, the size of the polarized electron beam was optimized for the measurement condition. Usually an elongated beam spot was found when the beam current was optimized.

#### D. Sample Preparation

A W(001) crystal ribbon is used as the substrate of the magnetic thin film deposition. The ribbon was made from a slab that was first diamond-sawed from a single crystal ingot,<sup>42</sup> mounted on a goniometer, oriented within 1° by X-

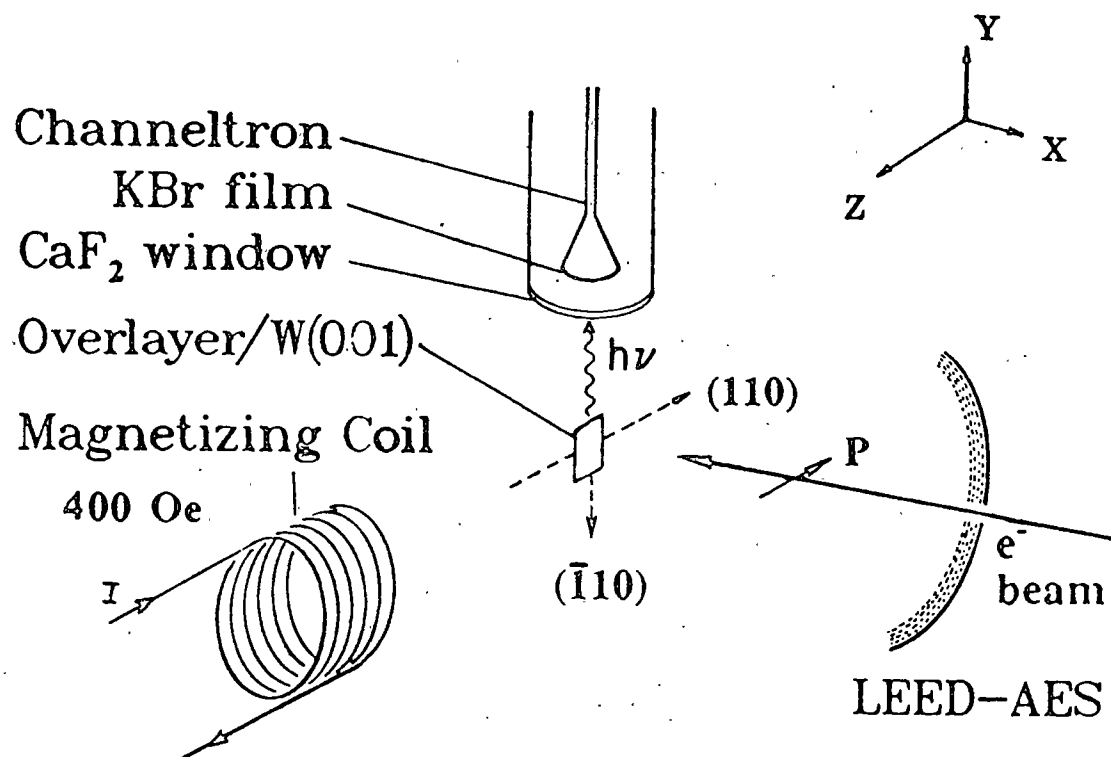


Figure 20. Perspective view of the experimental geometry.

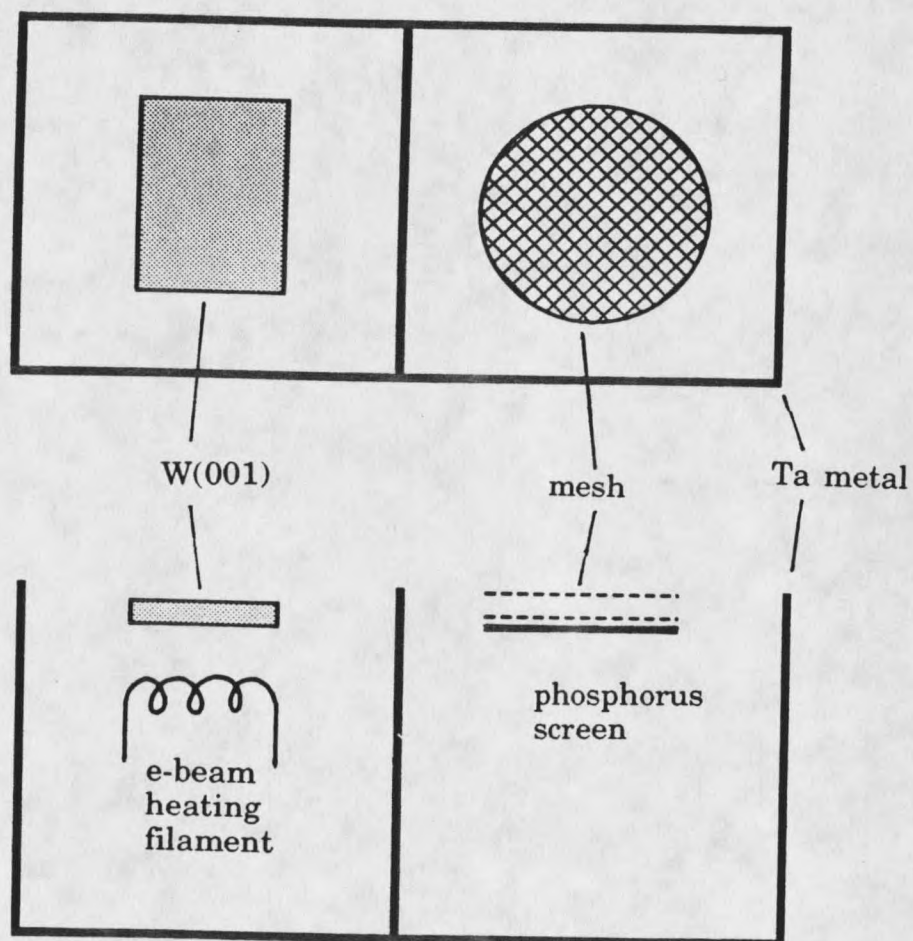


Figure 21. Sample holder and spot detector, Top: front view, bottom: side view.



ray Laur pictures. It was then ground and mechanically polished to a mirror-like finish. One side of surface was electrochemically etched in 30% NaOH solution to remove the damaged surface layer. The crystal was spotwelded on a Ta wire which provided support and electric contact.

A  $p(1 \times 1)$  LEED pattern was observed after flashing the tungsten crystal to  $\sim 2300^\circ\text{C}$  in the vacuum (the melting temperature is  $T_M = 3410^\circ\text{C}$ ). Auger analysis showed the existence of C (270 eV) and O (510 eV) Auger lines besides large W (170-180 eV) lines. While tungsten oxide ( $T_M = 1500^\circ\text{C}$ ) can be removed by flashing  $\sim 2000^\circ\text{C}$ , the tungsten carbide ( $T_M = 2870^\circ\text{C}$ ) is difficult to remove without sputtering. However, annealing the W crystal in oxygen environment oxidizes C to CO, which then can be desorbed at moderate temperatures. This process was repeated until Auger signals showed clean W only. If the crystal surface was subsequently contaminated by the residual gases, usually only a flash cleaning was needed. The Fe (or Co or Ni) was then deposited on the clean W(001) surface.

The thin films were deposited by thermal evaporation. A number of evaporators were placed in the UHV chamber, each as sketched in Fig. 22. The 0.25 mm Fe or Co wires are wrapped in the middle section of a 0.25 mm W wire. A well controlled evaporation was initiated at about  $1300^\circ\text{C}$  for Fe, as measured by pyrometer, by resistively heating the W wire. The evaporator was stable, in contrast to the resistively heating of pure Fe wires, which had a tendency to melt through. One still needs to be cautious not to alloy W with Fe whose melting temperature is much lower than W and comparable to Fe. This is accomplished by keeping the evaporation temperature a little below the melting temperature of Fe. This limitation on the temperature also limited the deposition rate for each evaporator, although multiple evaporators could be

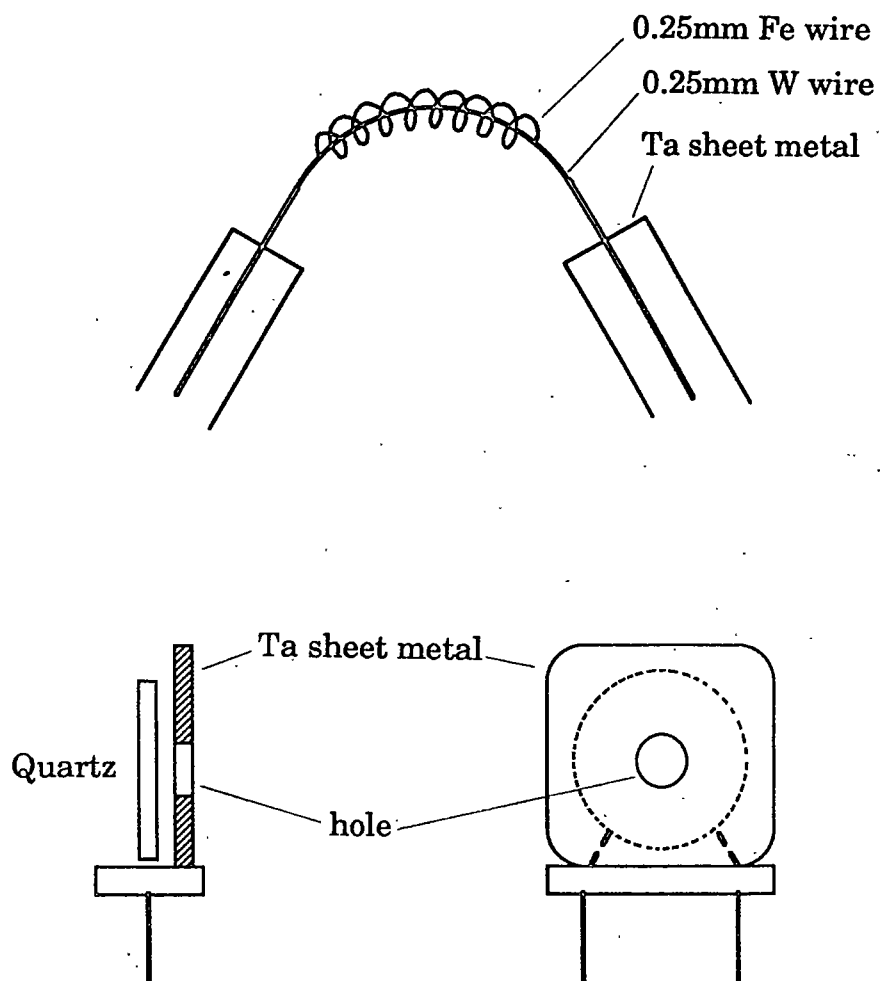


Figure 22. Evaporator (top) and QCO monitor (bottom).

used simultaneously. The rest of the chamber, especially the window of the photon detector, had to be shielded from the evaporating material.

The deposition rate was monitored by a modified quartz crystal oscillator (QCO), Fig. 22, calibrated against a standard Sloan QCO monitor. The QCO was placed adjacent to the W crystal, and measurements were taken after the frequency change due to thermal effects was stabilized. The deposition rate was about 0.01 Å/sec. During deposition, the sample was at room temperature, and chamber was kept in low  $10^{-10}$  Torr range. The newly prepared films were contamination free. The growth mode and morphology of the films was determined by LEED and Auger and will be described in detail in the subsequent chapters.

#### E. Data Acquisition

The schematic of the data flowchart of the inverse photoemission spectrometer is shown in Fig. 23. A Tektronics 4051 microcomputer was used for energy scan and data acquisition. A D/A ROM pack provided  $\pm 10$  V scan range. The Perkin-Elmer LEED control was in the circuit for the convenience of switching to the LEED mode. The IPES pulse signals were preamplified and stretched (5V by 250 ns), then fed to a counter and through a D/A converter to be plotted on an x-y plotter. Simultaneously, the signals were recorded by the microcomputer.

The sample was magnetized at the center of a 2.5 inch diameter by 2 inch length solenoid schematically shown in Fig. 20. The solenoid coil, ~600 turns of 0.5mm polyimide-coated wires, produced 100 Oe/A field, 400 Oe maximum, at the sample position. The outside surface of the coil was painted with

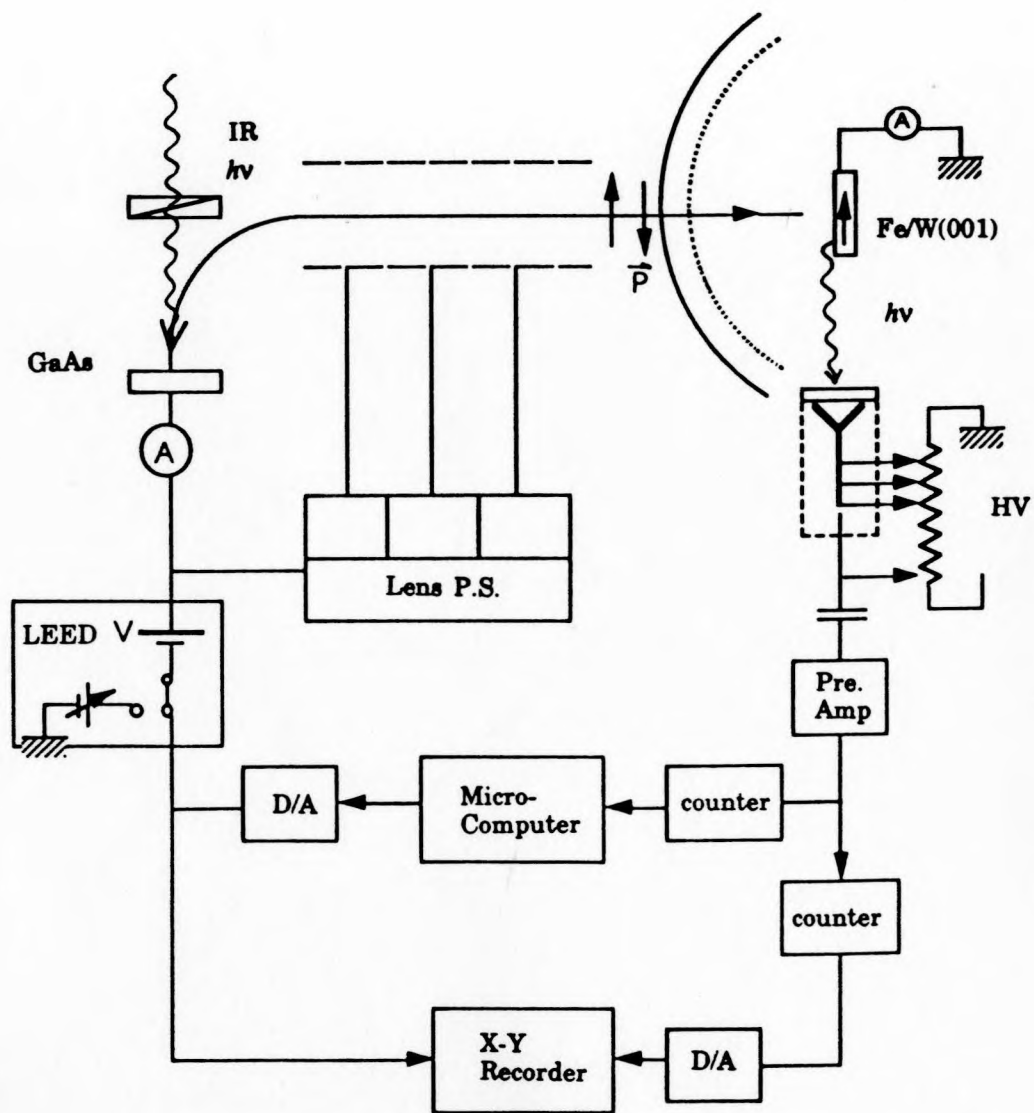


Figure 23. Schematics of SPIPES measurement.

Aquadag (a Colloidal solution of graphite) to prevent charging.

Each SPIPES spectrum consists of two IPES measurements with reversed electron spin polarizations. The thin films had to be previously magnetized and the SPIPES measurements were taken under no applied field. Reversing the sample magnetization also reverses the results of majority/minority spin spectra. The electron beam intensity was carefully kept constant, usually 4  $\mu\text{A}$  emission at the source and  $\sim 1 \mu\text{A}$  on the target at energy of middle scan.

The SPIPES spectra are ordinarily plotted as the signal strength as a function of the energy  $E$ , obtained by subtracting the photon energy from the incident energy  $E_i$ . The relationship between the energies is shown in Fig. 24, and is self explanatory. These relationships are used throughout this thesis. This way of plotting the spectra does not require further calibration or correction for the work function of the sample specimen, a feature which is particularly convenient for thin film and chemisorption systems because the work function can be variable in such systems. Additional information on the work function would be needed if the  $k$  vector parallel to the surface were to be determined for dispersion in angle-resolved measurements. A scan step of 0.2 eV was usually satisfactory. The overall experimental resolution apparently was determined by that of the photon detector.

The measured SPIPES spectrum using the partially polarized beam is a combination of polarized spectra and unpolarized spectra. It is not difficult to determine the formula to adjust for the polarization factor  $P$  ( $1 > P > 0$ ) as the following:

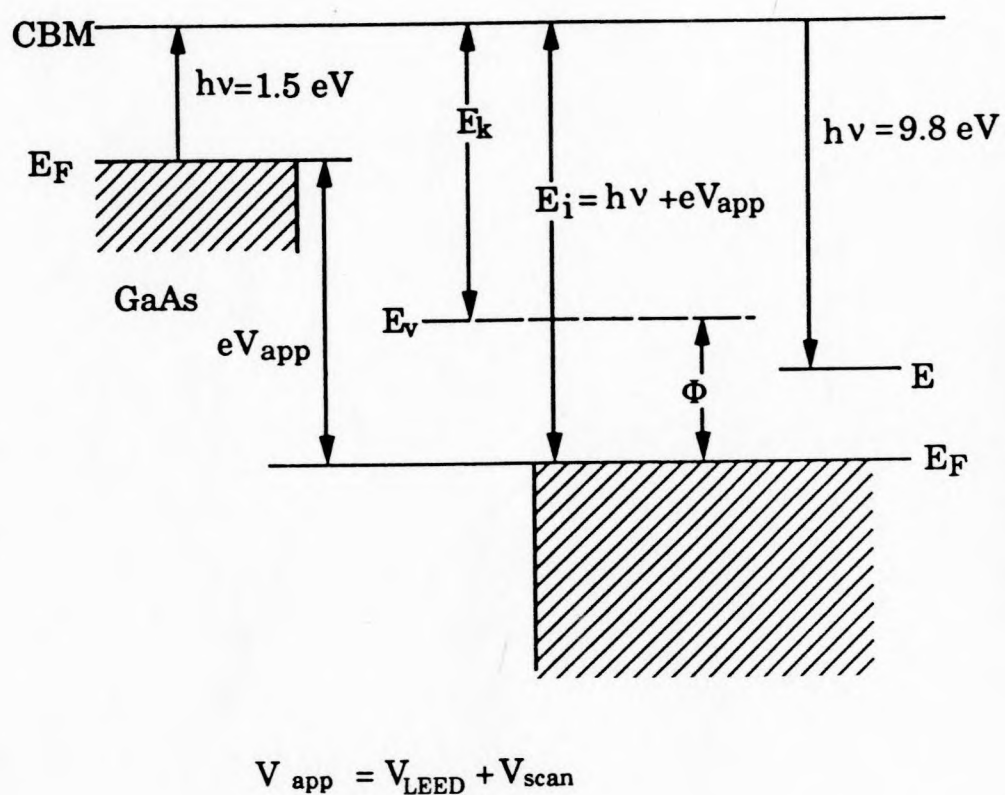


Figure 24. Energy diagram of SPIPES experiment.

$$\bar{n} = \frac{1}{2}(n\uparrow + n\downarrow) \quad (9)$$

$$A = \frac{1}{2}(n\uparrow - n\downarrow)/P/\bar{n} \quad (10)$$

$$N\uparrow = \bar{n}(1 + A) \quad (11)$$

$$N\downarrow = \bar{n}(1 - A) \quad (12)$$

where  $n\uparrow$  and  $n\downarrow$  are the measured majority and minority spin spectrum, respectively,  $\bar{n}$  is the spin-averaged spectrum,  $A$  is the spectral spin asymmetry, and  $N\uparrow$  and  $N\downarrow$  are the hypothetically 100% spin polarization SPIPES spectra, all as a function of final state energy  $E$ . Since the spin spectral asymmetry is a smaller effect based on the differences of spectral intensities of each spin, SPIPES measurements require better signal-to-noise and therefore longer time to measure. Usually, if it takes about 5 minutes to obtain a satisfactorily smooth IPES spectrum without recognizing the spin, it will take eight such scans (four accumulative scans for each spin) to obtain a satisfactory SPIPES spectrum which takes about one hour including adjusting instrument between scans of reversed spin. During the polarization adjustment using Eq. 10, the data fluctuations between a pair of spin spectra cannot be distinguished from spin polarization effect between them; the fluctuations can be unnecessarily and unphysically enhanced by the spin adjustment process. A three-point data smoothing is used on both  $n\uparrow$  and  $n\downarrow$  to reduce, if not prevent the fluctuations. The fluctuations with respect to the smoothed curve is then restored after the polarization adjustment. In other words, only systematic asymmetry is adjusted to 100% polarization and spectral difference at a single energy point is simply retained. A sample FORTRAN program is provided in Fig. 43 in Appendix A performing these data manipulations and plotting final SPIPES spectra of Fe monolayers.

## CHAPTER 4

## CLEAN W(001) RESULTS

The W(001) surface has been well studied both theoretically and experimentally in surface science. The investigations of the electronic structure of this surface include angle-resolved, and light-polarization dependent, photoemission below the Fermi level  $E_F$ ,<sup>43</sup> and above the vacuum level  $E_{vac}$ , studies using angle-resolved secondary electron emission experiments.<sup>44</sup> Between  $E_F$  and  $E_{vac}$ , IPES has been used.<sup>45</sup> In fact, W was one of the first materials considered for IPES study<sup>8</sup> since its 5d band stretches from just below  $E_F$  to just above the vacuum level.

The significance of IPES studies of clean, unreconstructed W(001) is two-fold. First, it demonstrates how the angle-resolved IPES can be an important tool to investigate the electronic band structure experimentally. Second, it provides a solid understanding of the W(001) surface, which serves as a substrate for 3-d metal magnetic overlayers studied subsequently.

The experimental setup and the sample crystal preparation are described in Chapter 3. The photoelectron source is operated with the quarterwave plate removed so the electrons are unpolarized. The incident plane coincides with W(100) mirror plane as the hatched plane shown in Fig. 25. The angle of incidence varies from  $0^\circ$  (normal incidence) to  $70^\circ$  in the incident plane. In this geometry the final state of a direct inverse photoemission transition can be determined in the surface Brillouin zone (SBZ) projected from the bcc-W Brillouin zone, as shown in Fig. 25.



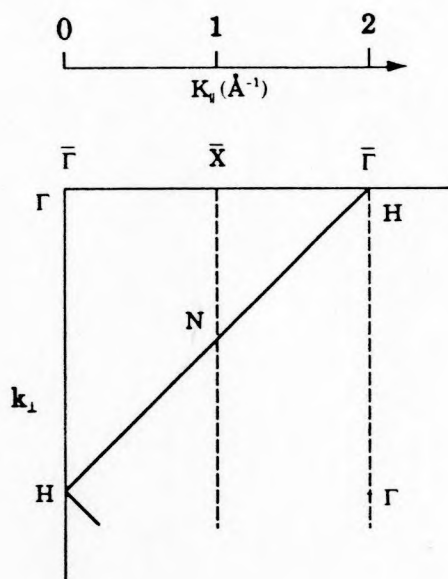
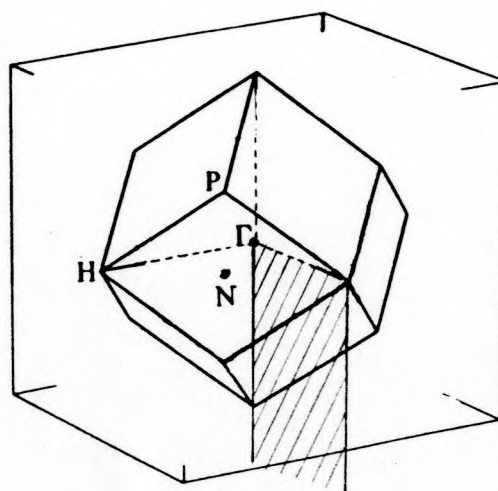


Figure 25. Tungsten bcc Brillouin zone, special points in the surface BZ, and IPES detecting plane.

The W(001) ribbon was cleaned using the standard method described in Chapter 3. The clean W surface gave good IPES spectra, but when Auger analysis showed C or O contamination, the IPES spectra became basically structureless and the intensities were lower. The cleaning procedures were repeated many times until the surface was free of contamination and the IPES spectra showed satisfactory prominent peaks at off-normal angles such as shown later in Fig. 27.

The LEED  $p(1\times 1)$  pattern was easily observed, indicating an unreconstructed surface atomic net. Shown in Fig. 26 is a photograph of LEED pattern from the  $p(1\times 1)$  surface.

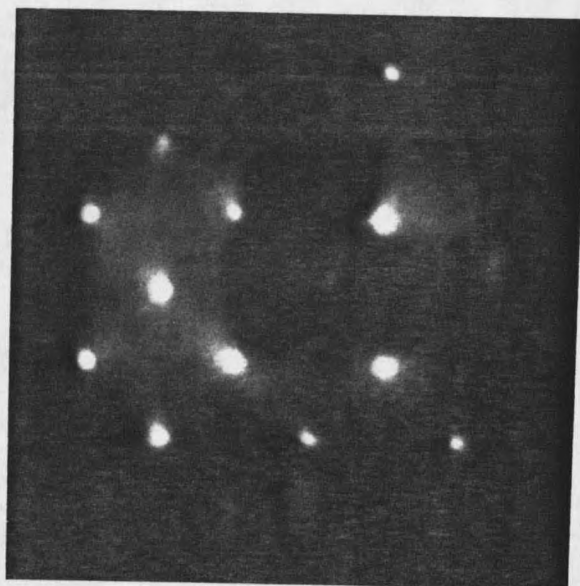


Figure 26. LEED pattern of  $p(1\times 1)$  W(001).

The IPES spectra are plotted in terms of the final state energy with the use of the energy conservation law,  $E = E_{\text{electron}} - h\nu_0$ . Two versions of bandpass UV photon detector were used, one with a maximum sensitivity at  $h\nu_0 = 9.8$  eV using the  $\text{CaF}_2$  window and the other with a maximum sensitivity at  $h\nu_0 = 9.5$  eV using the  $\text{SrF}_2$  window (Chapter 3). The dispersions of the peaks with incidence angle show very consistent trends between the two measurements, confirming the identification of the final states.

Figure 27 shows angle-resolved inverse photoemission (ARIPES) spectra from W(001) along the  $\bar{\Delta}$  plane, taken with the  $\text{SrF}_2$  window. There are two dominant features. One observed at angles  $\theta \geq 25^\circ$  disperses over the  $E = 3\sim 4$  eV region and is assigned to a bulk band transition because it is not sensitive to a large amount of chemisorbed oxygen. The other in the  $E = 1\sim 2$  eV region starts from  $\theta \geq 15^\circ$ , and may consist of two peaks splitting at  $25^\circ$  to  $30^\circ$ . This feature was largely suppressed by oxygen absorption. The normal-incidence curve is difficult to measure, partly because of the smaller signal-to-noise ratio due to the grazing detecting angle (see the geometry in Fig. 20). Nevertheless it is in good agreement with a similar work cited in Ref. 45.

Although angle-resolved IPES (ARIPES) measures the momentum vector of the incident electron, when the electron crosses the crystal-vacuum interface, only the component of the wave vector parallel to the surface,  $k_{\parallel}$ , is strictly conserved, while the normal component,  $k_{\perp}$ , in general bears no simple relation to the external normal momentum. The kinetic energy,  $E_K = E_{\text{electron}} - E_{\text{vac}}$ , is equal to the initial energy (w.r.t.  $E_F$ ) minus the target work function,  $\phi_W = 4.6$  eV. Therefore one can plot the band dispersions along  $k_{\parallel} = (\sqrt{2mE_K}/\hbar)\sin\theta$  to determine the possible transitions along  $k_{\perp}$  vertical lines; see the hatched plane of the irreducible Brillouin zone as shown in Fig. 25.

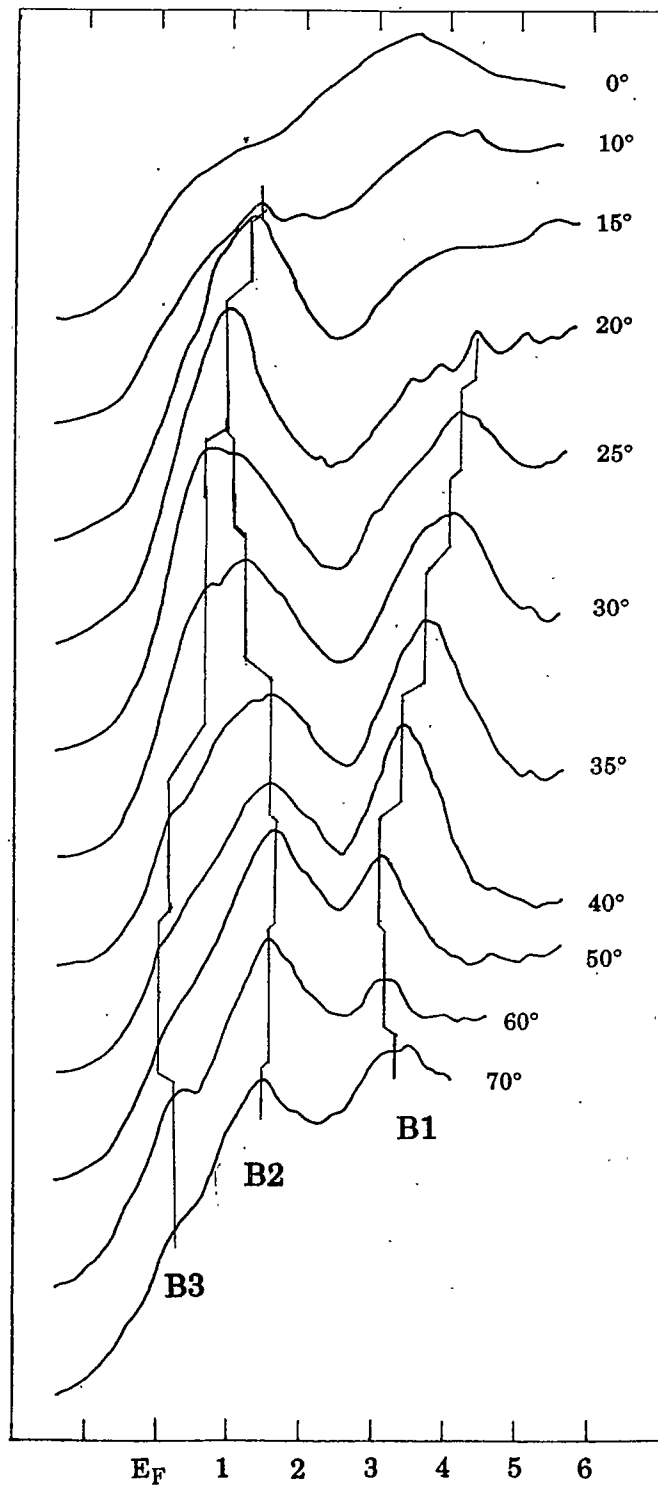


Figure 27. W(001) ARPES spectra with SrF<sub>2</sub> window photon detector.

Such a dispersion plot is shown in Fig. 28. It is plotted as  $E_f$  vs.  $k_{||}$  along the  $\bar{\Delta}$  line and it combines measurements with  $\text{SrF}_2$  and  $\text{CaF}_2$ . The peaks are denoted by large points, the shoulders by small dots, and three major bands, from B1 to B3, are indicated.

Figure 29 shows the non-relativistic band dispersions parallel to  $k_{\perp}$  lines for fixed  $k_{||}$  points. One is at the  $\bar{\Gamma}$  point<sup>1</sup> for  $k_{||}=(0,0)$  and another at the  $\bar{X}$  point<sup>2</sup> for  $k_{||}=(0,1)=1.0 \text{ \AA}^{-1}$ . At the  $\bar{\Gamma}$  point B1 is at  $\sim 3.5\text{eV}$ ; and at  $\bar{X}$  point B1 is at  $\sim 3.3\text{eV}$  and B2 at  $1.8\text{eV}$ , and, allowing a few tenths of eV broadening, they can all be attributed to the direct interband transitions as marked by vertical lines.

Indirect transitions may be responsible for some features in the spectra since there are plenty of final states available, as shown in the band calculations. However, both B2 and B3 are strongly suppressed by oxygen chemisorption for reasons we do not presently understand. Further, surface-derived features should be symmetric about the SBZ boundary, which is different from the bulk BZ boundary. B2 and B3 band dispersions are roughly symmetric around  $\bar{X}$ , while B1 dispersion is not. Therefore, B2 and B3 may be related to surface-derived features. In fact, in Ref. 46, it has been found from slab calculations that the  $(1\times 1)\text{W}(001)$  surface states exist near the  $\bar{X}$  point at  $\sim 0.2\text{-}0.3 \text{ eV}$ , a result which strongly suggests that the B3 band is a surface state, at least near the  $\bar{X}$  point.

The IPES results from the  $\text{W}(001)$  sample demonstrate that the bulk electron band structure is well reproduced in the IPES spectra. It is particularly encouraging that pronounced peaks with drastic dispersions are sometimes observed which can be attributed to direct interband transitions, because it means that the IPES technique can be applied to  $k$ -resolved electron

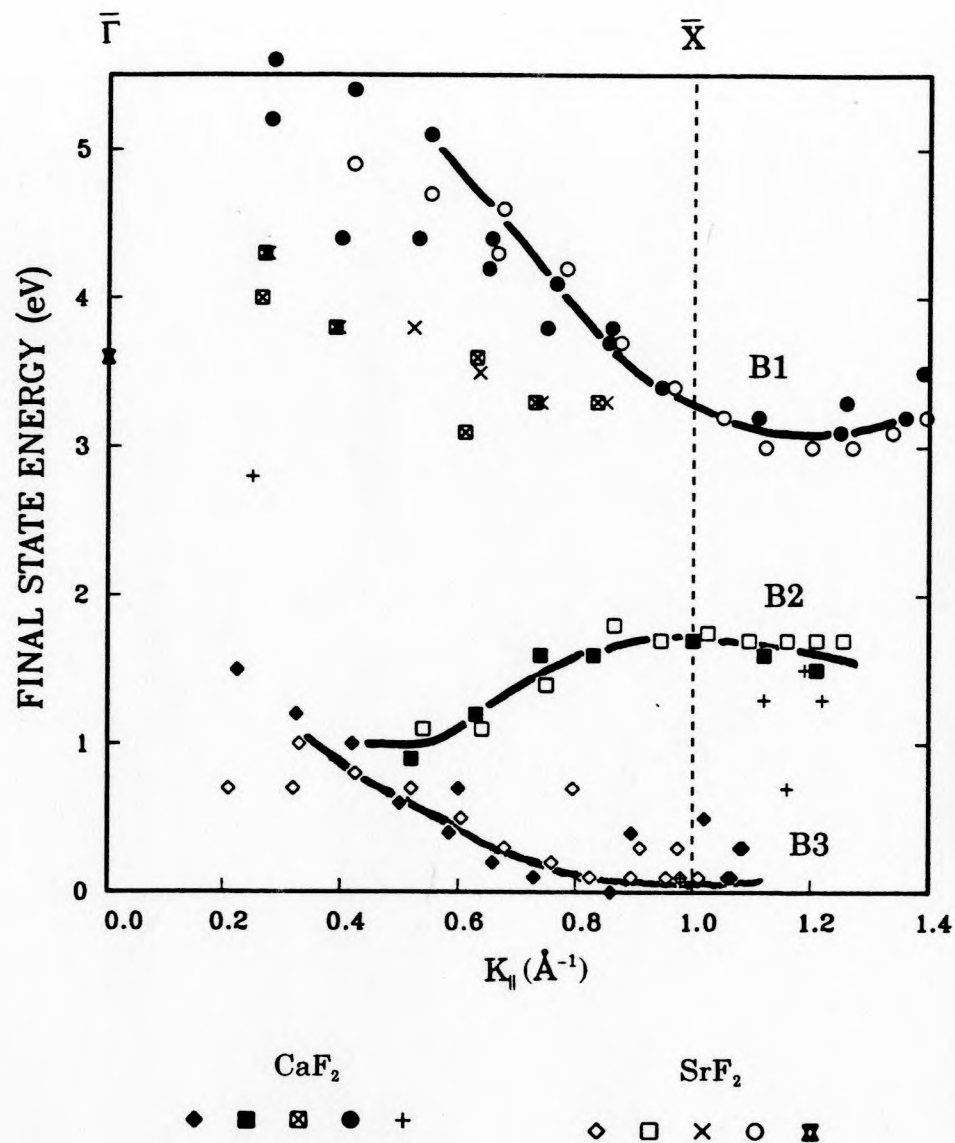


Figure 28, Band dispersion along  $\bar{\Delta}$ , the solid symbols are from CaF<sub>2</sub>-photon detector and the open symbols are from SrF<sub>2</sub>-photon detector, as listed on the bottom. Three lines highlight the bands B1, B2 and B3, corresponding to the pronounced peaks in the spectra. Other symbols represent small features.

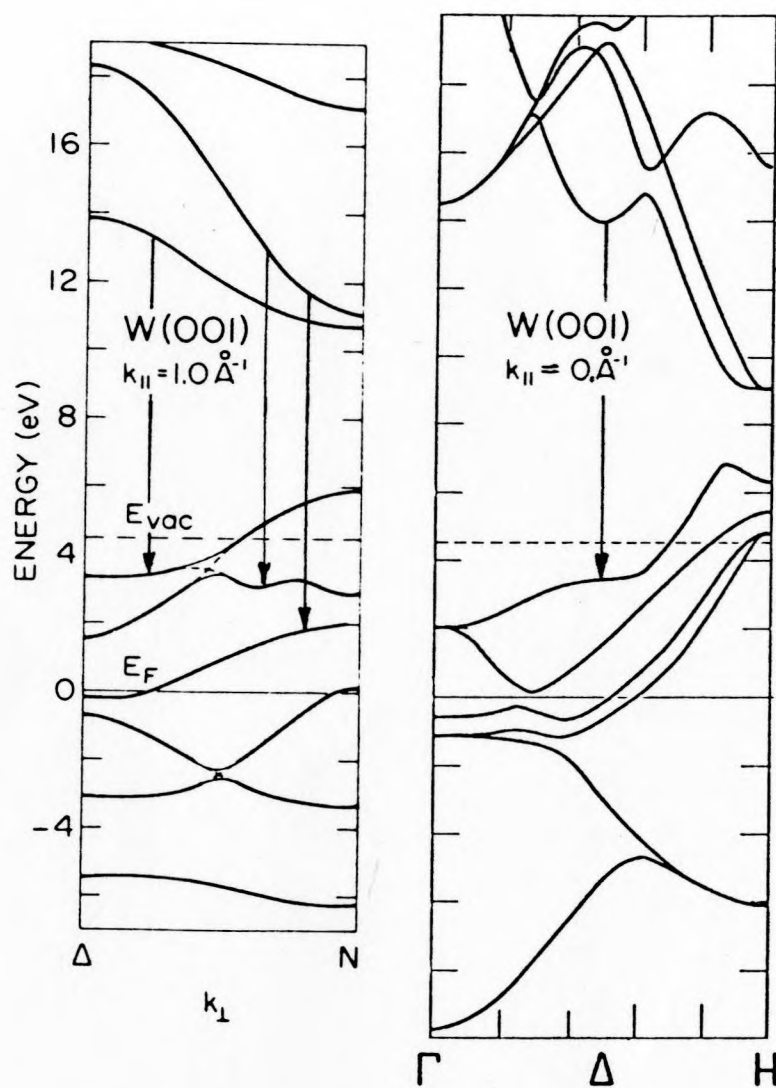


Figure 29. Theoretical W band calculations,<sup>44</sup> adapted from Ref. 43. Left:  $k_1$  from the middle of the  $\Gamma$ - $\Delta$ - $H$  line to  $N$ , cf. Fig. 25. Right:  $k_1$  from  $\Gamma$  to  $H$ . The vertical lines indicate the possible direct transitions at  $\sim 9.8$  eV photon energy, cf. Fig. 28.

band structure investigations in any metallic or semiconducting material. The good agreement between our IPES spectra and theoretical band structure gives us confidence in later analysis of electronic structures in magnetic overlayers.



## CHAPTER 5

## Fe ON W(001)

The properties of ultrathin Fe films were studied. First, film growth properties were determined. Then magnetic and electronic properties were investigated by spin- and angle- resolved inverse photoemission for film thicknesses of a single-monolayer to thicker films which are essentially "bulklike". In the bulklike samples, bulk band states were identified, and agreement with bulk Fe(001) properties was found. Films thinner than bulklike ones showed a "collapsing" band behavior, a behavior related to the vanishing of the exchange splitting in the Stoner picture. The latter result suggests that the Curie temperature is smaller for monolayer films. Further, the results provided data for evaluating the spatial correlation of the spin-density fluctuations in the itinerant ferromagnetic picture. The results tend to disfavor the local-band picture at finite temperatures.

A. Thin Film Characterization

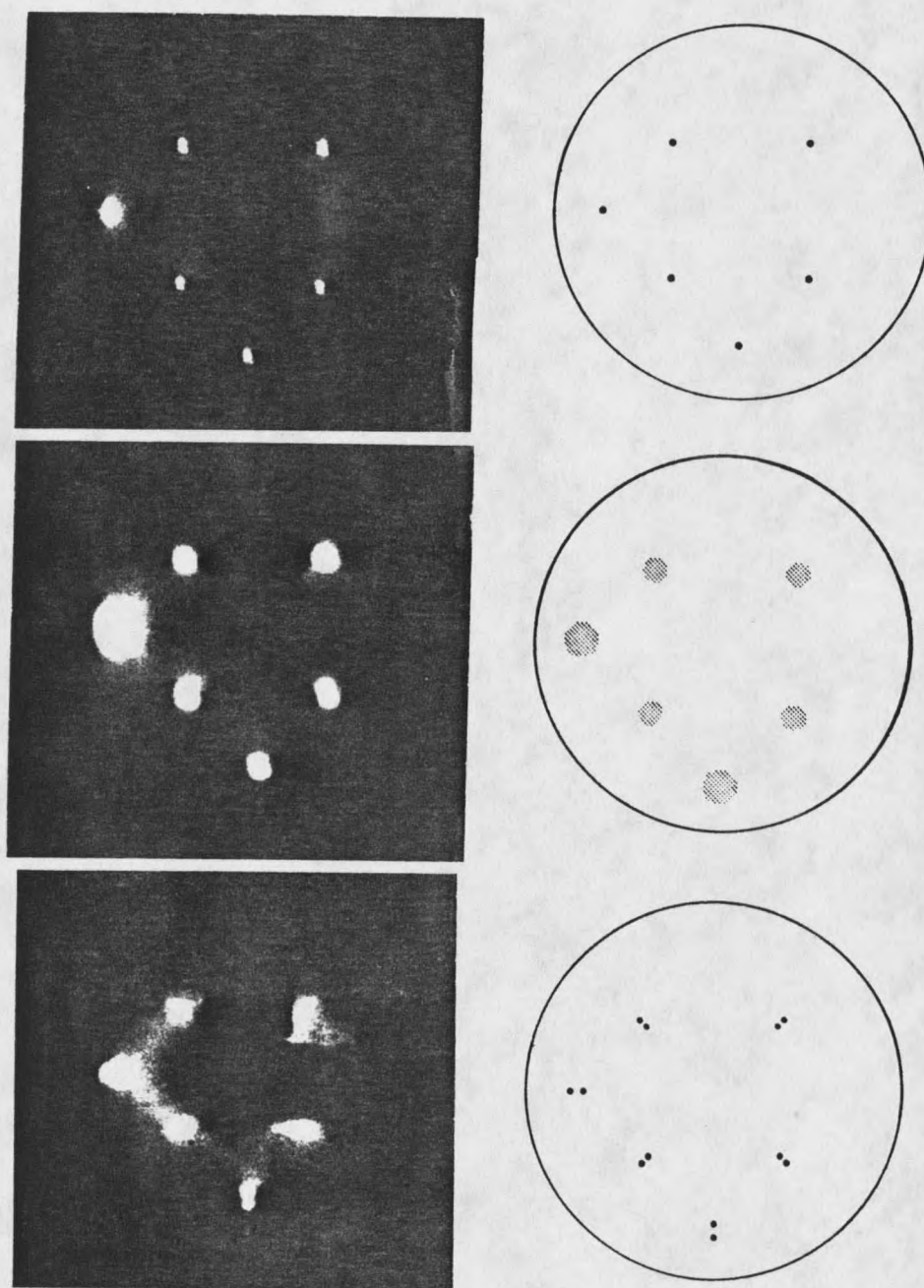
The growth properties of ultrathin Fe overlayers on W(001) were characterized by LEED and AES. The films were made by thermal deposition of Fe atoms onto a clean W(001) surface. The Fe films were found to grow layer by layer epitaxially while maintaining the square surface net. The thickness of the monolayer-scale films was determined by Auger measurements.

The Fe was deposited on a clean W(001) ribbon from an evaporator made by wrapping Fe wire on a W wire core (cf. Chapter 3). Just before deposition the W crystal was heated to remove C and O contaminations and checked by Auger analysis. After cleaning, the IPES showed good W spectra as described in the preceding chapter. The crystal was close to room temperature during Fe deposition, being heated only by the exposure to the thermal radiation from the evaporators. Any excessive heating was avoided because the ultrathin films were not stable at a few hundred degree centigrade. Heated films showed a decrease of the Fe adlayer Auger signal and an increase of the substrate W signal.

The LEED patterns of the Fe overlayer were basically  $p(1 \times 1)$  as shown in Fig. 30. A single monolayer of Fe is pseudomorphic: the sharp  $p(1 \times 1)$  LEED pattern indicates that the Fe atoms arrange themselves with the same lattice structure as the W substrate. Coverage above a monolayer still had a  $p(1 \times 1)$  pattern but the LEED spots were blurred. The blurring is the result of crystalline imperfection resulting from the pseudomorphic film releasing its stress to attain the bulk lattice space, which is 10% smaller than that of W.

Table 2. Bulk material properties of W, Fe, Co and Ni

	Crystal Structure	Lattice Constants(Å)	Melting Temp $T_{\text{Melting}}(^{\circ}\text{C})$	$E_{\text{Cohesive}}$ <sup>[Ref. 18]</sup> (kcal/mol)
W	bcc	3.16	3410	200.
Fe	bcc	2.87	1536	98.9
Co	hcp	2.51/4.07	1459	101.2
Ni	fcc	3.52	1453	102.3



84

Figure 30. LEED patterns observed of Fe on W(001). The top photograph is for one monolayer of as-deposited Fe which looks identical to that of the clean W(001), while the middle is for more than one monolayer of as-deposited Fe and the bottom is that after slightly heating the sample. The drawings to the right of each photograph identify sharp/blurred spots by solid/shadow circles.

In an attempt to restructure the thin film by slightly heating the sample, two smaller spots belonging to two different sets of square LEED patterns emerged from each blurred large spot. These two spots were separated in the radial direction by 10% of the radial distance from the (00) central spot. The pattern indicates that the bcc Fe and bcc W structures were observed simultaneously (Fig. 30). At the same time, the Fe Auger signal decreased and the W Auger signal increased. It seems that Fe formed islands on the surface with the bulk Fe lattice constant which are in perfect alignment with the substrate lattice to give the sharp doubled LEED pattern as shown in the bottom of Fig. 30. It is easy to see that the as-deposited Fe overlayers must have a strong tendency to release strains from the first (pseudomorphic) layer so the intrinsic lattice spacing is attained. The relaxation of the ~10% lattice mismatch in Fe multilayers can create a large number of defects, which can be responsible for the blurred LEED spots.

It has been determined that this overlayer system grows layer-by-layer, by the Frank-van der Merwe (FM) mode.<sup>47</sup> The cohesive energy, i.e., the energy it takes to free an atom from being in the solid state, is much higher for tungsten than for the 3d metals Fe, Co, Ni; see Table 2. Growth kinetics analysis indicates that layer-by-layer growth is favored when elements of lower surface energies are deposited on substrate with higher surface energy, while the reverse situation favors three-dimensional (3D) island formation.<sup>47</sup> Therefore Fe, and also Co and Ni, can be expected to grow layer by layer on tungsten, at least for the first few layers. A more detailed investigation of Fe(110) overlayer growth on W(110) surface has been conducted by Gradmann et al.<sup>48</sup>; those results are consistent with our observation of Fe(001)/W(001) epitaxial growth.

In these studies, layer-by-layer growth was inferred from two facts: First, by a few monolayers the W Auger peak amplitudes decreased rapidly to a value below the noise level while the overlayer crystalline structure exhibited an unchanged LEED pattern during growth (Fig. 31). Such behavior is inconsistent with other growth modes, either 3D islands (vertical columns) on the W substrate or islands after one monolayer of Fe, since the substrate is not uniformly covered in these cases.

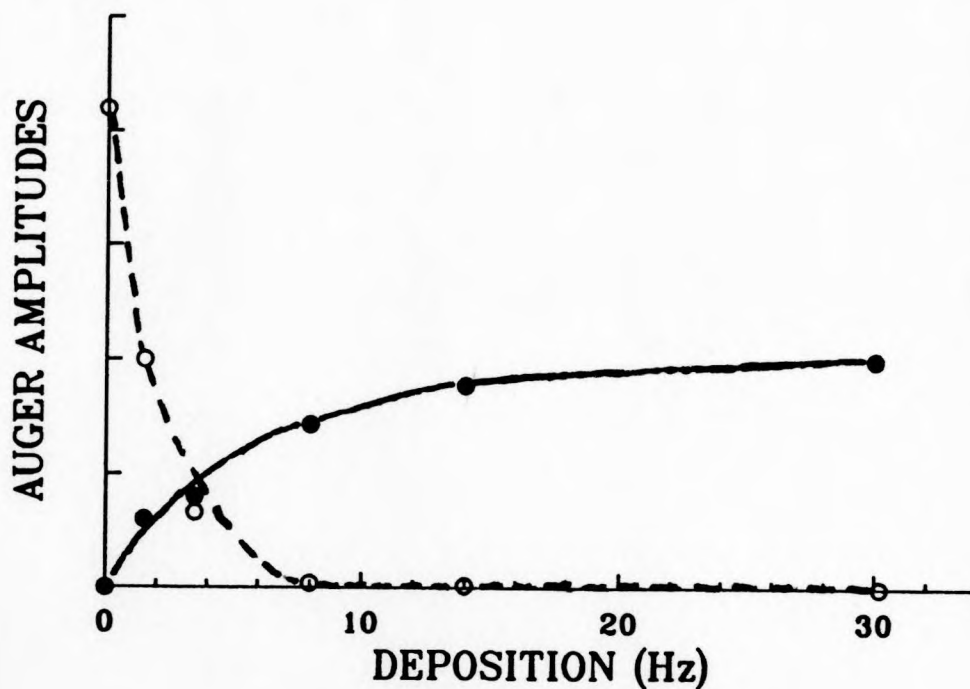


Figure 31. Auger peak-to-peak amplitudes of the W(001) substrate (169 eV and 179 eV) and of the Fe film (598 eV, 651 eV and 703 eV), as a function of the QCO frequency change which is linearly proportional to the Fe deposition.

The second observation which tends to confirm layer-by-layer growth is the detailed coverage dependence of the Auger signals during Fe deposition. Shown in Fig. 32 is one set of measurements containing about 40 points. The horizontal axis is the total Fe deposition measured by the frequency change of the QCO, in Hz. The Auger amplitude on the vertical axis is the sum of the three Auger amplitudes for the Fe triplet between 600-700 eV. The latter is normalized to the sum of the Fe and W signals to eliminate or reduce the effect of any instabilities in the measurements of the experimental system. Using a least-squares fitting method (LSF), it was found that the experimental curve can be fit by straight-line segments. Each line segment has an equal projection on the abscissa and each corresponds to approximately an incremental coverage of one monolayer. This result is found because lateral growth in one layer will be accompanied by a linear signal increase with a different slope for each layer. In this case, the curve can be fitted by a sequence of straight lines joined by kinks.<sup>49</sup>

This argument implies that the substrate W signal should decrease in straight line segments, but actually the decrease turns out to be more nearly exponential except at the beginning where the attenuation is very rapid. The reason for this behavior is not presently known.

The quality of the adlayer films was quite satisfactory, as the LEED and Auger results demonstrate. The Auger results excluded the possibility of W migrating to the surface of the Fe or significant Fe-W alloying. Even though W and Fe both have non-zero mutual solubilities<sup>50</sup>, no mutual dissolution was detected by the surface-sensitive Auger analysis, either from a well prepared Fe adlayer or from the clean W after removing the Fe adlayer. The Fe was removed by flashing the W ribbon to a very high temperature about 2200°C.

## AUGER GROWTH ANALYSIS, Fe/W(001)

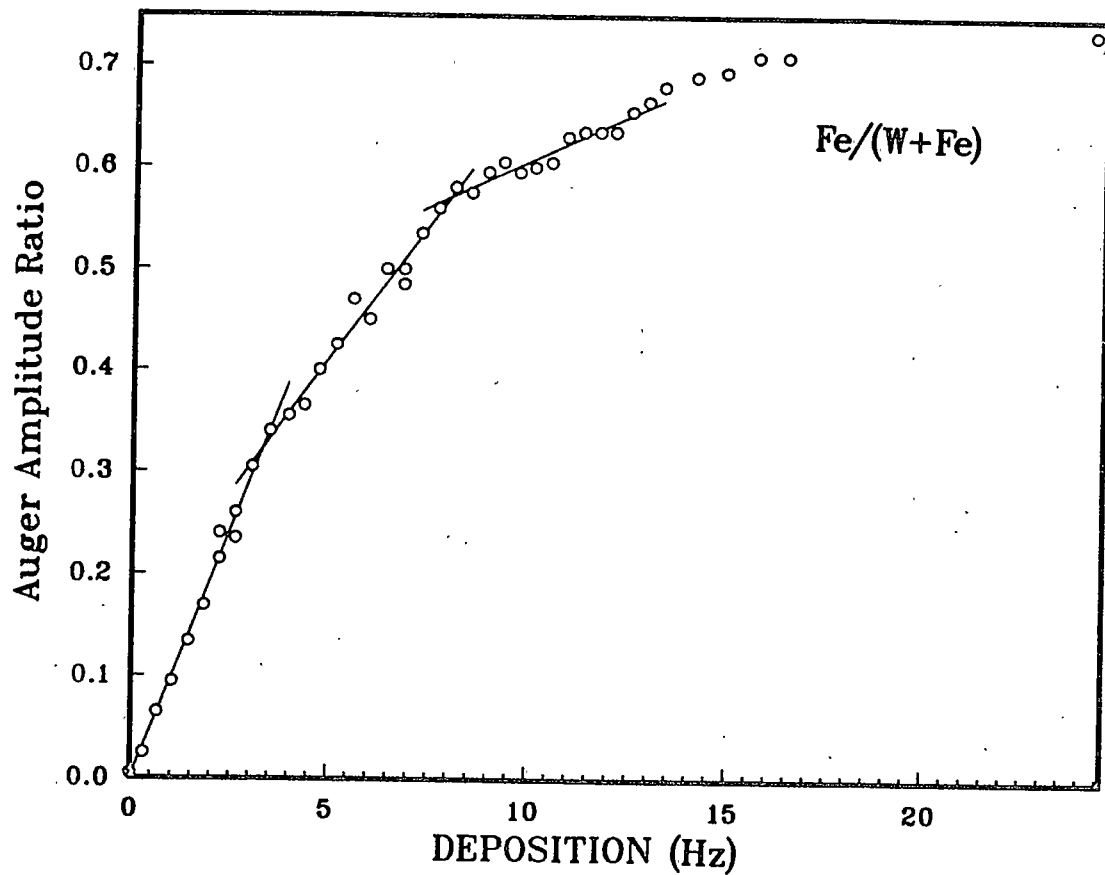


Figure 32. LSF-fitted Auger amplitude ratio measurements. The amplitude ratio is obtained by the Fe signal amplitude normalized to the sum of the Fe and W signals.

The determination of the completion of each monolayer by Auger spectroscopy agreed fairly well with that inferred from the QCO data. The first Fe monolayer is completed with less deposition than the following layers, as shown in Fig. 32, which is consistent with the pseudomorphic layer being ~20% less in atomic density relative to the bulk Fe. The relative Auger amplitudes were thus used to calibrate the Fe coverage in units of monolayers. For the first monolayer of Fe the ratio of the Fe peak height to the total peak heights of the Fe and W signals was about 55%.<sup>51</sup>

#### B. Normal-Incident SPIPES from Ultrathin Magnetic Films of Fe

The magnetic and electronic properties of Fe thin films were examined by SPIPES. The Fe was found to be ferromagnetic starting from the first monolayer. Since our spin sensitivity is in-plane, the ordering is in-plane. Spin-dependent intensity peaks in the spectra are attributed to Stoner band-structure features.

The as-deposited Fe thin films, prepared and calibrated as described above, were moved from the preparation position to the magnetization or to the SPIPES measurement positions. They were magnetized parallel to the  $\bar{\Sigma}$  direction of the SBZ and only the remanent magnetization was measured. The electron beam was incident normal to the sample surface, and the spectra were measured for incident spin polarization parallel to both the magnetization (spin up,  $\uparrow$ ) and its reverse (spin down,  $\downarrow$ ). The polar angle was taken  $\theta=0^\circ$  to be at the surface normal. The spectra shown have been corrected for spin impurity of the electron beam as described in Chapter 3.

Figure 33 shows the spectra obtained for one to four monolayers of Fe on



the W(001) surface. The spin  $\downarrow$  data points are denoted by downward triangles ( $\nabla$ ), and the spin  $\uparrow$  points are denoted by upward triangles ( $\Delta$ ). For comparison the figure also shows the spectral asymmetry  $A(E)$ , i.e., the spin spectral difference normalized by the sum as defined by Eq. 10 in Chapter 3.

The spectra are generally dominated by the minority-spin (spin  $\downarrow$ ) signal, and the maximum asymmetry for Fe is observed near 1.5 eV. The asymmetry amplitude varies linearly with the Fe film thickness. The latter result indicates the films were ferromagnetic from the first monolayer of Fe. The result excludes the possibility of a "magnetic dead layer".

The SPIPES results indicate that the direction of remanent magnetization is in the film plane, because in the experimental geometry the spin quantization axis was kept orthogonal to the thin film surface normal, i.e., in the plane. Analysis of thin film anisotropy shows that the anisotropy energy can be expanded as

$$E_{\text{anisotropy}} = K^{(2)}_z \alpha_z^2 + K^{(4)}_{xy} \alpha_x^2 \alpha_y^2 + K^{(4)}_z \alpha_z^4 + O(\alpha^6) \quad (13)$$

where the  $\alpha$ 's are the direction cosines of the magnetization vector, the z-axis is along film normal and the x,y axes are parallel to the mirror planes, ( $\bar{\Delta}$  directions), and the  $K^{(n)}$ 's are the coefficients in the expansion to the n-th order (Appendix B). The leading term of  $K^{(2)}$  describes the easy axes of magnetization which can lie either perpendicular to the film plane (if  $K^{(2)}_z < 0$ ) or in the film plane (if  $K^{(2)}_z > 0$ ). The shape anisotropy energy of thin films also favors in-plane magnetization because of the existence of a demagnetization field. If the total anisotropy (anisotropy density, to be precise) favored perpendicular magnetization, the SPIPES spectra would have shown no spin-

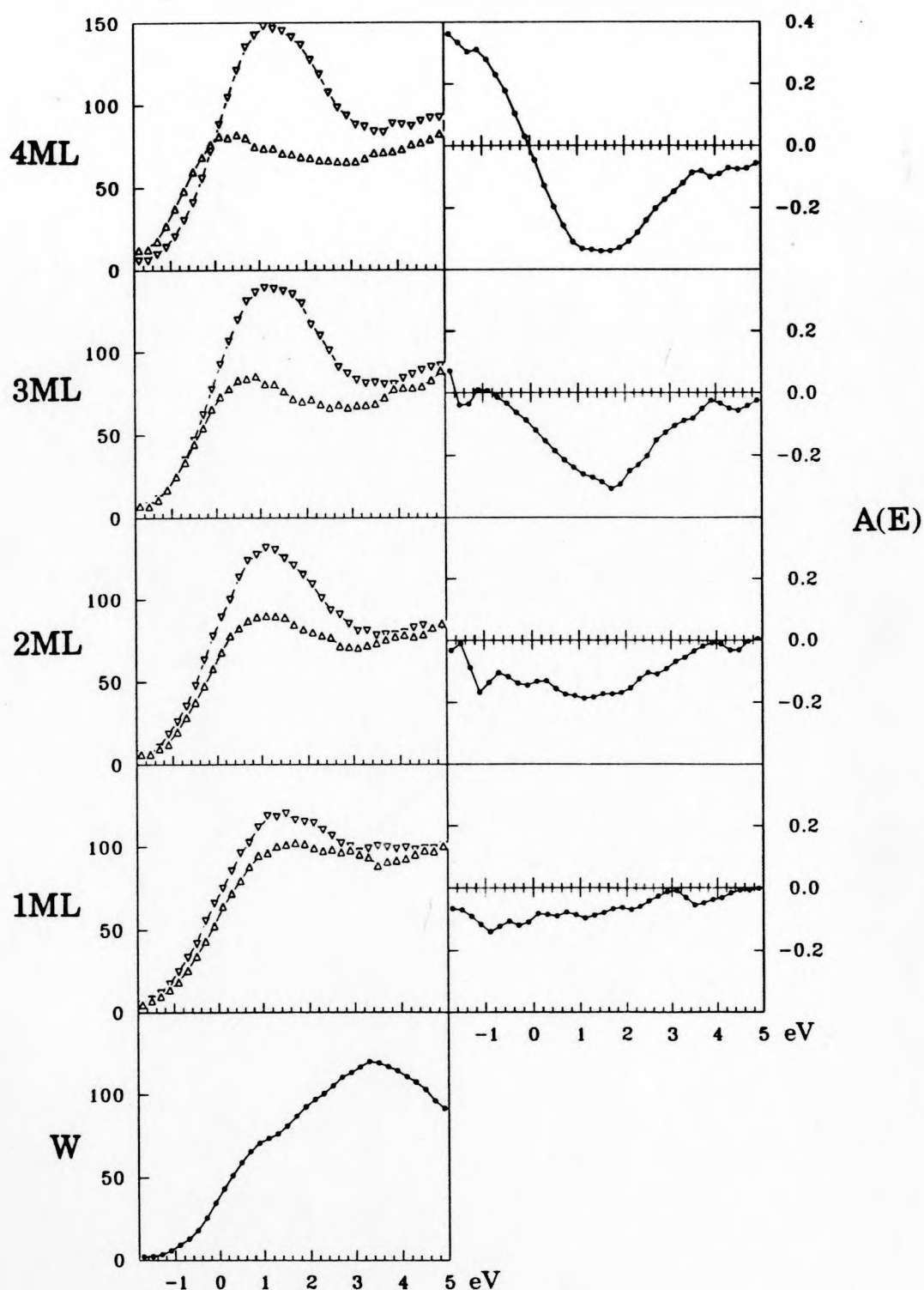


Figure 33. SPIPES and spectral asymmetry of Fe thin films, the minority spin data are denoted by  $\nabla$ , and the majority spin points are denoted by  $\Delta$ .

dependence for the present geometry. The next non-vanishing terms in the thin film anisotropy, the  $K^{(4)}$ s, indicate that the in-plane remanent magnetization of the Fe thin films may lie in the  $\bar{\Sigma}$  axes or the  $\bar{\Delta}$  axes, depending on the sign of  $K^{(4)}_{xy}$ . It is not clear in the present case which axis, if any, is preferred. Measurements with either axis rotated to coincide with the spin quantization axis were not possible in our experimental setup. However, the SPIPES results have revealed a spin-dependent electronic band structure which at large thickness agrees fairly well with the results of similar measurements for bulk Fe(001) surface along the  $\bar{\Sigma}$  direction.<sup>52</sup>

The proportional increase of spectral asymmetry  $A$  with film thickness implies that the Fe overlayers were within the analysis depth of SPIPES, which is about 10 Å. The spin-dependent spectral peaks and shoulders also evolved as a function of film thickness. With the present experimental resolution, no significant changes were observed for spectra thicker than four monolayers of Fe. Therefore four or more atomic layers of Fe are referred to as "bulklike". The spectra for thinner films are a superposition of the signal from the Fe film, the W substrate and their interfaces.

The bulklike Fe spectra are shown in the top panels of Fig. 33. The minority spin spectrum shows a large peak at ~1.3 eV, and the majority spectrum also has a peak about 0.2 eV above the Fermi level  $E_F$ . At  $E_F$ , the majority intensity exceeds the dominant minority intensity as the cross-hatched area shows in Fig. 33, a characteristic of the Fe electronic structure, as described in Fig. 5. The secondary contribution can be seen at the higher-energy end of the spectra. The secondary intensity can be extrapolated down to the low energy cutoff. It is interesting to notice that the inelastic processes have a large degree of spin orientation ( $A(E) < 0$  at the higher energies) due to

the spin population of the lower-energy final states.

It is natural to compare these results with the bulk electronic properties. Possible direct and indirect transitions are identified to help interpret the results. Figure 34 shows the bulk Fe bands along the  $\Gamma$ - $\Delta$ -H line, corresponding to the Fe(001) surface normal.<sup>53</sup> The dashed and solid curves are the minority and majority spin bands, respectively. Consider the allowed direct transitions at 9.8 eV photon energy. As the vertical arrows indicate, the majority-spin final states lie just above  $E_F$ , and the minority-spin final states at about 1.5 eV. Both direct transitions are possible contributors to the features in the spectra. The  $\Delta_2^{\uparrow\downarrow}$  bands which merge at  $H_{26}^{\uparrow\downarrow}$  have dipole-forbidden transitions to  $\Delta_6^{\uparrow\downarrow}$ .

The indirect transitions tend to reflect the DOS (Chapter 2). The calculated bulk DOS<sup>54</sup> are shown in the lower panel of Fig. 34. The minority spin states exhibit a pronounced d-band peak at about 1.5 eV. It originates from the d-bands in the neighborhood of  $\Gamma'_{12}$  in the band diagram. It is obvious that only indirect transitions, not direct, play an important role at that k point because there is no initial state 9.8 eV directly above it. Similarly, it may be that the peak intensity at  $E_F$  in the majority spin spectra may partially reflect the peak in the majority spin DOS from indirect transitions.

The main features of the bulklike spectra exhibit great similarities to the spectra from bulk Fe(001), as measured by similar methods<sup>52</sup> which used a different photon detector and electron spin polarization geometry.<sup>52</sup> The majority and minority spin peaks are at essentially the same energies. This similarity is strong evidence that epitaxially grown Fe thin films eventually develop into the bcc Fe(001) structure.

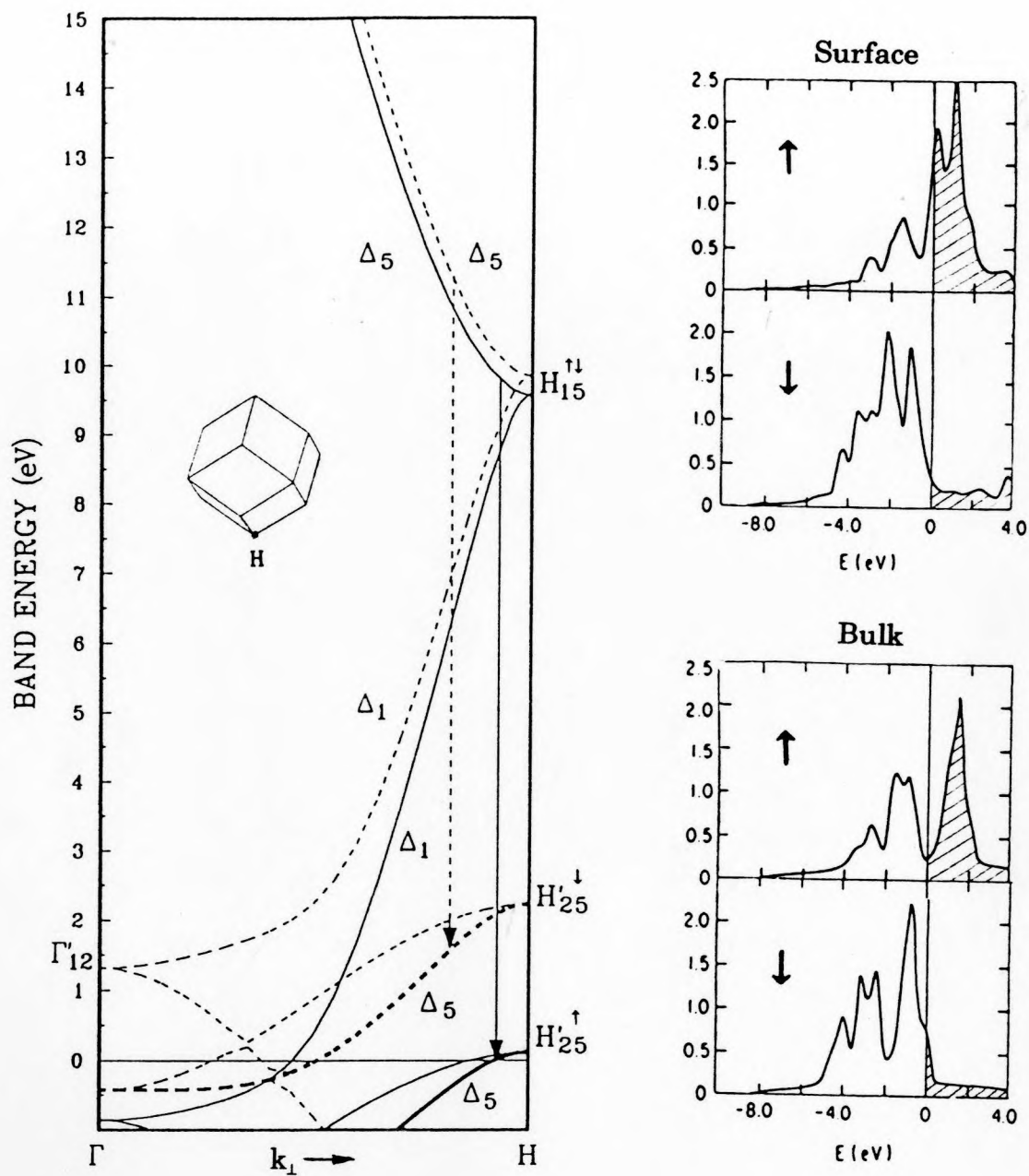


Figure 34. Left: bulk Fe bands along Fe(001) direction. Right: bulk and surface layer-projected density of states. Adapted from Refs. 53, 54.

The spectra for the bulk Fe(001) surface were measured by Kirschner et al.<sup>52</sup> with a bandpass photon detector of the same maximum response photon energy but reportedly having better energy resolution; therefore their spectra may differ from ours in details. It should be noted that the intensity of the majority spin peak relative to the minority peak for the bulklike thin films were significantly (~50%) lower than that for bulk Fe(001). This difference may be due to one or more of the following factors: the instrumental resolution, the inelastic contribution, and the magnetization of the thin films. The instrumental resolution directly affects the range of initial and final states integrated into each spectral point. The inelastically scattered electrons may contribute more to the high energy minority peak than to the majority peak at  $E_F$ . This effect could be more pronounced for a deposited thin film with larger numbers of defects and dislocations, that could contribute to a greater degree to inelastic scattering than a single crystal would. If, however, this intensity difference is an intrinsic property of thin film magnetism, it could mean that the thin film magnetization is enhanced over that of the bulk material. That is, smaller unoccupied majority DOS and larger unoccupied minority DOS implies more majority electrons and fewer minority electrons.

If the enhanced magnetism observed in the thin films is indeed intrinsic to the films, or related to the dilated Fe lattice in the overlayer, then SPIPES and SP-PES may be combined to provide further information about the electronic structure changes due to geometric changes. The dilation is a result of the lattice mismatch between the W and the Fe (see discussions in Chapter 2B). For example, the three-fold degeneracy of the states at  $H_{25}^{\uparrow}$  in the bulk might be removed as a result of reduced symmetry in the 2D layer, and part of the split-off bands could fall below  $E_F$ ; or the dilated lattice of the strained film

would narrow the d-bands which can result in the  $H_{26}^{\uparrow}$  states at the top of the majority d band being lower in energy.

As an extension to this reasoning, we would expect the reduced film thickness to cause a further signal reduction in the majority spectra at  $E_F$  as a result of increased Fe surface-to-volume ratio and a larger lattice dilation. Figure 33 shows for smaller film thickness that the majority spectral intensity at  $E_F$  is smaller and becomes smaller than the minority intensity for one monolayer. This effect is consistent with the previous argument that the majority/minority intensity ratio is lower in the thin films than in bulk Fe.

As a matter of fact, the changes noted above have been inferred in the surface layer electronic structure calculation.<sup>54</sup> The resultant layer-projected DOS are shown in Fig. 34. The surface-layer  $d\uparrow$ -bands fall completely below  $E_F$ , and the minority spin density is larger than the majority at all energies above  $E_F$ . It should be borne in mind that the layer-projected DOS includes all  $k_{\parallel}$  in the irreducible SBZ, and therefore is related more to indirect transitions in general. Nevertheless, when the film thickness is in the range of a monolayer, the surface-layer contribution is more important, since the bulk contribution is reduced, resulting in the reduced majority intensity at  $E_F$ .

### C. Off-Normal-Incidence SPIPES

Off-normal angle-dependent IPES is often used to check electron band dispersions. In the present case, a flat dispersion was found in bulklike Fe, along the  $\bar{\Sigma}$  direction.

The bulklike Fe thin film SPIPES spectra for incidence angles of 0 to 70°

are shown in Fig. 35. The main feature is the dominant minority spin intensity, peaked at  $\sim 1.5$  eV, which indicates the magnetic order in the thin film just as the normal-incidence spectra do. Little if any dispersion of this Fe feature is found in the spectra. When the incidence angle increases the spectral intensities of each spin at high energy rise drastically with respect to the intensities at low energy, obscuring any feature that might be present. For all angles of incidence, a rather large minority spin contribution persists over that range where mainly inelastic secondary signals are expected to contribute. In the low-energy part of the spectra, the dominance of the majority intensity above that of the minority at  $E_F$  also remains as the angle increases, but becomes much less pronounced.

The angle-dependent SPIPES spectra in Fig. 35 show no dispersion features such as W(001) showed in the preceding chapter. A comparison with a similar investigation on bulk Fe(001) at  $75^\circ$  incident angle<sup>52</sup> indicates that the structureless character may be intrinsic to Fe(001). An alternative approach in interpreting the data is to consider the theoretical band dispersion for direct transitions. Because the normal-incidence transitions occur around the H point, it is possible to tentatively assign the off-normal d-band final states in the neighborhood of H along the H-N line in the irreducible Brillouin zone, in the fully  $\mathbf{k}$ -resolved scheme, (cf. Ref. 52, "inner potential" model). The band dispersion depicted in Fig. 36 shows that the degenerate level at  $H'_{25}$  splits into three bands from  $H'_{25}$  to N, one of which is quite flat, the other two falling at lower energy. This implies a lower d-band intensity away from the H point, and is consistent with the observation of a less-pronounced minority spin peak (or shoulder, due to the large secondary signal) and more-reduced majority intensity at  $E_F$ , with increasing  $\theta$ .



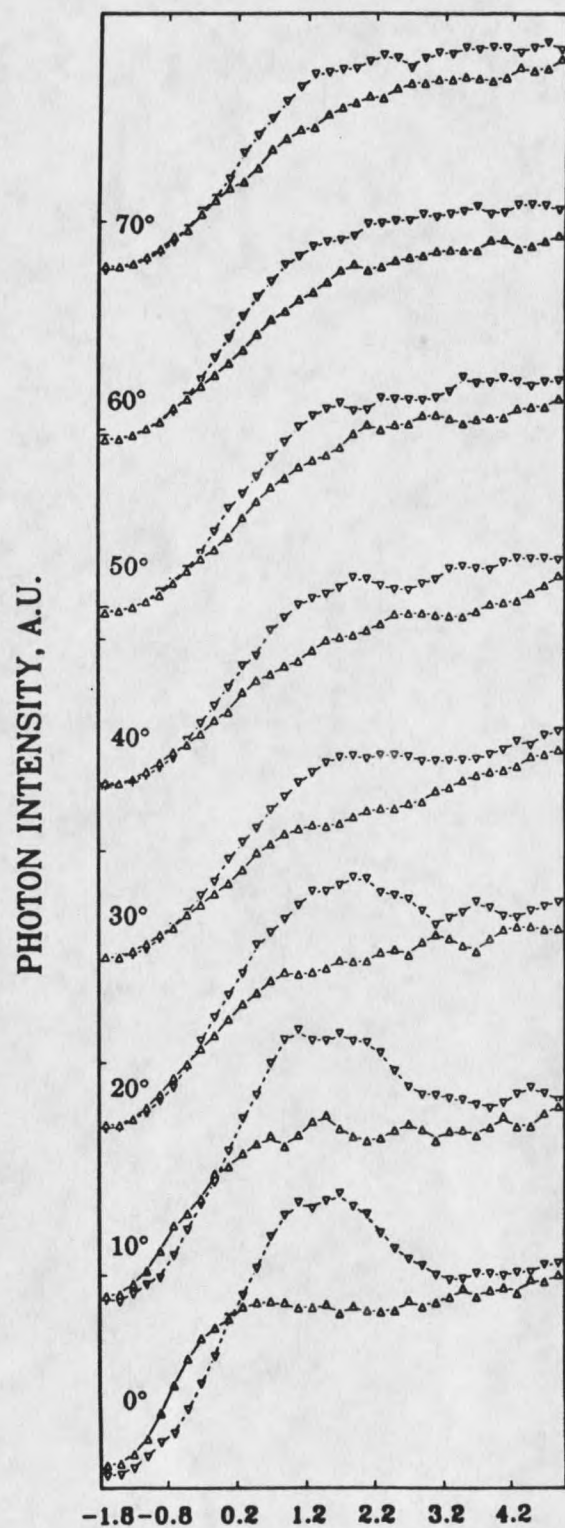


Figure 35. Angle-dependent spectra from bulklike Fe.

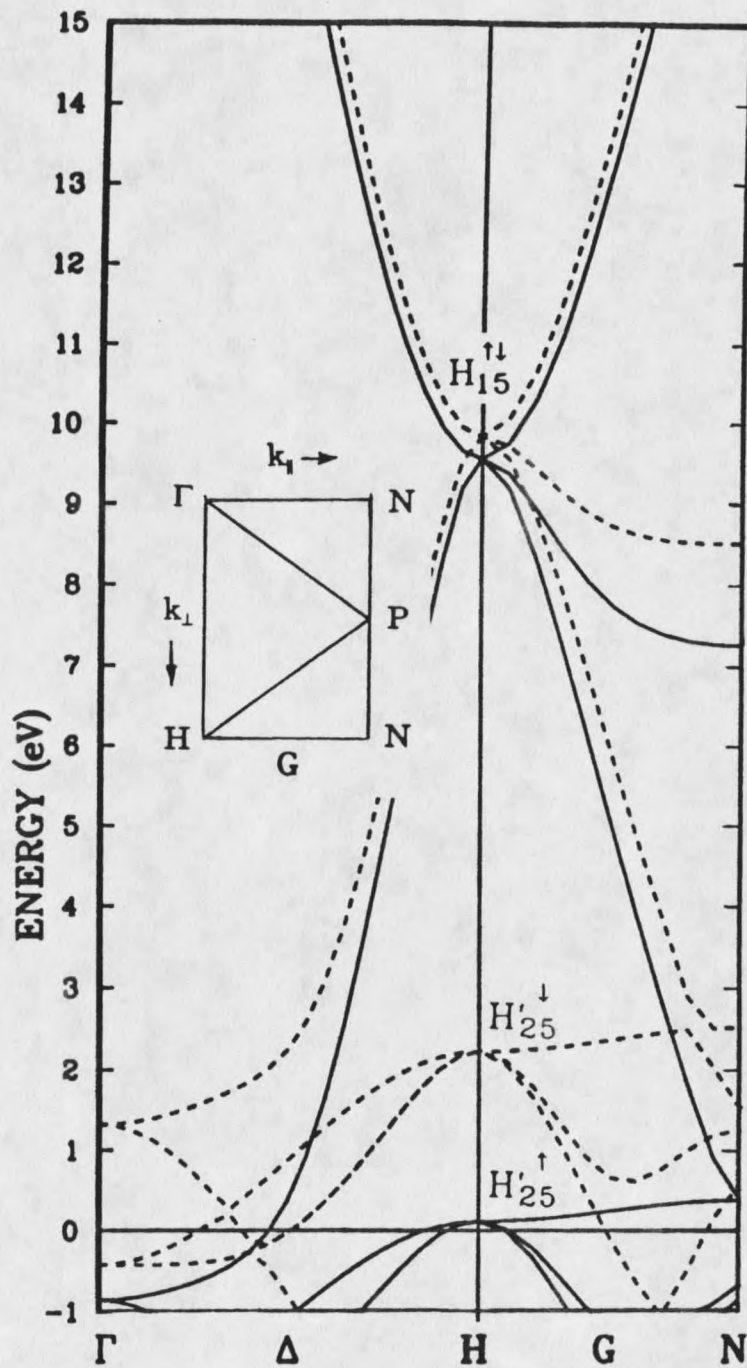


Figure 36. Energy bands of bulk Fe along the G direction.

The inelastic secondary signals become prominent signals with increasing  $\theta$ , increasing almost linearly with electron incidence energy. As discussed in Chapter 2, the inelastic process involves inelastic scattering, mostly electron-hole pair creation, followed by a radiative transition in which a photon of energy near 9.8 eV is emitted. The increase of such a process is believed to be related to the increased electron energy loss cross section at a grazing incident angle, since in this case the incident electrons travel a longer time just outside the metal surface while interacting with the material. Further, the epitaxial overlayers are less perfect than a single crystal surface. Imperfection in the overlayer and the surface and interface of the thin film sample may play an important, but yet unclear, role for scattering and energy loss, since the inelastic contribution to the SPIPES spectra seems to increase much faster at higher angles for the thin film sample than for a single crystal surface.

The inelastic signals exhibit a large polarization (spectral asymmetry) due to the spin-dependent scattering process that usually is investigated by spin-resolved electron energy loss spectroscopic techniques.<sup>55</sup> The idea can be obtained from the illustration of the inelastic process in Fig. 3 in Chapter 2. When the incident electron of energy  $E_i$  loses an energy  $\epsilon$  falls to a energy level  $E_i'$  and then undergoes a radiative transition, an electron-hole pair is simultaneously created across  $E_F$  gaining that energy  $\epsilon$ . The hole state and the two electron states involved in the process carry important information about the spin-split electron band states.

#### D. Thickness-Dependent SPIPES from Fe Monolayers

Up to this point, it has been satisfactory to interpret our results using the electron band picture plus scattering mechanisms. Now when the Fe film's thickness is reduced from four to one atomic layer, the normal-incidence spectral asymmetry  $A$  decreases linearly with the reduced amount of Fe, (Fig. 33). The reduction of the majority( $\uparrow$ ) spin intensity at  $E_F$  is consistent with the surface magnetic enhancement picture (Section A). However, the  $\uparrow$  spin peak does not fall below  $E_F$  for thinner films as a result of enhanced magnetic moment, but, instead, it moves towards higher energy, Fig. 33. The  $\uparrow$  spin intensity maximum is at  $\sim 1.5$  eV at one monolayer Fe thickness, while the  $\downarrow$  spin intensity stays reasonably unchanged except for a reduction in height caused by the smaller amount of Fe. Thus it has a reduced magnetization, just as if the temperature had been increased. Because the SPIPES measurements were taken with the sample at room temperature, we conjecture that the Curie temperature  $T_C$  for the system might be different (lower) with reduced Fe thickness in the monolayer scale. In other words, a gradually increasing  $T/T_C$  is equivalent to a  $T_C$  that is reduced from that of bulk Fe.

As supporting evidence, we recall that in a temperature-dependent SPIPES investigation of bulk Fe(001)<sup>52</sup> it was reported that the minority and majority peaks tend to merge at about 1eV as  $T$  was increased. That is consistent with our observation if we assume that the Fe multilayers have electron structure and  $T/T_C$  dependence similar to that of the bulk. Also, a theoretical temperature-dependent Fe(001) investigation<sup>29</sup> shows that when  $T/T_C$  increases the two peaks (majority and minority) move together at the  $\bar{\Gamma}$  point of the SBZ

both in the case of a surface layer and for the bulk. More explicitly, studies of ultrathin metallic magnetic films show that  $T_c$  can be reduced substantially and gradually with reduced film thicknesses.<sup>56</sup>

Within this picture, when  $T/T_c$  increases as the effective  $T_c$  decreases with reduced Fe thickness, the magnetization is reduced monotonously as described in Chapter 2. Therefore it is possible by means of SPIPES to investigate the temperature-dependent electronic structure of magnetic thin films. The local-band picture can be viewed as an average of fluctuating short-range magnetic ordering over a few Å scale that will produce an extraordinary peak (see Chapter 2) of opposite spin at the energy of an ordinary spin peak. The disordered-local-moment picture generally predicts the merging of peaks at an energy between the corresponding exchange-split peaks, (see Chapter 2). The major issue is the "correlation distance"  $\Lambda$  of the spin-density fluctuations in the itinerant magnetic system.

Figure 37 shows theoretical spectra of Fe at  $H'_{25}$  [Ref. 28]; the parameters are similar to those of the model spectra in Fig. 8. The dashed lines represent the zero-temperature energies of the  $H'_{25}^{\uparrow}$  and  $H'_{25}^{\downarrow}$  states, respectively, and the dotted line is the non-magnetic  $H'_{25}$  energy. The solid/dashed curves are  $\uparrow/\downarrow$  spin intensities respectively. The left panels are the magnetic state at elevated temperature  $T/T_c=0.85$  for the bulk, and the right panels are for the non-magnetic case  $T/T_c>1$ . The top panels show results for short-range order (local-band picture) described by a correlation parameter  $\Lambda=5.4\text{\AA}$ ; here the extraordinary peaks occur at essentially the ordinary peak energies. The changes of the two spin peaks at elevated temperatures are extremely asymmetric because the  $H'_{25}^{\downarrow}$  point is at the top of the bcc Fe d-band.<sup>28</sup> The lower panels show the results of the disordered-local-moment picture with a

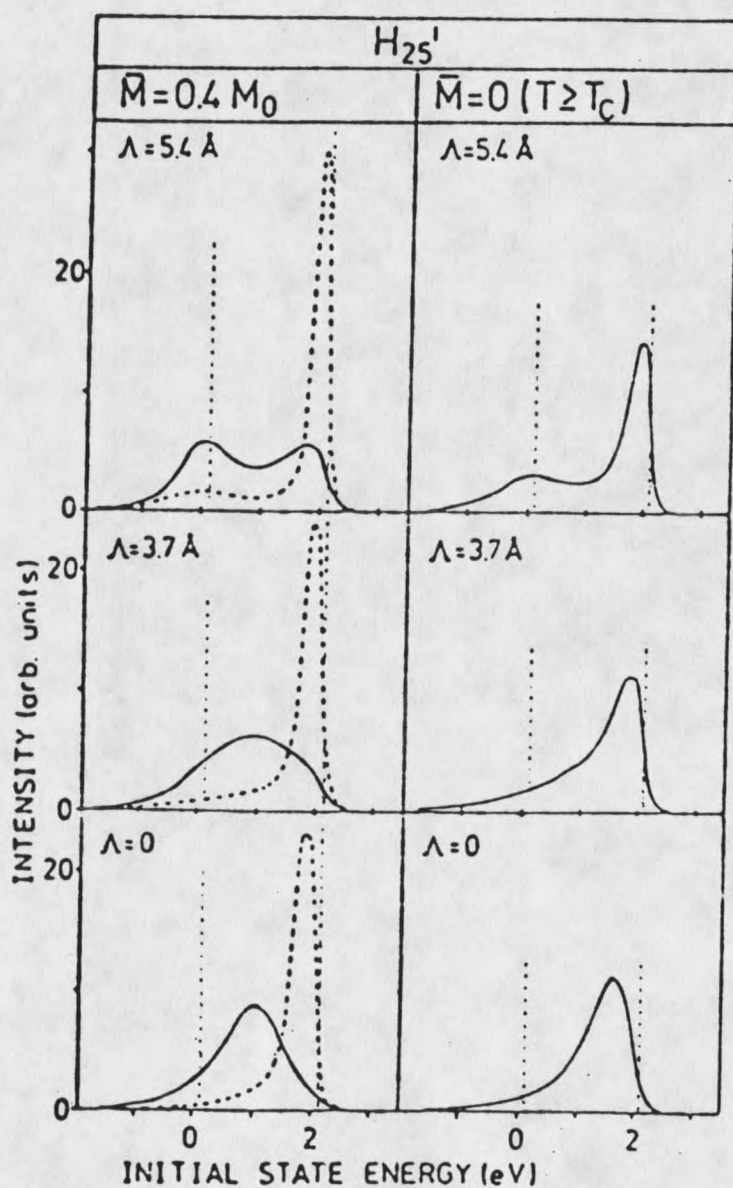


Figure 37. Theoretical Fe spectra for spin-polarized inverse photoemission from the  $H_{25}'$  state. The presentation is the same as in Fig. 8. Adapted from Ref. 28.

correlation parameter  $\Lambda=0\text{\AA}$ . The two spin peaks merge asymmetrically for the same reason, with the minority spin peak remaining at about the same position and the majority peak moving upward. The middle panels are for intermediate range  $\Lambda=3.7\text{\AA}$ .

Since it has been established that the two major peaks in the SPIPES spectra for a bulklike sample are from the transitions near the H point and the evidence strongly suggests that reduced film thicknesses tends to lead to a reduced  $T_c$ , it is reasonable to compare our results for thinner Fe films with the theoretical spectra for increased  $T/T_c$ , although the instrumental resolution prevents one from comparing the spectral shape directly. First, it is encouraging to notice that the energies of the majority and minority spin peaks are essentially at the same position as in the theoretical calculation, namely, near  $E_F$  for the majority spin and around or below 2 eV for the minority spin. Second, the minority peak is essentially stationary as  $T/T_c$  increases. Further, the majority peak moves essentially as one feature towards higher energy up to  $\sim 1.5\text{eV}$ . These features are in good agreement with the theoretical prediction of the disordered-local-moment picture.

On the basis of the concept of a reduced  $T_c$  for thinner films, our results may be used to examine the correlation length of itinerant magnetic system beyond the Stoner model for 3d metallic ferromagnets. Our results favor the disordered-local-moment picture.

## CHAPTER 6

## Co ON W(001)

The morphology, electronic and magnetic properties of ultrathin Co films on W(001) were also studied. A distorted hexagonal overlayer structure was found. In-plane magnetization was detected, and the spin-split electronic structure was studied.

A. LEED Results

Co was vapor-deposited on the clean W(001) surface at room temperature. The W(001) surface preparation, Co evaporator type and QCO thickness monitor were the same as described in the previous chapters for Fe. Auger analysis showed that with increasing Co coverage the W substrate signal diminished quickly to the noise level for an amount of Co comparable to that of Fe on W. Such behavior implies epitaxial layer-by-layer growth, as for Fe on W(001), and the same surface energy argument applies to the Co-W system, i.e., the Co with smaller cohesive energy generally tends to grow a uniform layer on top of a W surface with larger cohesive energy, as indicated in Table 2.

Figure 38 shows a LEED pattern of a Co overlayer on W(001) together with a  $p(1 \times 1)$  pattern for clean W(001) at the same LEED beam energy. The sharp LEED pattern of the Co overlayer indicates a long range order of the Co atoms at the surface. Yet the symmetry of the Co LEED pattern is significantly



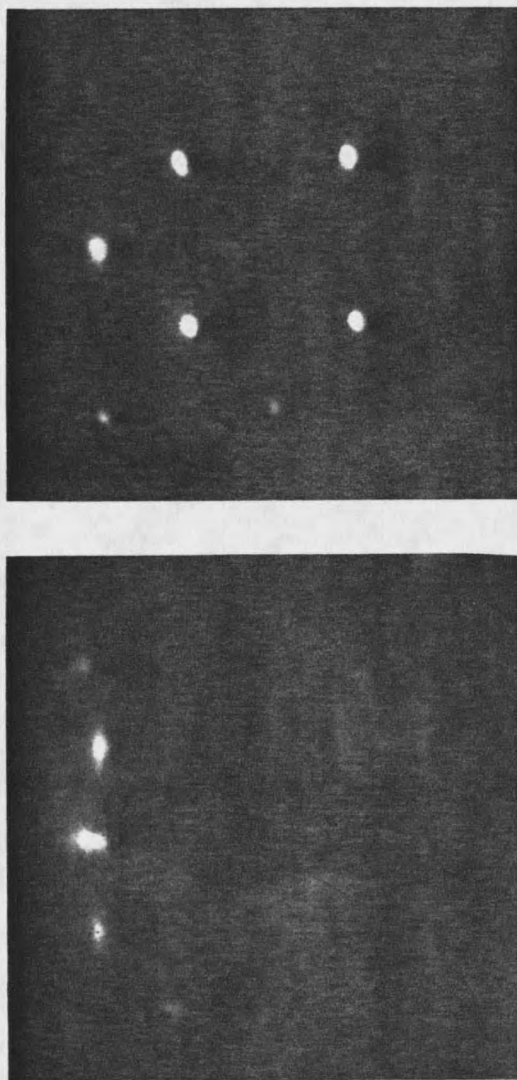


Figure 38. LEED patterns of W(001)p(1×1), top, and Co/W(001), bottom, which is illustrated by drawing in Fig. 39.

different from that of the Fe, indicating a different overlayer morphology. The (1,0) spots have disappeared, the (1,1) spots have become streaky along radial direction, and there are two additional spots around each (1,1) spot, which is streaky in the other direction. Because LEED reflects the symmetry of the surface atomic net, the lack of a simple translational symmetry in the originally observed LEED patterns implies the Co grows in a complex structure at the W(001) surface. The streaky Co LEED spots in two directions provide a clue for decomposing the original pattern into two sets of simple patterns, each containing a same distorted hexagonal LEED pattern rotated  $90^\circ$  with respect to the other, as illustrated in Fig. 39. Each pattern corresponds to a Co overlayer structure, which is distorted hexagonal and aligned with respect to the W(001) substrate, as can be seen in Fig. 39. The streaky LEED spot shape indicates elongated domains of each orientation, caused by a preferred growth in the direction orthogonal to that of the LEED spot elongation. The two domains have equal probability of nucleation and growth on top of the 4-fold-symmetric substrate surface.

A monolayer Co has an atomic density twice that of the W(001) surface when aligned perfectly on W(001) surface, as depicted in Fig. 39c. This implies that about twice the number of atoms have to be deposited to complete a single Co monolayer than for an Fe pseudomorphic monolayer. Since the W(001) surface has an atomic density of  $1.0 \times 10^{15}$  atoms/cm<sup>2</sup>, we infer a  $2.0 \times 10^{15}$  atoms/cm<sup>2</sup> atomic density for the Co monolayer, in contrast to the bulk Co hexagonal plane density of  $1.8 \times 10^{15}$  atoms/cm<sup>2</sup>. Specifically, the distortion may be described as a dilation by 2.5% in one direction and a compression of 10.9% in the orthogonal direction; or, in terms of interatomic distances in the hexagonal plane, one of the three axes is compressed from 2.52 Å to 2.24 Å

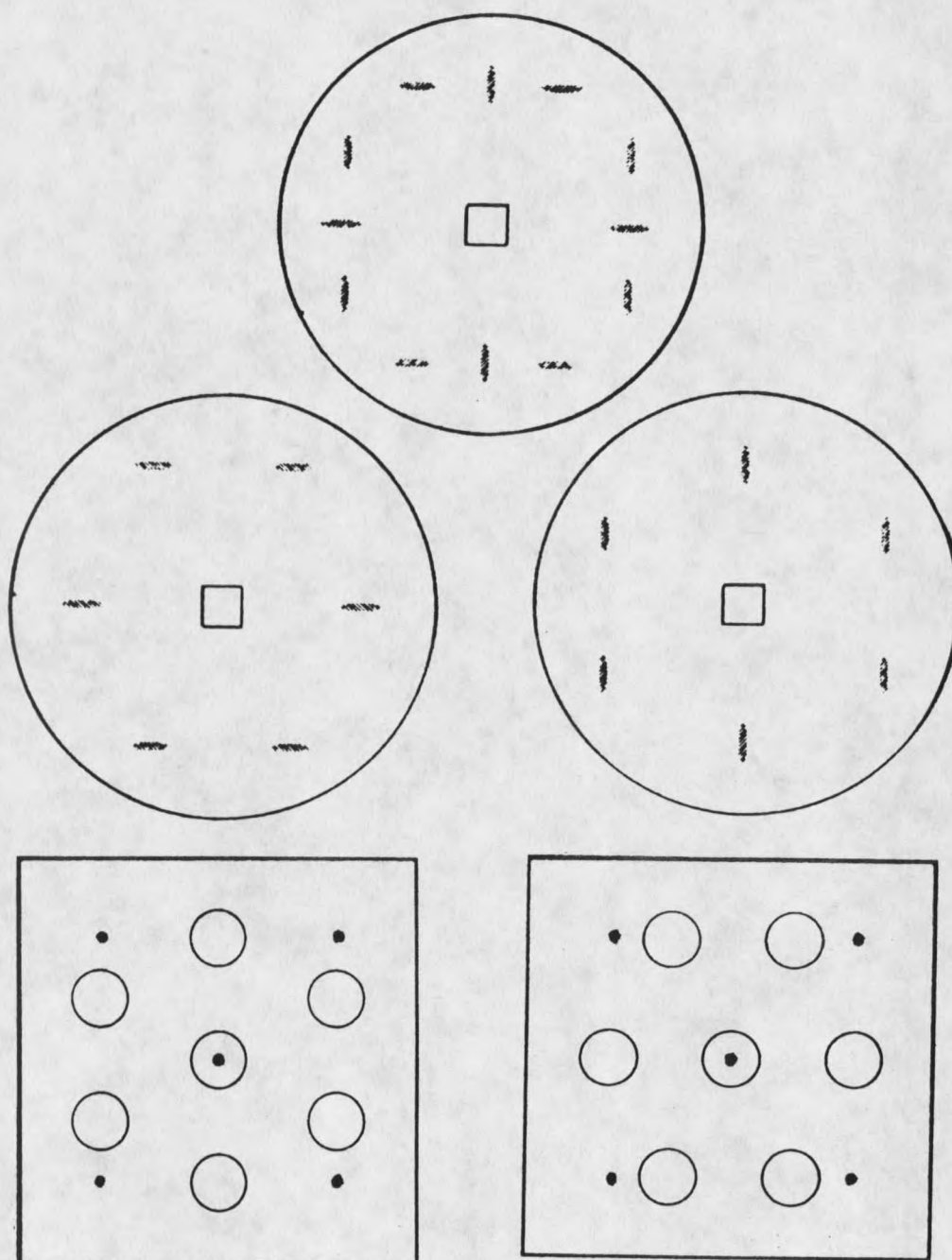


Figure 39. Illustration of decomposition of the Co/W(001) LEED patterns. The observed LEED pattern is shown on the top, with the blocked (0,0) spot represented by a square. The middle drawings represent the two orthogonally oriented distorted-hexagonal patterns, each with spots streaky on the same direction. The corresponding surface atomic nets are shown below each pattern, with open circles representing the Co atoms, and the small dots the substrate W atoms.

and the other two to 2.50 Å. The strains can be released through the structural domain boundaries, which may prevent the domains from growing beyond a certain size. The hexagonal structure should be the favored adsorption structure since it is the highest density plane and has the largest interplane distance in either hcp or fcc crystal structures. As in the Fe case, only as-deposited films are discussed unless otherwise mentioned, because an annealing treatment causes irreversible changes in the overlayer structure.

### B. SPIPES Results

Figure 40 shows the normal incidence SPIPES spectra of one and two monolayers of Co on W(001), together with a non-polarized spectrum of clean W(001). The Co/W(001) samples were previously magnetized in 400 Oe field along  $\bar{Z}$  of W(001) SBZ, and measured in remanent magnetization, as described in Chapter 3. In the spin-polarized spectra from Co/W(001), the majority (minority) data points are denoted by  $\Delta$  ( $\nabla$ ), the same as for the Fe spectra. Although the relative intensity with respect to the W spectrum is not significant, one can see an increase of intensity for both spins at ~1-2 eV range for the one monolayer of Co from the clean W spectrum, indicating the development of unoccupied Co 3d band states. In the one monolayer sample, any minority spin spectral dominance, if it exists, is comparable to the signal fluctuations, and hence one cannot infer the existence of remanent magnetization in the Co monolayer sample at room temperature. This small margin of polarization could also suggest a remanent magnetization perpendicular to the spin sensitive direction of our measurement. This would imply that the total thin film anisotropy favors a perpendicular easy axis of

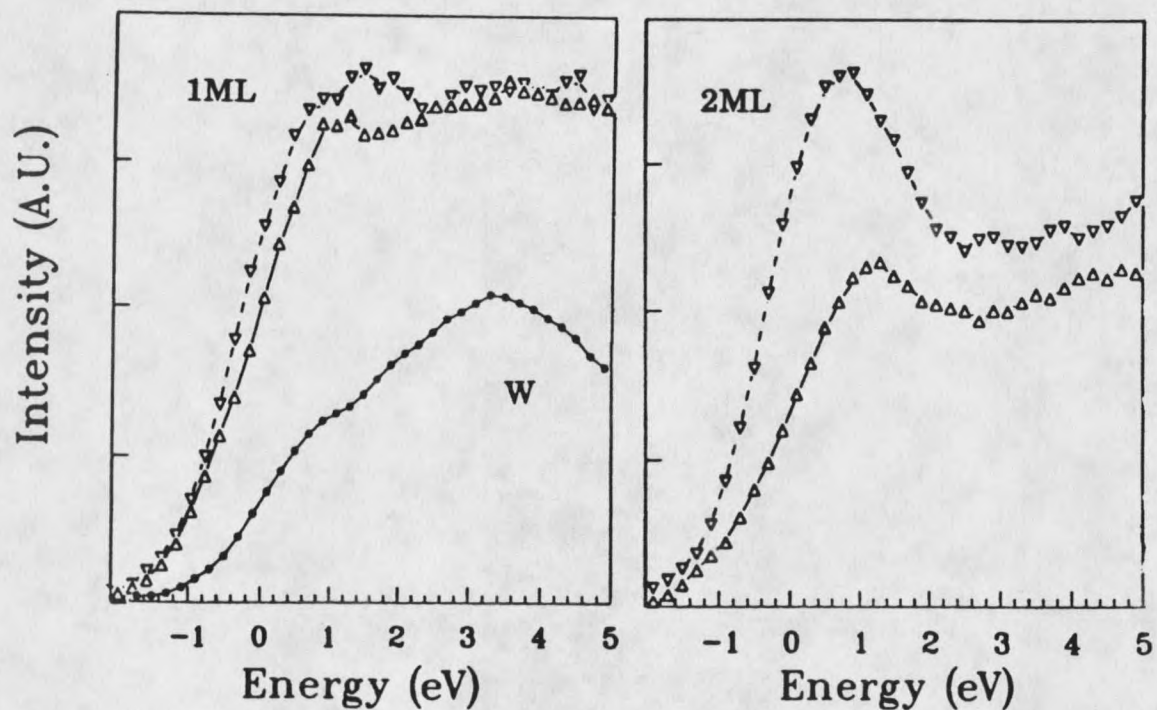


Figure 40. The SPIPES spectra for one and two monolayers of Co on W(001). The data points are denoted by  $\Delta$  and  $\nabla$  for majority and minority spin, respectively. The IPES spectra of clean W(001) is included together with the one monolayer spectra for comparison.

magnetization, as in hcp-Co where the uniaxial crystal anisotropy also favors the easy axis perpendicular to the hexagonal plane.

When the Co thickness increases to two monolayers, there is a predominant minority spin peak with a maximum at 0.8 eV, as the top curves in Fig. 40 show. The majority spin intensity, while always below the minority, shows a smaller peak at about 1.2 eV above  $E_F$ . That it is possible to measure the large spectral polarization indicates the existence of ferromagnetic ordering in the sample, and that the remanence is in the film plane.

In the case of in-plane remanent magnetization, the influence of the mixed structural domains of the Co overlayers should be taken into account in the following way. The leading terms of in-plane anisotropy energy in a single crystal domain can be written generally as

$$E_{\text{anisotropy, ||}} = K_X^{(2)} \cdot \cos^2(\theta_X) + K_Y^{(2)} \cdot \cos^2(\theta_Y) \quad (14)$$

where  $\theta_X$  and  $\theta_Y$  are the angles between the magnetization direction and the in-plane axes, X and Y, chosen parallel to the two orthogonal mirror planes. The coefficients  $K_X^{(2)}$  and  $K_Y^{(2)}$ , which are equal in an additional n-fold ( $n > 2$ ) rotationally symmetric single crystal layer, are no longer equal because of the structural distortion. Depending on which  $K^{(2)}$  is smaller, the remanent magnetization will lie in the corresponding direction. Therefore, one group of domains has its remanent magnetization lying in the SPIPES spin-sensitive direction, yielding the "true" spin-polarized signals. The other group has its remanent magnetization lying transverse to the SPIPES spin-sensitive direction, producing essentially non-polarized signals.

This concept can be utilized to obtain the true spin-resolved SPIPES from a

single domain by subtracting 50% of the spin-averaged spectrum from the spectra of both spin directions. The result for two monolayers of Co is shown in Fig. 41. The dominant minority peak at 0.7 eV is essentially unchanged, while the majority peak has been largely removed.

While the electronic structure of distorted hexagonal monolayers has not been studied theoretically, comparison is made with that of hcp bulk Co. One such band structure is shown in Fig. 5.<sup>57</sup> It has d bands ( $\Delta_5, \Delta_6$ ) along the  $\Delta$  direction, and is in fairly good agreement with a more recent self-consistent hcp-Co band structure calculation.<sup>58</sup> The allowed direct transition is marked by a vertical line with energy difference equal to 9.8 eV. The final (lower) states include minority spin only near 0.7 eV above  $E_F$ . This is consistent with the minority spin peak observed at 0.8 eV for the hexagonal Co multilayers.

The hcp Co band structure in Fig. 42 shows the corresponding majority spin d bands below  $E_F$ ; the majority spin DOS for the d bands are also below  $E_F$  while part of the minority spin d bands are above  $E_F$  (cf Chapter 2). Therefore, the majority spin peak in the spectra for two monolayers of Co in Fig. 40 appears to be contradicted by the lack of majority final states. The adjustment for two orthogonal domains, which leads to the spectra in Fig. 41, has helped to remove this contradiction by suppressing the majority spin peak.

However, one cannot totally exclude the existence of a majority spin peak, since even after the adjustment there is still a shoulder at ~1.4 eV. There are a number of unknown factors involved in this study of Co layers which could explain the majority feature found in the unoccupied states. The first factor is the lack of SPIPES studies for the hexagonal face of bulk Co which could test whether such majority spin features exist. The ordinary IPES study based on the assumption that all unoccupied-state features in Co are from the minority



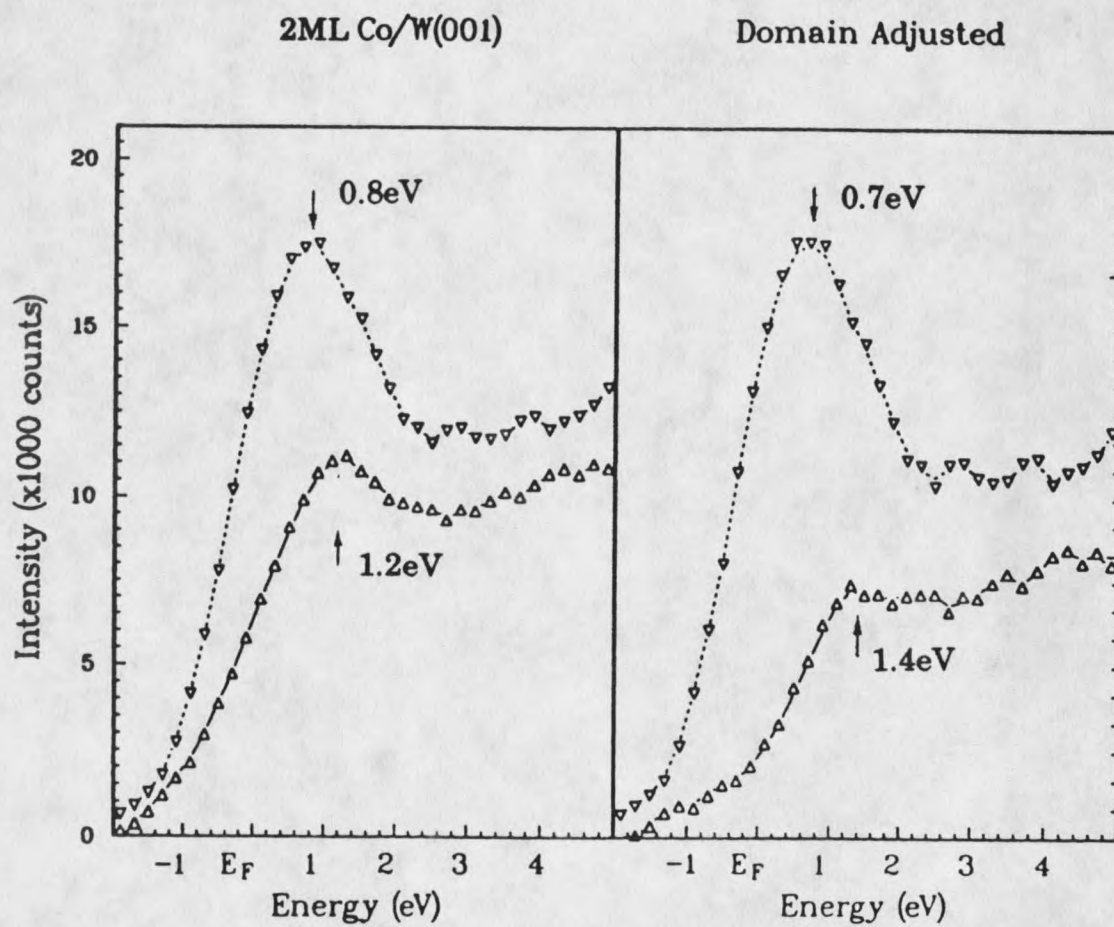


Figure 41. Right: domain adjusted SPIPES spectra from two monolayers of Co on W(001). Left: the SPIPES spectra before such adjustment.



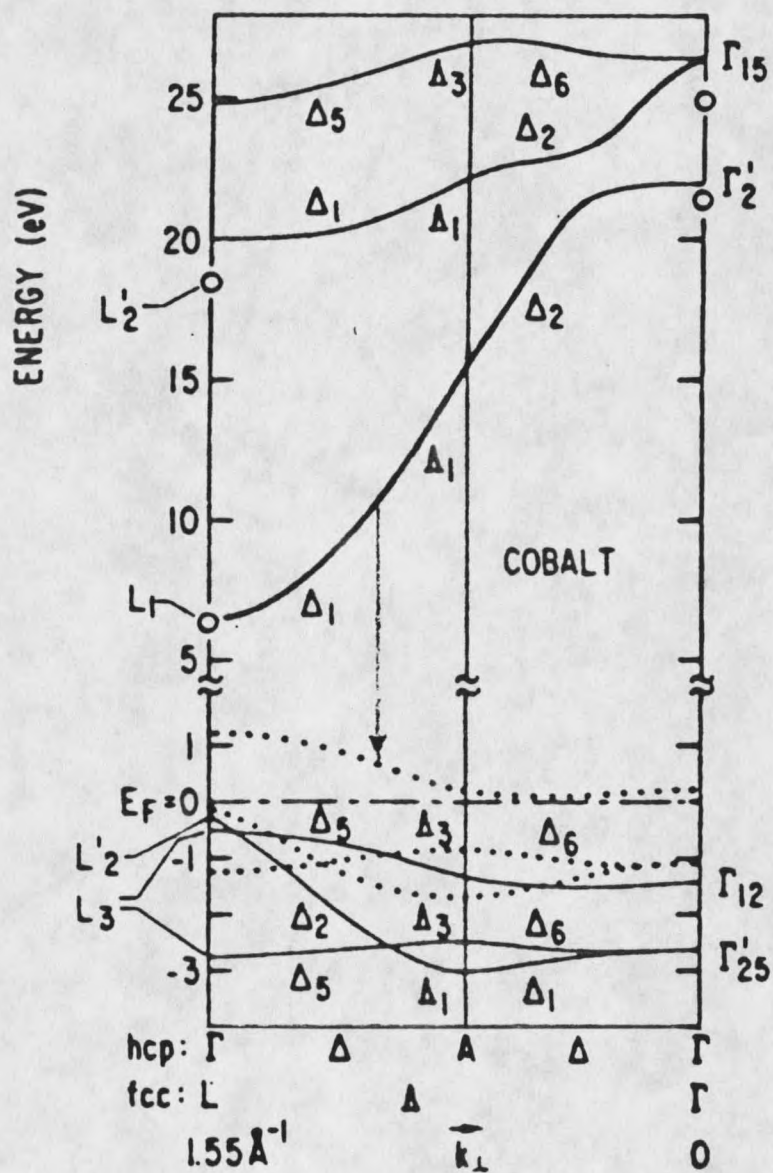


Figure 42. Theoretical energy bands of hcp Co along the direction normal to the hexagonal plane. Adapted from Ref. 57.

d-band states does not resolve the issue. Secondly, two monolayers of distorted hexagonal Co on W(001) need not possess a band structure similar to that of hcp Co. Further,  $T_c$  for the monolayer-scale Co overlayer is possibly lower than the bulk Curie temperature  $T_c$  and close to room temperature; this in turn will cause the electronic structure to differ substantially from the zero-temperature properties. For example, the local-band picture suggests a small "extraordinary" majority peak at the energy of the corresponding minority spin peak at elevated temperature (see Chapter 2). It requires further temperature-dependent investigations to verify this possibility, and  $T_c$  needs to be determined for the two monolayer Co system.

Finally it is necessary and instructive to discuss the remaining majority spin feature in terms of the secondary contributions, as if this is not the primary feature. Let us assume, in the Co case, that occupied states have mainly majority spin and unoccupied states have only minority spin. Then the secondary contribution will mostly involve spin-flip energy loss, i.e., inverting the spin polarization while losing an amount of energy, followed by a radiative transition. Because electron-hole pair creation, the predominant energy loss mechanism, will likely have an electron excited from a majority d-band state to a minority d-band state across  $E_F$ , (cf. Fig. 3 in Chapter 2), the incident electron will undergo a spin-flip process also. Thus the majority spin electrons incident at higher energy will have a large dipole radiative decay cross section after the spin-flip energy loss just as the minority incident electrons do, except that the majority spin electrons should have an extra amount of energy to compensate the energy loss. The average amount of energy loss in this case should be comparable to the d-band exchange splitting, say  $\sim 0.85$  eV. This could be responsible for the majority spin shoulder of the adjusted spectrum in

Fig. 41 located at higher energy,  $\sim 1.4$  eV, i.e., 0.7 eV above the minority spin peak position.

Based on the assumption that the distorted hexagonal Co overlayer will develop an electronic structure close to that for the hcp-Co, our results provide evidence of the spin-flip energy loss. This possibility should be investigated carefully by SP-EELS. On the other hand, the minority feature agrees very well with the hcp-Co band structure.

## CHAPTER 7

## SUMMARY

In order to investigate the spin-dependent electronic structure and magnetic properties of 3-d transition metals and 2D magnetic systems, an experimental system containing spin-polarized inverse photoemission spectroscopy and magnetic thin film sample preparation and characterization apparatus was developed at Montana State University. Novel ultrathin magnetic films of 3-d transition metals, Fe and Co, were epitaxially grown on top of a clean W(001) substrate. Auger and LEED were used to characterize the thin film growth and morphology. Evidently atomically smooth monolayers were achieved.

The W(001) surface was studied by ARIPEs to elucidate its unoccupied electronic band structure. The dispersion of the peaks is generally consistent with the bulk band structure.

Ultrathin Fe films were investigated for thickness from one to four atomic layers. The Fe grows in a square lattice similar to that of a Fe(001) surface structure. The first monolayer of Fe grows pseudomorphically on W(001) with ~10% lattice dilation due to the mismatch, and is also ferromagnetically ordered in the film plane. Normal incidence SPIPES spectra show that four monolayers of Fe have electronic structure in good agreement with the bulk bcc-Fe(001) band structure. The angle-dependent SPIPES investigation shows that the prominent minority d-band peak is essentially stationary along  $\bar{\Sigma}$  of the surface Brillouin zone. The inelastic contribution exhibits a large polarization that may be of potential help in understanding the spin-dependent

electron-solid interaction.

The thickness-dependent SPIPES results suggest a reduced effective  $T_c$  for monolayer-scale Fe thin films. Variation of thickness thus becomes a novel way of investigating the "temperature-dependent" electronic behavior in the itinerant magnetic system. The SPIPES peaks correspond to the final states near the  $H_{25}^{\uparrow}$  and  $H_{25}^{\downarrow}$  points of the bulk Brillouin zone, and these states merge together with increasing effective  $T/T_c$ , a result which suggests a shorter correlation distance of the spin-density fluctuations when the spectra are compared with theoretical spectra. The results favor the disordered-local-moment model in the modern theory of the itinerant-electron magnetic system.

Co overlayers on W(001) grow in a complicated structure of elongated domains, each with an unusual distorted hexagonal lateral structure, with two types of domains which are orthogonal to each other. The ideal atomic monolayer of such a structure contains twice the atomic density found for the substrate surface layer. The first monolayer of Co does not show in-plane magnetization, while two monolayers of Co produce an in-plane magnetization with a pronounced minority spin peak at  $\sim 0.8$  eV and also a majority spin peak at  $\sim 1.2$  eV.

Since the Co unoccupied d-band structure was studied by spin-polarized IPES for the first time in this thesis, to our knowledge, there is no external evidence to support or refute the supposition that the Co overlayer system develops the bulk hcp-Co electronic structure. The SPIPES spectra were compared with the theoretical band structure of hcp-Co, and the minority feature was found to be in agreement with the known properties of the minority d-band. The majority peak, on the other hand, is not consistent with the characteristics of the Co electronic structure. The majority peak could be

at least partly due to the in-plane remanent magnetization direction of the distorted domain structure of the Co overlayer, while other contributions such as the electronic structure at elevated temperature and spin-flip inelastic contributions may also be involved.

The SPIPES technique has demonstrated the important role it can play in the investigation of spin-dependent unoccupied electronic structure, especially for the 3-d transition metal bulk and surface magnetism. The present work has shown a great potential for further investigation in this direction, including work on other spin-dependent electronic structures besides elemental materials, including magnetic semiconductors and amorphous materials. The present work on the spin-polarized electron technique could also be extended to other spin-polarized experimental techniques such as scattering (spin-polarized LEED) and energy loss spectroscopy (SPEELS).

It is the author's hope and belief that including the new dimension of freedom of spin, - which is an intrinsic property of electrons of fundamental importance, - in experimental solid state and surface science will greatly help investigators to uncover nature's secrets, contribute to the development of technology, and ultimately improve the life of mankind.

REFERENCES

## REFERENCES

1. E.C. Stoner, Proc. Roy. Soc.(London) A154, 656 (1936); also see E.P. Wohlfarth, Rev. Mod. Phys. 25, 211 (1953).
2. V.L. Moruzzi, J.F. Janak and A.R. Williams, Calculated Electronic Properties of Metals, Pergamon, New York, 1978; D.A. Papaconstantopoulos, Handbook of The Band Structure of Elemental Solids, Plenum, New York, 1986.
3. Z.-Y. Zhu and J. Hermanson, Phys. Rev. B 27, 2092 (1983).
4. L.N. Liebermann, D.R. Fredkin and H.B. Shore, Phys. Rev. Lett. 22, 539 (1969); L. Liebermann and J. Clinton, Phys. Rev. Lett. 25, 232 (1970).
5. V.L. Moruzzi, P.M. Marcus, K. Schwarz and P. Mohn, Phys. Rev. B 34, 1784 (1986).
6. J.G. Gay and Roy Richter, Phys. Rev. Lett. 56, 2728 (1986)
7. A.J. Freeman and C.L. Fu, J. Appl. Phys 61(8), 3356 (1987).
8. J.B. Pendry, J. Phys. C 14, 1381 (1981).
9. G. Thörner and G. Borstel, Solid State Comm. 47, 329 (1983).
10. D.W. Jepsen, Th. Fauster and F.J. Himpsel, Phys. Rev. B 29, 1078 (1984).
11. G. Thörner and G. Borstel, Solid State Comm. 49, 997 (1984).
12. R. Feder and A. Rodriguez, Solid State Comm. 50, 1033 (1984).
13. There is a two orders of magnitude difference between momentum vectors of an electron and a photon in the energy range we studied, either in the crystal or free space. The electron  $\mathbf{k}$  vector in the crystal  $\approx$  the reciprocal lattice  $2\pi/a_0 \sim 1\text{\AA}^{-1}$ , while for a 10eV UV photon,  $|\mathbf{q}|=2\pi/\lambda \sim 10^{-2} \text{\AA}^{-1}$ .
14. G. Borstel and G. Thörner, "Inverse photoemission from solids: theoretical aspects and applications", Surf. Sci. Rep. 8, 1 (1987).
15. Volker Dose, Prog. Surf. Sci. 13, 225 (1983).
16. This difference can be seen from differential final-state phase space,  $k^2 d\Omega dk$ . In PES,  $k^2$  leads to  $2m_e E_k$  for electron, while in IPES it leads to  $(\hbar v/c)^2$  for photon; and their ratio is  $10^6$  for electron kinetic energy and photon energy of 10eV.
17. The first spin- and angle- resolved PES experiments were done in 1980, see E. Kisker, W. Gudat, E. Kuhlmann, R. Clauberg and M. Campagna, Phys. Rev. Lett. 45, 2053 (1980); the IPES counterpart in 1982, see J. Unguris, A. Seiler, R.J. Celotta and D.T. Pierce, Phys. Rev. Lett. 49, 1047 (1982); both on Ni(110).



18. C. Kittel, Introduction to Solid State Physics, 3rd ed. John Wiley & Sons, New York, 1967.
19. A.J. Freeman and C.L. Fu, J. Appl. Phys. 61(8), 3356 (1987); C.L. Fu and A.J. Freeman, J. Magn. & Magn. Mater. 54-57, 777 (1986).
20. for a monolayer on Ag(001), J.G. Gay and Roy Richter, J. Appl. Phys. 61(8), 3362 (1987).
21. A. Zangwill, Physics at Surfaces, Cambridge, New York, 1988.
22. X.Y. Zhu, Ph.D. Thesis, Montana State University, 1983; H. Huang, Ph.D. Thesis, Montana State University, 1985.
23. P.A. Dowben, S. Varma, Y.J. Kime, D.R. Mueller and M. Onellion, Z. für Physik, July 25, 1988.
24. G. Allan, "Itinerant electron surface magnetism", Surf. Sci. Rep. 1, 121 (1981).
25. H. Capellmann, ed. Metallic Magnetism, Springer-Verlag, Berlin, 1987.
26. B.L. Gyorffy, J. Kollar, A.J. Pindor, G.M. Stocks, J. Staunton and H. Winter, in NATO Advanced Study Institute Series B113, W. Temmermann and P. Pharisean eds. Plenum Press, New York, 1984.
27. T. Moriya, Ann. Rev. Mater. Sci. 14, 1 (1984); T. Moriya, Spin Fluctuations in Itinerant Electron Magnetism, Springer-Verlag, Berlin, 1985.
28. R. Clauberg, E.M. Haines and R. Feder, Z. Phys. B 62, 31 (1985).
29. H. Hawasage, J. Phys. F: Met. Phys. 17, 165 (1987).
30. D.T. Pierce and F. Meier, Phys. Rev. B 13, 5484 (1976).
31. D.T. Pierce, R.J. Celotta, G.-C. Wang, W.N. Unertl, A. Galejs, C.E. Kuyatt and S.R. Mielczarek, Rev. Sci. Instrum. 51(4), 478 (1980).
32. The p-GaAs(100) wafer, M/A Laser Diode Labs. 0.014 inch thick, one side polished, doping concentration is  $1.5-2.9 \times 10^{18} \text{ Zn/cm}^3$ .
33. Laser diode LCW-10, M/A Laser Diode Labs., nominal 8000Å wavelength, 10 mW cw.
34. L.E. Klebanoff, R.K. Jones, D.T. Pierce and R.J. Celotta, Phys. Rev. B 36, 7849 (1987), where  $P = 0.27(3)$  was reported.
35. Keith D. Jamison, Ph.D. thesis, Rice University, page 20 (1984),  $P = 27\%$ .
36. H. Hopster, private communications,  $P = 0.28 \pm 0.02$ .

37. Spiraltron electron multiplier, popularly known as Channeltron, model SEM-09, Galillio, 9mm nominal dia.
38. Disks of 1 inch dia.x 2mm thick  $\text{CaF}_2$  or  $\text{SrF}_2$  crystals, Harshall Crystals.
39. The light beam passed through a LiF window. The light curve was measured by two types of detectors: sodium salicylate and a GaAsP-Au Schottky photodiode, the latter was used to measure the absolute photon flux.
40. 99.99% Research Purity oxygen, Matheson Gas Products.
41. See, for example, Y. Namba and T. Mori, J. Vac. Sci. Technol. A4(4), 1884, (1986), and references cited therein.
42. Ingot, 9mm dia.x 25mm W single crystal, 110 orientation, 99.999%, Puratronic®, Johnson Matthey Chemicals Limited.
43. For example, see J. Anderson, G.J. Lapeyre and R.J. Smith, Phys. Rev. B17, 2436 (1978).
44. N.E. Christensen and R.F. Willis, J. Phys. C12, 167 (1979); R.F. Willis and N.E. Christensen, Phys. Rev. B18, 5140 (1978).
45. I.L. Krainsky, J. Vac. Sci. Technol. A5(4), 735 (1987).
46. D.W. Bullet and P.C. Stephenson, Sol. St. Commun. 45, 47 (1983); P.C. Stephenson and D.W. Bullet, Surf. Sci. 139, 1 (1984).
47. E. Bauer and J.H. van der Merwe, Phys. Rev. B 33, 3657 (1986).
48. U. Gradmann and G. Waller, Surf. Sci. 116, 539 (1982).
49. S. Ossicini, R. Memeo and F. Ciccacci, J. Vac. Sci. Technol. A3(2), 387 (1985).
50. M. Hansen, ed, Consitution of Binary Alloys, 2nd ed. McGraw-Hill, New York, 1958.
51. We should point out for layer-by-layer growth the maximum amplitude ratio ordinarily saturates at unity. When the Fe source was nearly empty this condition did not occur. Because near the end, an Fe-W alloy was formed at the W wire interface and W was deposited along with the Fe, causing an W Auger signal to be observed at thicker coverages. At the end, the bare W wire was left.
52. J. Kirschner, M. Glöbl, V. Dose and H. Scheidt, Phys. Rev. Lett. 53, 612 (1984).
53. J. Callaway and C.S. Wang, Phys. Rev. B16, 2095 (1977).
54. C.S. Wang and A.J. Freeman, Phys. Rev. B 24, 4364 (1981).

55. J. Kirschner, Surf. Sci. 162, 83 (1985).
56. Submonolayer Fe/Au, S.D. Bader, E.R. Moog and P. Grünberg, J. Magn. & Magn. Mater. 53, L295 (1986); gradually reduced  $T_c$  from Ni/Cu, J. Erskine, private communications.
57. F.J. Himpsel and D.E. Eastman, Phys. Rev. B 21, 3207 (1980).
58. T. Jarlborg and M. Peter, J. Magn. & Magn. Mater. 42, 89 (1984).
59. U. Gradmann, J. Korecki and G. Waller, Appl. Phys. A 39, 101 (1986).
60. G.T. Rado, Phys. Rev. B 26, 295 (1982).

APPENDICES

Appendix A Computer Program

Figure 43. Sample FORTRAN program for Fe data analysis and plotting

```

PROGRAM FE

cccccccccccccccccccccccccccccccccccccccccccccccccccccccccccc
C
C   plot SPIPES spectra and spectral asymmetries from magn
C   for magnetic thin films on W(001)
C
cccccccccccccccccccccccccccccccccccccccccccccccccccccccccccc

IMPLICIT REAL (B-H,O-Z)

cccccccccccccccccccccccccccccccccccccccccccccccccccccccccccc
C
C   character strings
C       F1,F2 - file names of each energy scan
C       V1,V2 - comments, dates, etc
C       W1,W2 -
C       X1,X2 -
C       Y1,Y2 -
C
C   data arrays
C       A1,A2 - a pair of as-measured spin spectra
C       A3     - energy range
C       A4,A5 - spin-averaged spectrum and spectral asymmetry
C       A6,A7 - pair of polarization-adjusted spectra, fluc-
C               tuation restored
C       A8,A9 - pair of 3-point-smoothed spectra
C       A10,A11 - pair of polarization-adjusted spectra,
C               smoothed
C
cccccccccccccccccccccccccccccccccccccccccccccccccccccccccccc

CHARACTER*80 F1,F2,V1,V2,W1,W2,X1,X2,Y1,Y2

DIMENSION A1(36),A2(36),A3(36),A4(36),A5(36),A6(36),A7(36),
x          A8(36),A9(36),A10(36),A11(36),X(2),Y(2)

CALL PSCRIPT(7.98,10.99,0.007)
C CALL TK41(4105)
CALL NOBRDR
CALL TRIPLX

```

Figure 43. Continued

```

cccccccccccccccccccccccccccccccccccccccccccccccccccccccccccc
c
c   repeat data plotting procedure from clean W(001) and one to
c   four monolayers of Fe thin films
c
cccccccccccccccccccccccccccccccccccccccccccccccccccccccccccc

DO 999 KK=1,5
  IF (KK.EQ.1) THEN
    F1='T8F141.DAT'
  ELSEIF (KK.EQ.2) THEN
    F1='T8F150.DAT'
    F2='T8F151.DAT'
  ELSE IF (KK.EQ.3) THEN
    F1='T8F148.DAT'
    F2='T8F149.DAT'
  ELSE IF (KK.EQ.4) THEN
    F1='T8F147.DAT'
    F2='T8F146.DAT'
  ELSE
    F1='T8F143.DAT'
    F2='T8F142.DAT'
  ENDIF

  OPEN (UNIT=1, FILE=F1, STATUS='OLD', FORM='UNFORMATTED')
  READ (1) I, M, M1, B, S, R, K, P
  READ (1) V1, X1, W1, Y1
  READ (1) (A1 (J), J=1, 36)

  READ (1) (A3 (J), J=1, 36)
  DO 30 J=1, 36
30  A3 (J) = A3 (J) - 2.7

  IF (KK.NE.1) THEN
    OPEN (UNIT=2, FILE=F2, STATUS='OLD', FORM='UNFORMATTED')
    READ (2) I, M, M2, B, S, R, K, P
    READ (2) V2, X2, W2, Y2
    READ (2) (A2 (J), J=1, 36)
  ELSE
    H4=0.
    DO 20 J=1, 36
    A4 (J) = A1 (J)
    IF (H4.LT.A4 (J)) H4=A4 (J)
20  CONTINUE
    GOTO 900
  ENDIF

c   polarization factor
PO=0.27

```

Figure 43. Continued

```

H4=0.
AL=0.
AH=0.
H7=0.

c   3-pts smoothing A8,A9
    A8(1)=A1(1)
    A8(36)=A1(36)
    A9(1)=A2(1)
    A9(36)=A2(36)
    DO 40 K=2,35
    A8(K)=0.5*A1(K)+0.25*(A1(K-1)+A1(K+1))
    A9(K)=0.5*A2(K)+0.25*(A2(K-1)+A2(K+1))
40  CONTINUE

    DO 50 J=1,36

c   spin-averaged spectra from smoothed, max H4
    A4(J)=(A8(J)+A9(J))/2.
    IF (H4.LT.A4(J)) THEN
    H4=A4(J)
    ENDIF

c   Asymmetry from smoothed, max AH, min AL
    A5(J)=(A8(J)-A9(J))/2./PO/A4(J)
    IF (AH.LT.A5(J)) THEN
    AH=A5(J)
    ELSEIF (AL.GT.A5(J)) THEN
    AL=A5(J)
    ENDIF

c   hypothetical 100% spin spectra from smoothed
    A10(J)=A4(J)*(1.+A5(J))
    A11(J)=A4(J)*(1.-A5(J))

c   statistical fluctuations restored
    A6(J)=A10(J)+(A1(J)-A8(J))
    A7(J)=A11(J)+(A2(J)-A9(J))
    IF (H7.LT.A6(J)) THEN
    H7=A6(J)
    ENDIF
    IF (H7.LT.A7(J)) THEN
    H7=A7(J)
    ENDIF
50  CONTINUE

    DO 60 J=1,36
    A10(J)=A10(J)*110./H4
    A11(J)=A11(J)*110./H4
    A6(J)=A6(J)*110./H4

```



Figure 43. Continued

```

        A7(J)=A7(J)*110./H4
60      CONTINUE
        IF(KK.NE.2) GOTO 70
        DO 70 J=1,34
        A5(J)=A5(J+2)
        A3(J)=A3(J+2)
        A6(J)=A6(J+2)
        A7(J)=A7(J+2)
        A10(J)=A10(J+2)
        A11(J)=A11(J+2)
70      CONTINUE

        CALL CURVE(A3,A6,34,-1)
        CALL CURVE(A3,A10,34,0)
        CALL DASH
        CALL MARKER(6)
        CALL CURVE(A3,A7,34,-1)
        CALL CURVE(A3,A11,34,0)
        CALL RESET('DASH')
        CALL XTICKS(5)
        CALL XGRAXS(-1.,1.,5.,2.5-1./3.4,' ',1,1./3.4,0.)
        CALL ENDGR(0)

C ASYMMETRIES
        CALL PHYSOR(4.5,-1.5+2.*KK)
        CALL AREA2D(2.5,2.)
C      CALL FRAME
        CALL XNAME('$',100)
        CALL XNONUM
        CALL YNONUM
        IF(KK.EQ.2) THEN
        CALL XTICKS(34)
        ELSE
        CALL XTICKS(0)
        ENDIF
        CALL GRAF(-1.8,6.8,5.,-.4,.2,.4)
        CALL VECTOR(0.,2.,2.5,2.,0000)
        CALL MARKER(15)
        CALL RESET('BLSYM')
        CALL SCLPIC(0.4)
        CALL CURVE(A3,A5,34,1)
        IF(KK.EQ.2) THEN
        CALL YAXEND('NOLAST')
        ELSE IF(KK.EQ.5) THEN
        CALL YAXEND('NOFIRST')
        ELSE
        CALL YAXEND('NOENDS')
        ENDIF
        CALL RESET('YNONUM')
        CALL XTICKS(34)

```

Figure 43. Continued

```

CALL XGRAXS(-1.8,6.8,5.,2.5,' ',1,0.,1.)
CALL XGRAXS(-1.8,6.8,5.,2.5,' ',-1,0.,1.)
CALL XTICKS(5)
CALL XGRAXS(-1.,1.,5.,2.5-1./3.4,' ',1,1./3.4,1.)
CALL XGRAXS(-1.,1.,5.,2.5-1./3.4,' ',-1,1./3.4,1.)
CALL YGRAXS(-.4,.2,.4,2.,' ',-1,2.5,0.)
IF(KK.EQ.2) THEN
CALL RESET('XNONUM')
CALL XGRAXS(-1.,1.,5.,2.5-1./3.4,' ',1,1./3.4,0.)
ENDIF
CALL ENDGR(0)
GOTO 999

900 CALL PHYSOR(2.,0.5)
CALL AREA2D(2.5,2.)
CALL XREVTK
CALL YREVTK
CALL INTAXS
CALL YAXANG(0.)
CALL YNAME(' ',1)
CALL XNAME(' ',1)
CALL VECTOR(2.5,0.,2.5,2.,0000)
CALL YAXEND('NOLAST')
CALL XNONUM
CALL XTICKS(34)
CALL GRAF(-1.8,6.8,5.,0.,50.,150.)
CALL MARKER(15)
CALL RESET('XNONUM')
DO 910 J=1,34
910 A4(J)=A4(J)*120./H4
CALL SCLPIC(0.4)
CALL CURVE(A3,A4,34,1)
CALL RESET('SCLPIC')
CALL XTICKS(5)
CALL XGRAXS(-1.,1.,5.,2.5-1./3.4,' $',100,1./3.4,0.)
CALL ENDGR(0)

999 CONTINUE

CALL ENDPL(1)

CALL DONEPL
STOP
END

```

## Appendix B Magnetic Anisotropy of Thin Films

There has been some discussions about the thin film anisotropy energy<sup>20,59</sup> which may cause confusion, and some interesting work has been done which provides guidance in how to make use of the form of anisotropy in deriving the thin film properties.<sup>59,60</sup> A general form of anisotropy energy is usually expressed in terms of direction cosines of the unit vector  $\mathbf{u}$ ,  $\mathbf{M}=[\mathbf{M}]\cdot\mathbf{u}$ .

$$\mathbf{u} = \alpha_x \mathbf{i}_x + \alpha_y \mathbf{i}_y + \alpha_z \mathbf{i}_z. \quad (15)$$

where

$$\begin{aligned} \alpha_z &= \cos\theta \\ \alpha_x &= \sin\theta \cos\phi \\ \alpha_y &= \sin\theta \sin\phi \end{aligned} \quad (16)$$

where  $\phi$  and  $\theta$  are the azimuthal and polar angles relative to z-axis, and

$$\alpha_x^2 + \alpha_y^2 + \alpha_z^2 = 1 \quad (17)$$

When the Cartesian coordinations are chosen such that the axes coincide with the mirror planes, only even order terms remain in the crystal anisotropy

$$\begin{aligned} E_{\text{anisotropy}} &= K^{(2)}_z \alpha_z^2 + K^{(2)}_x \alpha_x^2 + K^{(2)}_y \alpha_y^2 + K^{(4)}_x \alpha_x^4 + K^{(4)}_y \alpha_y^4 + K^{(4)}_z \alpha_z^4 \\ &+ K^{(4)}_{xy} \alpha_x^2 \alpha_y^2 + K^{(4)}_{xz} \alpha_x^2 \alpha_z^2 + K^{(4)}_{yz} \alpha_y^2 \alpha_z^2 + O(\alpha^6) \end{aligned} \quad (18)$$

and in the single crystal thin films, z-axis are taken to be the film normal, and the equation holds provided the magnetic behavior is still symmetric perpendicular to the thin film plane, in and out, with no difference caused by the substrate interface and vacuum interface.

In the case of a crystal surface with a two-fold rotation symmetry as in the Co/W(001) case (cf. Chapter 6),  $K'_x \neq K'_y$ , and all the second order terms are considered leading terms. When a crystal surface possesses higher degree of rotation symmetry such as four-fold symmetry in the Fe/W(001) case, then Eq. 15 can be combined into

$$E_{\text{anisotropy}} = K_z^{(2)} \alpha_z^2 + K_{xy}^{(4)} \alpha_x^2 \alpha_y^2 + K_z^{(4)} \alpha_z^4 + O(\alpha^6) \quad (19)$$

when the sixth order or high terms can be ignored.

If one considers only the lowest order term in Eq. 16, for  $K_z^{(2)} > 0$ , the film plane is the easy plane, the plane where the remanent magnetization can lie in, for  $K_z^{(2)} < 0$  the surface normal is the easy axis, the axis where the remanent magnetization can lie in. In the easy plane situation, the in-plane anisotropy in the higher order terms will compete for the easy axis. In the quadratic approximation, the  $K_z^{(4)}$  may tend to generate canted angle easy axis off the film plane because  $\alpha_z^4$  contains the components of  $\alpha_z^2$  and  $\sin^2(2\theta)$  terms, while the  $K_{xy}^{(4)}$  will determine the easy axes in the film plane. The order of these terms will generally determine the angular periodicities of the easy axis.

MONTANA STATE UNIVERSITY LIBRARIES



3 1762 10113560 4

